DETECTION OF OH IN A FLAME USING In AS A RESONANCE IONIZATION DETECTOR ELEMENT

By

DENISE IMBROISI

A DISSERTATION PRESENTED TO THE GRADUATE SCHOOL
OF THE UNIVERSITY OF FLORIDA IN PARTIAL FULFILLMENT
OF THE REQUIREMENTS FOR THE DEGREE OF
DOCTOR OF PHILOSOPHY

UNIVERSITY OF FLORIDA

1994

Dedicated to my father and to my son.

ACKNOWLEDGEMENTS

I would like to thank my research advisor, Prof. James D. Winefordner for his guidance throughout my doctorate studies. I appreciated the opportunity of working with Dr. Winefordner; his constant enthusiasm and good mood, his promptness and willingness to help made this work much easier.

I would like to express my sincere gratitude to Dr. Giuseppe Petrucci for all the help in the laboratory and for helping me with my many questions during the past few years. Besides being a great co-worker, Giuseppe helped a lot with my confusing working schedule right after the birth of my son. His ideas and suggestions to this whole work were invaluable.

I acknowledge the priceless discussions, suggestions and comments of Dr. Nicolo Omenetto, specially those related to the proposed energy transfer mechanism of the OH/In-RID.

I thank Dr. Ben Smith, to whom I turned for answers to many of my questions. His contribution to my work was really appreciated.

Many group members have given me much help in the past years. Special thanks go to Dennis Hueber for his help with the computers. Rob Guenard was a big help during the last months of work. I would also to thank the members of the

group, past and present, whose friendship highlighted my professional life during the past years: Stefanie Pagano, Sue Ohorodnik, Monica Escobar, MaryAnn Gunshefski, Cheri Morgan, Yuan-Hsiang Lee, Chonyu Chen, Andrea Pless, Wilfredo Resto, Donna Robie, Bill Spencer, Wellington Masamba, Raul Badini, Nancy Mullins and Nancy Szabo, just to mention a few.

I acknowledge the Conselho Nacional de Desenvolvimento Científico e Tecnológico (CNPq) for awarding me the scholarship that supported my studies at the University of Florida.

Many important family moments were missed by myself while studying abroad; I would like to thank my parents for their love and incentive. Even separated physically, we will always be together. My gratitude and love goes to my sister Deila for taking care of Tomás during the past year. Mamãe Deila, Gugu, Leleo and Fed made my life in Gainesville a more enjoyable experience. Dênia has always given her time and support to all my efforts and Dennis helped me to keep going with his calls. I also thank Diniz for the opportunity of studying English before coming to the U.S.A.

I would like to thank Dêner for his love and support. Most of all, I would like to thank him for sharing his birthday present with me. I would also like to thank Tomás for being here, with his kisses and hugs and for the uncountable hours of pure pleasure and happiness. He brought light and perspective to my life.

TABLE OF CONTENTS

ACKNOWLEDGEMENTS iii

LIST OF TABLES vii

LIST OF FIGURES viii

ABSTRACT xii

CHAPTERS

1 INTRODUCTION 1

2 LASER ENHANCED IONIZATION 7

- Introduction 7
- Thermal Ionization Enhancement 9
- Laser Perturbation of Flame Ionization 12
  - Single Step Excitation 15
  - Two-step Excitation 18
- LEI Analytical Performance 20

3 INDIUM - RESONANCE IONIZATION DETECTOR 24

- Resonance Monochromators 24
- Resonance Ionization Detectors 27
  - RID Figures of Merit 32
  - Line-broadening Mechanisms 34
- Indium as a RID Element 37
- Experimental 38
- Results and Discussion 44
  - Calibration of the Transimpedance Amplifier 44
  - One-step Excitation 44
  - Stepwise Excitation 50
- Calculation of the Quantum Efficiency. 59

4 OH DETECTION IN THE In-RID 64

- Introduction 64
- OH Radical - General Considerations 67
- Experimental 72
- Results and Discussion 73

Optimization Studies 73
Investigation of Mechanisms 109

5 FLAME TEMPERATURE MEASUREMENTS USING THE OH/In-RID 145

Introduction 145
Theory 146
Experimental 149
Results and Discussion 153

6 CONCLUSIONS AND FUTURE WORK 186

REFERENCE LIST 191

BIOBRAPHICAL SKETCH 195

LIST OF TABLES

Table 1. In transitions that could be coupled with λ_{23} and closest OH transitions 132

Table 2. Transitions of OH (1→0) used for calculation of temperature values in the flame 154

Table 3. Temperatures obtained for the OH/In-RID technique 168

Table 4. Temperatures obtained for the OH/In-RID technique 172

Table 5. Temperatures obtained for the LIF technique 183

LIST OF FIGURES

Figure 1. Partial excitation spectrum of OH 4

Figure 2. Expanded excitation spectrum of OH 6

Figure 3. General configuration of a LEI experiment 11

Figure 4. Excitation and ionization processes for LEI 14

Figure 5. Schematic diagram of the resonance detector proposed by Sullivan and Walsh 26

Figure 6. Schematic diagram of a resonance ionization detector 29

Figure 7. Experimental configuration used in the In-RID studies 40

Figure 8. Saturation curve for one-step excitation of In - Linear plot 47

Figure 9. Saturation curve for one-step excitation of In- Log-log plot 49

Figure 10. Saturation curve for the first excitation step in the stepwise excitation of In - Linear plot 52

Figure 11. Saturation curve for the first excitation step in the stepwise excitation of In - Log-log plot 54

Figure 12. Saturation curve for the second excitation step in the stepwise excitation of In - Linear plot 56

Figure 13. Saturation curve for the second excitation step in the stepwise excitation of In - Log-log plot 58

Figure 14. Determination of α - Simultaneous recording of absorption of λ_{12} and LEI intensity 62

Figure 15. Partial excitation spectrum of OH showing peak assignments 66

Figure 16. Energy diagram for OH major bands 69

Figure 17. Saturation curve for $\lambda_{exc}=Q_15=282.6674$ nm in absence of λ_{23} - Linear plot 76

Figure 18. Saturation curve for $\lambda_{exc}=Q_15=282.6674$ nm in absence of λ_{23} - Log-log plot 78

Figure 19. Saturation curve for $\lambda_{23}=786.44$ nm in absence of λ_{exc} - Linear plot 80

Figure 20. Saturation curve for $\lambda_{23}=786.44$ nm in absence of λ_{exc} - Log-log plot 82

Figure 21. Saturation curve for $\lambda_{exc}=Q_15=282.6674$ nm in presence of $\lambda_{23}=786.44$ nm - Linear plot 85

Figure 22. Saturation curve for $\lambda_{exc}=Q_15=282.6674$ nm in presence of $\lambda_{23}=786.44$ nm - Log-log plot 87

Figure 23. Saturation curve for $\lambda_{23}=786.44$ nm in presence of $\lambda_{exc}=Q_15=282.6674$ nm - Linear plot 89

Figure 24. Saturation curve for $\lambda_{23}=786.44$ nm in presence of $\lambda_{exc}=Q_15=282.6674$ nm - Log-log plot 91

Figure 25. Effect of the high-voltage applied to the collection electrode on the LEI signal 94

Figure 26. Effect of the concentration of the nebulized indium solution on the LEI signal 97

Figure 27. Effect of the incident power applied to the ultrasonic nebulizer on the LEI signal 100

Figure 28. Effect of the gas flow rates on the LEI signal 102

Figure 29. Expanded excitation spectrum in the flame In-RID 105

Figure 30. Expanded excitation spectrum in the flame In-RID - Enlargement 107

Figure 31. Second step (λ_{23}) excitation in the OH/In-RID with $\lambda_{exc}=Q_1 5=282.6674$ nm:
a) 740.01 - 767.40 nm 111
b) 767.40 - 792.92 nm 112

Figure 32. Schematic diagram of the proposed fluorescence capture mechanism 116

Figure 33. Partial excitation spectrum of OH 119

Figure 34. Saturation curve for the fluorescence signal at 303.9 nm while nebulizing water, $\lambda_{exc}=Q_1 5=282.6674$ nm - Linear plot 122

Figure 35. Saturation curve for the fluorescence signal at 303.9 nm while nebulizing water, $\lambda_{exc}=Q_1 5=282.6674$ nm - Log-log plot 124

Figure 36. Emission spectrum of nebulized water, $\lambda_{exc}=Q_1 5=282.6674$ nm 126

Figure 37. Partial energy diagram for In 130

Figure 38. Schematic diagram of the proposed energy transfer mechanism 134

Figure 39. Schematic diagram of additional possible processes of energy transfer 137

Figure 40. Schematic diagram of fluorescence collection experiment 139

Figure 41. Schematic diagram of energy transfer experiment 143

Figure 42. Modified experimental configuration showing the two excitation laser beams crossing at 90° in the flame 152

Figure 43. Typical excitation spectrum of OH rotational transitions used for flame temperature measurements in the OH/In-RID 157

Figure 44. Boltzmann plots used for calculation of temperature; transitions used were from the 1→0 band of OH in the region 286.0-287.8 nm 159

Figure 45. Boltzmann plots obtained for the "sitting" procedure; transitions used were from the 1→0 band of OH in the region 286.0-287.8 nm 162

Figure 46. Typical excitation spectrum of OH rotational transitions used for flame temperature measurements in the OH/In-RID 164

Figure 47. Representative Boltzmann plot used for calculation of temperature 167

Figure 48. Flame temperature profile at ≈ 2 mm above the inner cone using the procedure of scanning the excitation laser in the OH/In-RID technique 170

Figure 49. Flame temperature profile at ≈ 2 mm above the inner cone using the procedure of "sitting" on the peak of each transition in the OH/In-RID technique 174

Figure 50. Excitation spectrum of OH obtained by the use of the LIF technique 177

Figure 51. Representative Boltzmann plot used for calculation of temperatures 180

Figure 52. Flame temperature profile at ≈ 2 mm above the inner cone using the procedure of scanning the excitation laser in the LIF technique 182

Abstract of Dissertation Presented to the Graduate School
of the University of Florida in Partial Fulfillment of the
Requirements for the Degree of Doctor of Philosophy

DETECTION OF OH IN A FLAME USING In AS A RESONANCE IONIZATION DETECTOR ELEMENT

By

Denise Imbroisi

April 1994

Chairperson: James D. Winefordner
Major Department: Chemistry

Rotational spectra of the 1 → 0 vibrational band of OH radical in a flame were unexpectedly recorded in a resonance ionization detector (RID) using indium as the detector element. Step-wise excitation was employed in the In-RID. A laser tuned to 303.9 nm was used as the first excitation step (transition 5p $^2P_{1/2}$ → 5d $^2D_{3/2}$). The second excitation step was provided by a laser tuned to 786.4 nm (transition 6p $^2P_{3/2}$ → 10d $^2D_{5/2}$). The ionization step was achieved through collisions in the flame.

OH rotational transitions in the 1 → 0 band were excited when the first excitation laser was tuned to the range 281 - 288 nm. The second excitation step in the RID was kept at 786.4 nm.

Two mechanisms were proposed to explain the detection of OH. The fluorescence capture mechanism involved excitation of

OH from v"=0 to v′=1 followed by upward collisional redistribution to the v′=2, K′=25 level, which then decayed radiatively by emission at 303.937 ($Q_1$25 transition of 2 → 1 band). The absorption of these photons by indium atoms in the flame served as the first excitation step in the In-RID.

The energy transfer mechanism involved excitation of OH from v"=0 to v′=1, followed by collisional redistribution downwards to v′=0. The first level of the In-RID second excitation step, In $^2P^o_{3/2}$, was populated through energy transfer from OH v′=0 to In $^2P^o_{1/2}$ level.

Both mechanisms were investigated during this study. No unequivocal proof to the actual mechanism involved in the detection of OH using the OH/In-RID was found.

Optimization studies of the OH/In-RID were performed. Among the conditions optimized were the concentration of indium solution, the high voltage applied to the collection electrode and the gas flow rates in the flame.

The OH/In-RID was proposed as a technique for combustion diagnostics due to its spectral (≈ 30 pm) and spatial resolution (volume probed ≈ 2×10^{-6} cm^3). Flame temperature measurements were determined using the OH/In-RID; the results were compared with the values obtained by laser induced fluorescence (LIF) technique.

CHAPTER 1
INTRODUCTION

This research work was brought about by the serendipitous recording of a partial excitation vibrational spectrum of the transitions in the (1,0) vibrational band of OH molecules.

While trying to observe an *in situ* N_2 Raman spectrum in an atmospheric pressure acetylene-air flame by the utilization of a resonance ionization detector (RID) with indium as the detector element, the spectrum shown in Figure 1 was recorded. The excitation laser was scanned from 283.3 to 284.3 nm according to the following explanation. The photons to be detected in the In-RID used in our experiments are called signal photons and have a wavelength of 303.9 nm (λ_{sig}) . As the Raman shift of N_2 is 2330.7 cm^{-1} ($\tilde{\nu}_{Raman}$), the required excitation wavelength (λ_{exc}) is 283.8 nm, according to equation (1) [1,2]:

$$\frac{1}{\lambda_{exc}} = \frac{1}{\lambda_{sig}} + \tilde{\nu}_{Raman} \tag{1}$$

The partial excitation spectrum from Figure 1 was then expanded by scanning the excitation laser from 280 to 288 nm, as can be observed in Figure 2. More unexpected peaks were observed and those peaks were later assigned to transitions of the OH radical.

The purpose of this dissertation is to describe the work done to characterize the phenomenon pictured above. Possible mechanisms that could lead to the experimental data observed, namely the fluorescence mechanism and the energy transfer mechanism, were investigated. The analytical optimization of the experimental conditions was performed and the application of this method to evaluate flame temperatures was examined.

Figure 1. Partial excitation spectrum of OH.

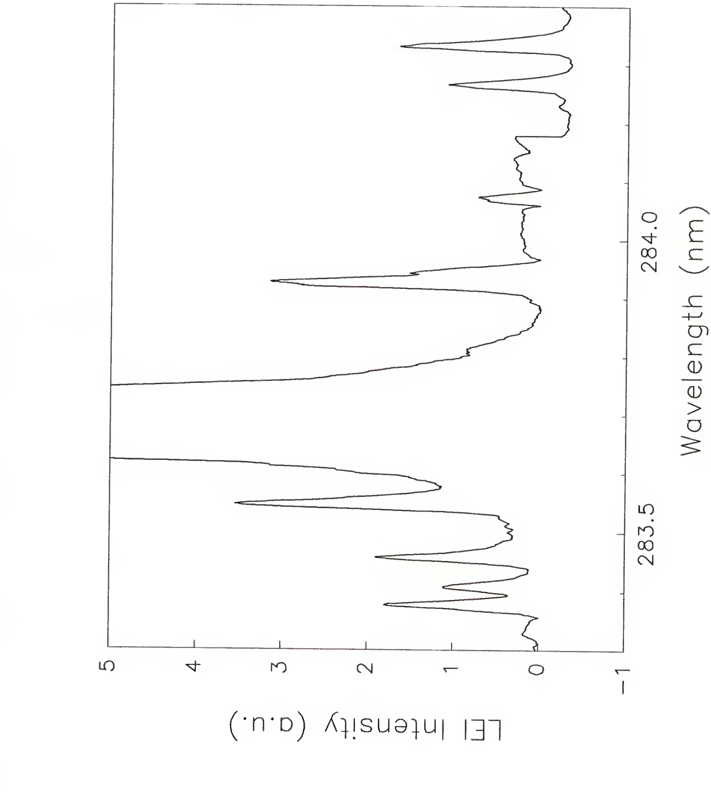

LEI Intensity (a.u.)
5
4
3
2
1
0
−1
283.5
284.0
Wavelength (nm)

Figure 2. Expanded excitation spectrum of OH.

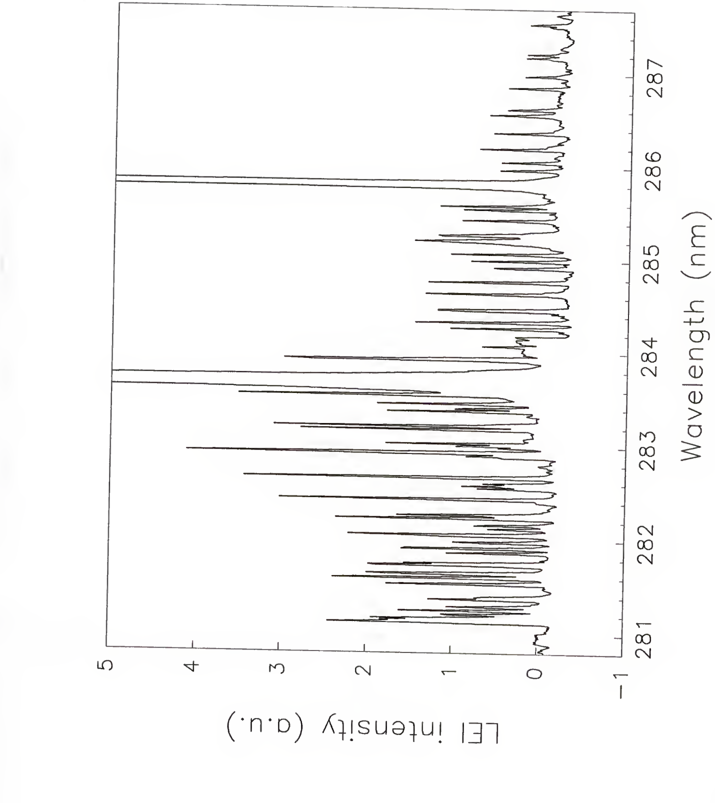
LEI intensity (a.u.)
5
4
3
2
1
0
−1
281
282
283
284
285
286
287
Wavelength (nm)

CHAPTER 2
LASER ENHANCED IONIZATION

Introduction

Resonance ionization spectroscopic techniques are based on the excitation of atomic or molecular species by one or more laser beams, followed by the ionization of the excited species and detection of the electron of the ion-pair produced. The ionization step may be achieved by different means, such as photoionization, when another laser beam produces the ions, or by collisional means, among others. Laser enhanced ionization (LEI) is the term utilized when the ionization step is produced by means of collisions, as it is the most general situation in collisional rich environments such as atmospheric pressure flames [2-4].

Different types of flames and burners have been utilized as atomic sources for LEI. Nitrous oxide-acetylene and air-acetylene flames are most commonly used for analytical applications. The former shows a higher inherent flame ionization rate and gives higher limits of detection (LOD),and the air-acetylene flame is generally used if it can provide effective atomization for the species being studied.

Pulsed or continuous wave (cw) lasers may be employed as excitation sources. If the latter are used they typically are amplitude modulated in order to discriminate against the continuous thermal ionization background of the flame.

LEI is detected by the monitoring of the resulting current produced by the application of a voltage across the flame through a circuit containing a pair of biased electrodes and therefore is an optogalvanic method. The current density generated in a flame by the applied electric field is a measure of ionization rate in a certain volume (ions generated per cm^3 per s). So, changes in the current produced by the LEI can be sensed in this type of configuration. The negative biased electrode, the cathode, collects the ions while the electrons move to the grounded burner anode. The collection efficiency can reach 100%; this is one of the advantages of the method when compared to other spectroscopic techniques, such as fluorescence, which is limited by its fractional solid angle of photons collection.

Several different types and configurations of electrodes have been used in LEI. Examples are the tungsten or molybdenum rod cathodes, flat plates of similar materials and the water-cooled stainless steel cathode. The latter can be immersed in the flame for longer periods of time without deterioration and shows a greatly improved tolerance to easily ionized matrices.

The dc background current from ions naturally present in a flame is the ultimate source of limiting noise for LEI. In a typical LEI experiment, the ac component of the flame current is discriminated against the dc component by means of a resistor-capacitor network. Figure 3 shows a block diagram of a LEI setup. The LEI signal is amplified in a high gain preamplifier (~ 10^6 V/A) and processed in a boxcar integrator. Electrical pickup of radio-frequency interferences caused by pulsed lasers can be minimized by placing the preamplifier as close as possible to the burner.

Thermal Ionization Enhancement

The LEI optical enhancement of the naturally occuring thermal ionization in flames, in which there are always collisions to a certain extent (rate of collisions > 10^9 s^{-1}) can be easily explained [2,5]. The rate constant for collisional ionization from a laser excited level j by collision partner x , k_j (s^{-1}) can be expressed as equation 2:

$$k_j = n_x \left(\frac{8kT}{\mu\pi} \right)^{1/2} \sigma_{xj} \left[e^{-(E_{ic}-E_j)/kT} \right] \tag{2}$$

where n_x is the number density of collision partners (cm^{-3}), $(8kT/\mu\pi)^{1/2}$ is the average relative velocity of collision partners (cm s^{-1}), k is the Boltzmann's constant ($8.62\mathrm{x}10^{-5}$ eV k^{-1}), T is the temperature (K), μ is the reduced mass of the collision pair, σ_{xj} is the collision cross section for ionization of the analyte in level j (cm^2) and $(E_{ic}-E_j)$ is the energy difference between the ionization continuum and the excited level j.

Figure 3. General configuration of a LEI experiment.

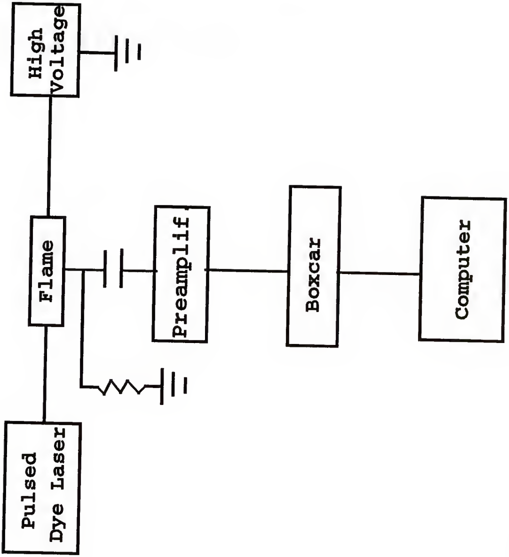
High Voltage
Flame
Preamplif.
Boxcar
Computer
Pulsed Dye Laser

The total rate of ionization, dn_{ion}/dt is proportional to k_j, as can be seen from equation 3:

$$dn_{ion}/dt \propto k_j\ n_j \qquad (3)$$

where n_j is the number density (cm^{-3}) of the laser excited level.

The ionization rate is near 1 when $E_j \approx E_{ic}$. The product kT is approximately 0.22 eV for flames with T=2500 K and therefore each eV of optical excitation provided by the laser increases the ionization rate by two orders of magnitude, or $e^{(1/0.22)}$. This increase in the rate of ionization by the promotion of atoms to higher energy levels is the basis for LEI.

Laser Perturbation of Flame Ionization

Atomic populations in a flame are optically perturbed by the utilization of laser excitation. Many of the features of LEI can be revealed by the use of kinetic rate equations to model the atomic populations in their different energy levels. In this rate equations approach, the time-dependent population of each level is found by solving a system of differential equations [5-8].

Different excitation schemes can be used in LEI as shown in Figure 4. The excitation schemes shown involve the use of one or two laser beams. In the single step excitation scheme, a laser is tuned to a resonance transition of the atom ($\lambda_{1\to2}$)

Figure 4. Excitation and ionization processes for LEI.

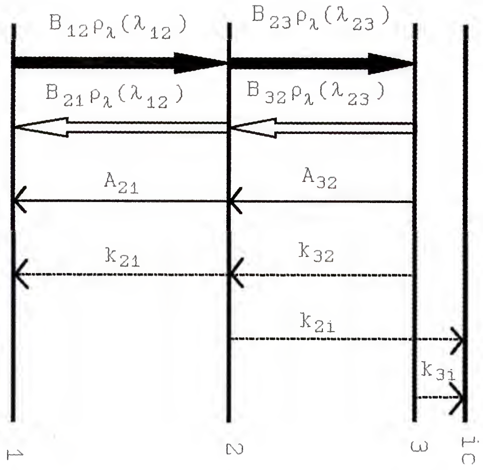
$B_{12}\rho_\lambda(\lambda_{12})$
$B_{23}\rho_\lambda(\lambda_{23})$
$B_{21}\rho_\lambda(\lambda_{12})$
$B_{32}\rho_\lambda(\lambda_{23})$
A_{21}
A_{32}
k_{21}
k_{32}
k_{2i}
k_{3i}
1
2
3
ic

and the transfer of the atoms from the excited state to the ionization continuum is promoted by collisions. In the two step or stepwise excitation scheme, the atom is promoted to the first excited state (level 1) by a laser tuned at $\lambda_{1\rightarrow2}$. A second laser tuned at $\lambda_{2\rightarrow3}$ promotes the atom to a higher excited state and the ionization is achieved by collisions. In this scheme, temporal and spatial coincidence of the two lasers in the flame is imperative, since both excitation steps share a common level.

After excitation by absorption of a resonant photon, deactivation from the excited level is possible by radiative means (spontaneous and stimulated emission) and also by collisional means (ionization or deactivation back to the originating level of the transition).

Single Step Excitation

The rate equations to be considered are the following:

$$\frac{dn_i}{dt} = k_{2i}\, n_2 \qquad (4)$$

$$\frac{dn_2}{dt} = B_{12}\rho_\lambda(\lambda_{12})\,n_1 + k_{12}n_1 - B_{21}\rho_\lambda(\lambda_{12})\,n_2 - A_{21}n_2 - k_{21}n_2 - k_{2i}n_2 \qquad (5)$$

$$n_T = n_1 + n_2 + n_i \qquad (6)$$

where A_{21} is the Einstein coefficient of spontaneous emission (s^{-1}), B_{12} is the Einstein coefficient of stimulated absorption (cm^3 J^{-1} Hz s^{-1}), B_{21} is the Einstein coefficient of stimulated emission (cm^3 J^{-1} Hz s^{-1}), k_{12} is the rate of collisional deactivation (s^{-1}), k_{2i} is the rate of collisional ionization (s^{-1}) and $\rho_\lambda(\lambda_{12})$ is the spectral energy density of the laser (J Hz^{-1} cm^{-3}) at wavelength λ_{12}, n_1, n_2 and n_i are number densities (cm^{-3}) and n_T is total atomic number density (cm^{-3}).

This system of equations can be solved by standard methods. In order to obtain the final expression for n_i additional considerations, such as evaluation of the optical saturation of the transition, must be taken into account.

Linear interaction

If the transition is not saturated, A_{21} and k_{21} are much bigger than $B_{12}\rho_\lambda(\lambda_{12})$ and the solution can be simplified as follows:

$$n_i = n_T\left[1 - \exp\left(-\frac{B_{12}\rho_\lambda(\lambda_{12})\,k_{2i}}{A_{21} + k_{21} + k_{2i}}\,\Delta t_1\right)\right] \tag{7}$$

where Δt_1 is the laser pulse duration.

The ratio n_i/n_T, called the ionization yield, will depend upon the rate of collisional ionization and the laser pulse duration, usually of the order of 10 ns. The rate constant k_{2i} can be increased by choosing an excited state closer to the ionization continuum, but even if $k_{2i}>>(A_{21}+k_{21})$ this scheme is not expected to produce any significant ionization yield, due to the extremely small value of $B_{12}\rho_\lambda(\lambda_{12})\Delta t_1$.

Optical saturation

When the spectral irradiance of the excitation laser beam is sufficiently high, the populations of the two levels involved in the atomic transition are maintained in the ratio of their respective degeneracies during the duration of the laser pulse:

$$n_1(t) + n_2(t) = n_{12}(t) \tag{8}$$

$$n_2(t) = \frac{g_2}{g_1} n_1(t) = \left(\frac{g_2}{g_1+g_2}\right) n_{12}(t) \quad . \tag{9}$$

In an optically saturated transition, $B_{12}\rho_\lambda(\lambda_{12})$ is much greater than $(A_{21}+k_{21}+k_{2i})$, i.e., the rate of induced absorption is much greater than the sum of the deactivation rates. Since $B_{12}g_1 = B_{21}g_2$, the solution of the differential equation yields:

$$n_i = n_T\left[1 - \exp\left(-\frac{g_2}{g_1+g_2} k_{2i}\Delta t_1\right)\right] \quad . \tag{10}$$

It can be seen from Equation 10 that the ionization yield is again dependent upon the product $k_{2i}\Delta t_1$. Therefore, significant ionization yields are not expected with nanosecond laser pulses for single step saturated excitation, unless k_{2i} is sufficiently large due to the closeness of the excited level to the ionization continuum.

Two-step Excitation

The stepwise excitation process considered here is such that the energy difference between the second excited level and the ionization continuum is extremely low, so that collisional ionization proceeds instantaneously and no radiative or collisional losses are observed from that level. This assumption is valid for flames and other environments with a high collisional rate. The duration of both laser pulses is the same, Δt_0.

According to the combination of the saturation-non saturation conditions of the two excitation transitions, four cases are possible:

1 - Linear interaction for both steps, so n_i is dependent on both $\rho_\lambda(\lambda_{12})$ and $\rho_\lambda(\lambda_{23})$;

2 - Linear interaction for step 1, optical saturation for step 2, so n_i is dependent on $\rho_\lambda(\lambda_{12})$;

3 - Optical saturation for step 1, linear interaction for step 2, so n_i is dependent on $\rho_\lambda(\lambda_{23})$;

4 - Optical saturation for both steps.

Expressions for calculation of n_i can be derived for all four cases [6]. Two expressions will be shown here, both regarding low levels of photons in the first excitation transition, λ_{12}, and thus applicable to resonance ionization detectors.

Linear interaction for both steps

The fraction of atoms ionized in this condition is given by equation 11:

$$n_i = n_T\left[1 - \exp\left(-\frac{B_{12}\rho_\lambda(\lambda_{12})\,B_{23}\rho_\lambda(\lambda_{23})}{A_{21}+k_{21}}\right)\Delta t_0\right] \quad . \qquad (11)$$

Linear interaction for step 1, optical saturation for step 2

For this case, n_i is given by following equation:

$$n_i = n_T\,[1 - \exp(-\,B_{12}\rho_\lambda(\lambda_{12})\,\Delta t_0)] \quad . \qquad (12)$$

When typical values for the parameters involved in equations 11 and 12 are assumed (B_{12}=B_{23}=10^{24} cm^3 J^{-1} s^{-1} Hz, A_{21}=k_{21}=10^9 s^{-1}, Δt_0=10^{-8} s, $\rho_\lambda(\lambda_{12})$= 10^{-18} J cm^{-3} Hz^{-1} and $\rho_\lambda(\lambda_{23})$= 10^{-16} J cm^{-3} Hz^{-1}), the ionization ratio yields approximately 0.05% for the case of linear interactions of both lasers and almost 1% for when transiton λ_{23} is saturated. Values of ionization yield close to 100% can be achieved by an increase in the $\rho_\lambda(\lambda_{12})$ employed for the case of saturation of the second step. As a result of these considerations, it can be seen that two step excitation with saturation of the second excitation transition must be used if it is desired to obtain significant ionization yields [9].

LEI Analytical Performance

LEI as an analytical method has several advantages over other conventional spectroscopic methods, most of them based on the selective excitation processes and on the ionization detection mechanism.

Axner and Rubinsztein-Dunlop [7] calculated the lowest detectable concentrations to be in the range 0.1 - 1 pg/ml, based on three times the standard deviation in the d.c. current. Typical flame conditions were assumed and the fundamental limitation of the number of created electrons that are needed for detection was given by the statistical shot-noise fluctuations in the natural background current through the flame.

Several elements have been determinated by LEI, among them Ag, Al, Au, Bi, Ca, Cd, Co, Cr, Cs, Fe, In, K, Li, Mg, Na, Pb, Sn, W and Yb. LEI in trace element analysis shows detection limits in the range of 1 - 100 pg/ml for aqueous solutions with one step excitation of elements with low or moderate ionization potentials. Even for elements with higher ionization potential, detection limits in the pg/ml range can be frequently achieved when a second step excitation is added, which is in excellent agreement with the theoretical value mentioned above. This shows again the drastic increase in the sensitivity of the method by the use of stepwise instead of single step excitation [10-13].

For many elements, LEI detection limits in aqueous solution are comparable to or better than the ones achieved in graphite furnace - atomic absorption spectrometry and inductively coupled plasma - mass spectrometry. The best detection limits are usually achieved by elements with low to moderate ionization potential.

The high sensitivity of the technique is based upon several of its features. The detection of electrons means that almost a 100% collection efficiency can be achieved, whereas fluorescence techniques, for example, cannot collect 4π steradians of the emitted photons. In addition, LEI does not suffer from background due to scattered laser excitation light, flame background light or ambient light and self-absorption losses.

Linear dynamic ranges reported are typically four to five orders of magnitude. The upper limit results from nonlinear collection efficiency due to the large number of charges created.

The high selectivity of LEI is due to the utilization of narrow laser pulses for the excitation process. Pulsed dye laser bandwidths of the order of 0.3 cm^{-1} give spectral resolving powers equivalent to the best spectrometers used in atomic emission ($\sim 10^5$) and at least as good as the ones achieved in atomic absorption spectrometry (AAS). However, laser sources used in LEI have the advantage of being tunable.

LEI selectivity can be further improved by the use of a second step excitation in stepwise excitation processes due to the small probability of having the two excitation wavelengths from the analyte coincident with two transitions of another element.

LEI suffers from some interferences that limit its performance as a trace element technique. There are some interferences that are not related to the laser source, such as the background thermal ionization of the flame species or from the sample matrix and the production of charge sheaths at the electrode by continuous ionization in the flame. The latter can impair the charge collection efficiency and affect the accuracy and can be reduced by the use of an immersed stainless steel water-cooled electrode.

The laser excitation source may also induce some interferences. Atomic species other than the analyte can spectrally interfere in the excitation step; however, this can be considerably reduced by stepwise excitation and the use of laser powers which can affect the analyte and the interferent differently. For example, LEI signals can be acquired when the saturation condition is achieved by the analyte and not by the interferent species, thus improving the selectivity.

Ionization signals can originate from photoionization of matrix elements in the system. Photoionization can be observed from the highly populated ground state, when the ionization potential is smaller than the photon energy, from thermally populated excited states or from excited states that are populated due to laser excitation.

NO molecules in N_2O-based flames can cause spectral problems due to resonant enhanced multiphoton ionization. For NO, two photons of wavelength smaller than 290 nm are sufficient to photoionize the molecule. On the other hand, CH and OH molecules do not contribute to the background LEI signal, because even if they have molecular absorption bands in the scanned region, the excited molecule has a larger tendency to dissociate than to ionize.

LEI has been used in applications other than trace analysis [7,14]. Examples of these applications are flame rise velocity measurements, determination of mobilities and diffusion processes in flames, measurements of metastable lifetimes of atoms in flames, determinations of ion-electron recombination rates and study of the effect of easily ionizable elements on ion-electron recombination in inductively coupled plasmas.

CHAPTER 3
INDIUM - RESONANCE IONIZATION DETECTOR

Resonance Monochromators

The usual method of isolation of a resonance line is by the use of a grating monochromator. Wood in his innovative work at the beginning of the century [15,16] demonstrated an alternative way of isolating resonance lines. He used what is called today a resonance monochromator. In this approach, the resonance lines emitted from an atomic species can be isolated when they are passed through and absorbed by atomic vapor of the same element and subsequently reemitted and collected, usually at an angle of 90° by a photomultiplier.

Sullivan and Walsh proposed in 1968 the use of resonance monochromators (RM) in modern spectroscopy, as shown in Figure 5 [17]. In that work and in some previous ones [18,19], they discussed different types of devices for the production of the resonance radiation, such as hollow cathode lamps and cathodic sputtering in an electrical discharge, as well as resonance detectors of the thermal and sputtering types. Potential advantages of the RM were stressed, namely resolution of the order of atomic linewidths (0.01 Å) determined mainly by the physical conditions prevailing in the detector and blindness to nonresonance light emitted by the atomic vapor reservoir.

Figure 5. Schematic diagram of the resonance detector proposed by Sullivan and Walsh.

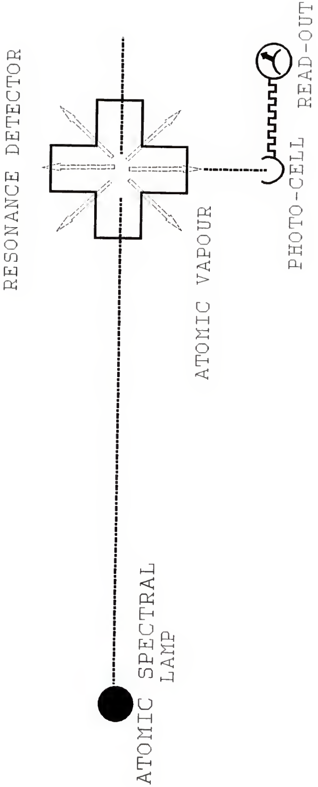
ATOMIC SPECTRAL LAMP
ATOMIC VAPOUR
RESONANCE DETECTOR
PHOTO-CELL
READ-OUT

Examples of atomic cells used as resonance detectors include hollow cathode lamps [20,21], flames [22] and furnaces [23]. Spectroscopic techniques such as fluorescence [24], optogalvanic effect [21,25,26] and atomic absorption [23] were employed with the RM.

RMs have been mainly used in atomic absorption analysis and mathematical expressions for calculation of radiance and absorbance for atomic absorption with resonance monochromators were derived by Palermo and Crouch [27].

Resonance Ionization Detectors

Matveev *et al.* first proposed a resonance photon detector based on stepwise atomic photoionization [28,29]. This detector is known as a resonance ionization detector and it is pictured in Figure 6. In a resonance ionization detector configuration, the detector compartment is filled with vapor of the detector atomic element, mainly in its ground state. The detector is always irradiated with photons of energy $h\nu_{23}$ corresponding to a second excitation step for that element. The photons to be detected must have energy $h\nu_{12}$ corresponding to the first excitation step for the detector element. They are emitted by another radiation source (the sample compartment) as a result of some excitation process and are collected into the resonance detector. After the excitation processes, the ionization of the detector element is usually achieved by collisions if the detector reservoir is a flame.

Figure 6. Schematic diagram of a resonance ionization detector. The excitation/ionization processes ocurring in the resonance detector compartment are shown on the right side of the drawing.

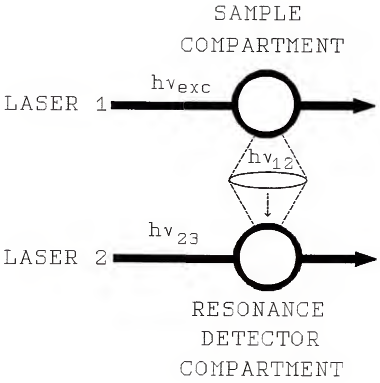
SAMPLE COMPARTMENT
hν exc
LASER 1
hν 12
hν 23
LASER 2
RESONANCE DETECTOR COMPARTMENT

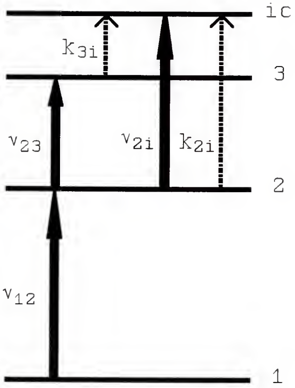
ic
3
2
1
k 3i
ν 23
ν 2i
k 2i
ν 12

Photoionization may occur if energy $h\nu_{23}$ is adequate or if a third laser with energy $h\nu_{3i}$ is employed. The analytical signal is the electrical current measured in the ionization detector [30]. The number of ion-pairs created in the detector is proportional to the number of photons ν_{12} absorbed in the first excitation step; therefore, the photon detection is based on ionization.

Some of the advantages of a RID are the sensitivity, the high quantum efficiency, the large solid angle of collection of the incoming radiation (up to 2π sr) and the high spectral resolution. Another advantage is the fact that the excitation and detection processes are physically separated in two independent atomizers.

The detector reservoir is one of the most important elements of the RID. Two main types of cells have been used, open cells in the form of flames and closed, evacuated cells in the form of hollow-cathode lamps, high-frequency spectral lamps and chambers with heated walls [31]. Several advantages of using flames as atomic reservoirs for RID can be pointed out. The energy requirements for the ionization step can be minimized, due to the flame thermal energy, the solutions used to produce atomic vapors are easily replaced, and the level of intrinsic noise is low.

The signal photons emitted from the sample compartment are not the only radiation collected into the RID that can cause a pulsed signal. Scattering in the sample compartment from unvaporized matrix particles and thermal emission from the matrix and analyte can also contribute to the total signal in the RID. If the scattered light is non-resonant an appropriate cut-off filter can be used to prevent it from reaching the RID. Another possibility is to delay the excitation laser in the RID until the scattering is minimized, which can be difficult to realize in atomizers with a high collision frequency. Other possibility is to decrease the laser intensity for the sample compartment if the excitation processes are saturated, and therefore linearly reduce the scattered radiation with minimal losses of the signal photons [30].

RIDs have been used successfully for recording absorption lines in atomic absorption and in intracavity laser spectroscopy [32]. Different general optical schemes have been proposed and evaluated for the RID by different research groups [33,34].

The utilization of the RID for detection of Raman scattering was proposed and theoretically evaluated by Smith *et. al* [35]. The first experimental demonstration of the detection of Raman photons by means of LEI of magnesium atoms in an air-acetylene flame using carbon tetrachloride as the Raman scattering species was later demonstrated [36].

A comprehensive investigation of magnesium as a resonance ionization detector element was performed by Petrucci *et. al*

[37]. The Mg-based flame RID was shown to be capable of detecting about 1000 photons with a resolution of better of 0.5 cm^{-1}.

RID Figures of Merit [38]

The primary and most significant figure of merit of a photon detector is its quantum efficiency (QE), i.e., the ratio between the number of ion-pairs created in the detector and the number of incident photons.

In the absence of a metastable state, η_i^* represents the fractional probability of ionization and it is given by equation 13 (refer to Figure 4):

$$\eta_i{*} = \frac{k_{2i}+k_{3i}+\sigma_{3i}\ I_{23}}{k_{2i}+k_{3i}+\sigma_{3i}I_{23}+A_{21}+k_{21}} \qquad (13)$$

where σ_{3i} is the peak cross-section of the transition level 3→ic, evaluated at the central frequency of the transition (cm^2), I_{23} is the laser photon irradiance integrated over the emission spectral bandwidth ($s^{-1}\ cm^{-2}$), k_{2i} and k_{3i} are rates of collisional ionization (s^{-1}), A_{21} is the Einstein coefficient of spontaneous emission (s^{-1}) and k_{21} is the rate of collisional deactivation (s^{-1}).

The quantum efficiency is then defined by equation 14:

$$QE = \eta_i{*}\ [1 - e^{-\sigma_{12}\, n_1\, l_{abs}}] \qquad (14)$$

where l_{abs} is the absorption length (cm) and n_1 is the atomic number density in the ground state (cm^{-3}). The quantity inside the brackets represents the fraction of photons absorbed by the ground state n_1 over the entire absorption length and should be unity, which is easy to achieve for transitions of moderate strengths ($\sigma_{12} \sim 10^{-12} - 10^{-14}$ cm^2).

Another figure of merit of a RID is the ion yield (Y_i), defined as the ratio between the number of ion-pairs created during the interaction and the number of atoms present in the probe volume.

Ion yield mathematical expressions have been derived by Omenetto *et al.* for three cases: linear interaction for both excitation steps, linear interaction for the first step in the absence of the second excitation step and optical saturation for the first step and linear interaction for the second step. Those expressions can be found in reference 38.

An ionization method can be used either as an analytical method or as a photon detector. When the approach is the analytical method, the requirement is to achieve unity ion yield, irrespective of the number of primary photons necessary to form an ion-pair. On the other hand, if the method is to be used as a photon detector, the requirement is to have unity quantum efficiency, and one ion-pair should be created by each primary photon absorbed.

Line-broadening Mechanisms

Atomic lines have a finite frequency (or wavelength) distribution. The width of a line is generally described by its width at one-half of the maximum height, or full-width at half maximum (FWHM). When a laser with a narrow exciting linewidth ($\Delta\nu_{exc}$) is used in a RID, the resolution of the detector is determined mainly by the physical conditions existing in the detector compartment. The response profile of the RID is then the result of a variety of line-broadening phenomena.

Natural broadening

Due to emission and absorption from radiation and collisional processes, the energy states j (upper) and i (lower) participating in an atomic excitation process have finite lifetimes. This radiative or natural lifetime causes natural broadening ($\Delta\nu_N$, Hz) and is given by equation 15:

$$\Delta\nu_N = \frac{A_{ji}}{2\pi} \tag{15}$$

where A_{ji} is the Einstein coefficient for spontaneous emission (s^{-1}). Natural broadening is usually negligible when compared to other broadening sources.

Spontaneous emission of photons leads to an exponential time decay of the excited-state population. As a consequence, the radiation emitted has a frequency distribution. The frequency distribution resulting from natural broadening is described by a Lorentzian or dispersion function. The normalized spectral profile due to the natural broadening $S_{\nu N}$ (Hz) is symmetric with respect to the line center and is given by:

$$S_{\nu N} = \frac{2/(\pi\,\Delta\nu_N)}{1 + [2(\nu_m - \nu)/\Delta\nu_N]^2} \tag{16}$$

where ν_m is the frequency at the line center (Hz).

Collisional broadening

Broadening caused by collisions increases with the concentration of collision partners and is also called pressure broadening. Collisions can leave the atom in the same energy level or a different one, and are called respectively adiabatic or diabatic collisions.

Diabatic collisions reduce the lifetime of the initial state and originate an exponential decay of the excited-state population with time. The half-width of a diabatic collision ($\Delta\nu_d$, Hz) is given by equation 17:

$$\Delta\nu_d = \frac{k_j}{2\pi} \tag{17}$$

where k_j is the collisional deactivation rate (s^{-1}).

The adiabatic collision half-width ($\Delta\nu_a$, Hz) is given by:

$$\Delta\nu_a = \left(\frac{8kT}{\pi^3\mu}\right)^{1/2} \sigma_a\, n_x \tag{18}$$

where k is the Boltzmann constant (J K^{-1}), T is the temperature (K), μ is the reduced mass of the collision pair, σ_a is the optical cross section for adiabatic collision broadening (cm^2) and n_x is the number density of collision partners (cm^{-3}).

The spectral line profile of lines broadened by adiabatic or diabatic collisions can be represented by a Lorentzian function of the form of equation 16 with $\Delta\nu_a$ or $\Delta\nu_d$ replacing $\Delta\nu_N$.

If natural and collisional broadening are assumed to be mutually independent, the total FWHM of the Lorentzian profile ($\Delta\nu_L$, Hz) is given by equation 19:

$$\Delta\nu_L = \Delta\nu_N + \Delta\nu_C \qquad (19)$$

where $\Delta\nu_c$ (Hz) is the FWHM from adiabatic and diabatic collisions. In flames, $\Delta\nu_C >> \Delta\nu_N$ and $\Delta\nu_L \sim \Delta\nu_C$, and so the adiabatic collision broadening, which is usually much larger than the diabatic one, will be the main source of broadening.

The total spectral profile ($S_{\nu L}$, Hz) is also Lorenztian and has the form of equation 17, with $\Delta\nu_L$ replacing $\Delta\nu_N$.

Doppler broadening

Doppler broadening is caused by the statistical distribution of velocities of the emitting or absorbing atoms along the observation path. The Doppler FWHM ($\Delta\nu_D$, Hz) is given by equation 20:

$$\Delta\nu_D = 2\left[\frac{2(\ln 2)kT}{m}\right]^{1/2}\frac{\nu_m}{c} \tag{20}$$

where m is the atomic weight (g) and c is the speed of light.

If the velociy of the atom does not change while radiating, the distribution of velocities predicted by Maxwell's law is a Gaussian function. Therefore, the profile of a Doppler-broadened line, $S_{\nu D}$ (Hz), has also a Gaussian shape:

$$S_{\nu D} = \frac{2\sqrt{\ln 2}}{\Delta\nu_D\sqrt{\pi}}e^{-4(\ln 2)(\nu-\nu_m)^2/\Delta\nu_D^2} \tag{21}$$

Doppler broadenings are predominant in low pressure environments.

Indium as a RID Element

The characterization of indium as a RID element in a flame was done by Badini et. al [39]. The authors used a stepwise excitation scheme, with a laser tuned to 303.9 nm as the first excitation step (transition 5p $^2P_{1/2}$ → 5d $^2D_{3/2}$) and with the second excitation step provided by a laser tuned to 786.4 nm (transition 6p $^2P_{3/2}$ → 10d $^2D_{5/2}$). The initial level of the second excitation step is not connected optically to the final level of the first excitation level, being populated only through collisions.

The choice of the first excitation transition was based on the fact that its final level (5d $^2D_{3/2}$) is not appreciably populated in a flame and therefore does not contribute significantly to the background noise when the second excitation step is added.

The final level of the second excitation (10d $^2D_{5/2}$) transition lies only 0.228 eV below the ionization continuum. The collisional ionization probability in this case is close to unity, since this energy difference is smaller than 3kT in a collisional rich environment, i.e., an atmospheric pressure flame.

The QE reported for their system [39] was 0.76, the minimum detectable energy (based on S/N=3) was 1 x 10^{-15} J and the minimum detectable number of photons was 1600.

Experimental

The experiments conducted to characterize the performance of the In-RID in our system used the experimental configuration shown in Figure 7. A frequency doubled Nd-YAG laser (532 nm) (Model YG581-30; Continuum, Santa Clara, CA) was used to pump two dye lasers (Models TDL-50; Continuum, Santa Clara, CA). The Nd-YAG output was typically 300 mJ per pulse, with a pulse duration of 12 ns. The pump energy was split in a ratio 40%/60% to pump the dye lasers. One of the dye lasers, pumped with 180 mJ, was used for the transitions in the near-IR region. The other dye laser, pumped with 120

Figure 7. Experimental configuration used in the In-RID studies.

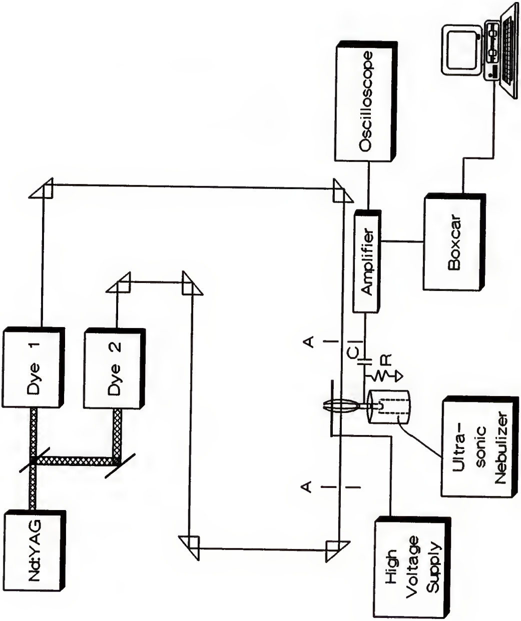
Nd:YAG
Dye 1
Dye 2
A
A
C
R
Amplifier
Oscilloscope
Boxcar
High Voltage Supply
Ultra-sonic Nebulizer

mJ, was used for the transitions in the UV region, after the dye fundamental output was doubled with a KDP frequency doubling crystal. In the latter case, the fundamental and the doubled output could be either separated by the use of a low bandpass colored filter, which absorbed the visible wavelengths, or by the use of a Pellin-Broca prism. The dyes used for the generation of the wavelengths necessary to the work were from the rhodamine family (Rhodamine 590, Rhodamine 640, Rhodamine 610, or mixtures of these dyes) for the UV generation or from the LDS family (LDS 765 or a mixture LDS 765/LDS 821) for the generation of the near-IR wavelengths. The two dye laser beams were counterpropagating in the flame. They were also made spatially and temporally coincident in the flame. Temporal coincidence of the two beams was checked with a fast photodiode, risetime < 200 ps (ET 2000; Electro-Optics Technology, Fremont, CA) whose output was connected to a fast digitizing oscilloscope (Model 2430A; Tektronix, Inc., Beaverton, OR). The fast photodiode was placed at the position occupied by the flame in the set-up and the laser beams were alternately sent to the photodiode. The temporal coincidence was then achieved by increasing or decreasing the path length of one of the beams until both beams were temporally coincident.

For the In-RID, the wavelength used to emulate the signal photons to be detected and thus representing the first excitation step was 303.9 nm. The laser beam was expanded 8-

fold, reduced to 2 mm in diameter with an iris diaphragm and attenuated with neutral density filters before going to the flame. The best signal observed was when the second excitation step utilized was at 786.4 nm; in this case, the laser beam was reduced to 3 mm in diameter before going into the flame.

The mini-burner used to support the air-acetylene flame was a 2 cm long, 1.9 mm i.d. stainless-steel tube that was pressure fitted into a phenolic base. The phenolic base was fitted into a conventional atomic absorption pre-mix spray chamber. An aluminum tube was used as a radio-frequency pick-up shield for the burner. A complete description of this burner can be found in reference 37.

A premixed acetylene-air flame was utilized. The flow rates were 108 cm^3/min for the acetylene and 800 cm^3/min for the air.

A laboratory-constructed ultrasonic nebulizer was used to carry the 2% indium solution used in the experiments into the flame. The nebulization rate used assured an indium concentration in the flame sufficient to absorb ≈ 100% of the signal photons. This was checked by measuring the absorbance of an In-hollow cathode lamp 303.9 nm line going into the flame with a monochromator and a photomultiplier tube.

Detection of the current produced in the RID was made by applying a high voltage (usually -1200 V) between the burner tube, the anode, and an immersed water-cooled tubular stainless steel electrode (3 mm o.d.), the cathode.

The laser-induced current was a.c. coupled into a current-to-voltage transimpedance amplifier (Model A1, Thorn EMI; Gencom, Plainview, N.Y.) by a high-voltage capacitor (2.2 nF, 2 kV).

The resulting voltage output was sampled with a boxcar integrator (Model SR245; Stanford Research Systems, Palo Alto, CA) and processed by a personal computer.

Saturation curves were obtained by attenuation of the intensity of the laser beams with the appropriate neutral density filters.

Absorption experiments were required to calculate the QE of the detector. In this case, the signal photons were sent to a photodiode placed in the laser path after the flame. The LEI signal and the photodiode transmittance signal were then measured simultaneously while the laser was scanned through the 303.9 nm transition. The signals were fed into boxcars and computer processed.

The transimpedance amplifier was calibrated for charge integration. Rectangular voltage pulses of known amplitude (0.040 - 5.000 V) and duration (20-500 ns) were injected into a current divider,i.e., the input to the amplifier was the charge taken at the open end of a 588 kΩ resistor. The output signal was measured directly with an oscilloscope after setting the width of the boxcar gate equal to the width of the output signal (at its base). The calibration factor (V s/A s) was calculated by dividing the integrated output signal in the scope (V s) by the amount of charge injected (A s).

Results and Discussion

The In-RID was evaluated for our experimental conditions both for one step excitation and for stepwise excitation, followed by ionization through collisions in the flame.

Calibration of the Transimpedance Amplifier

The total charge injected into the amplifier was calculated using the following equation:

$$q_i = \frac{V_i t_i}{588 \times 10^3 \Omega} \qquad (22)$$

where q_i is the injected charge (C), V_i is the injected pulse voltage (V) and t_i (s) is the duration of the injected pulse.

For a nominal setting of 10^5 V/A on the amplifier the calculated calibration factor was (8.66 ± 0.52) x 10^4 V s/A s. This factor was independent of the injected pulses voltage and amplitude within the range tested.

One-step Excitation

Using a single step excitation at λ_{12} = 303.9 nm, the dependence of the LEI signal on $B_{12}\rho_\lambda(\lambda_{12})$ was evaluated. The transition could be saturated with a laser energy of 350 nJ, as shown in Figure 8. This energy value corresponds to a spectral energy density of 5.71×10^{-19} J cm^{-3} Hz^{-1}, assuming a laser bandwidth of 6.50×10^{10} Hz (20 pm), a beam diameter of 2 mm and a laser pulse width of 10 ns.

At low energy values, there is a nearly linear dependence between the LEI signal and $B_{12}\rho_\lambda(\lambda_{12})$. A log-log plot yields a slope of 1.19 for this part of the curve, as shown in Figure 9. The plateau obtained for higher laser energy values shows that at those high energy spectral density values the rate of induced absorption is much greater than the sum of radiative and collisional deactivation processes, i.e., $B_{12}\rho_\lambda(\lambda_{12}) >> (A_{21} + k_{21} + k_{2i})$.

As discussed in Chapter 2, this excitation scheme is not expected to produce any significant ionization yield, even for saturation conditons. In this scheme, the ionization yield is dependent on the product $k_{2i}\Delta t_1$. Since the laser pulse width is only 10 ns, the ionization yield depends on how large k_{2i} is, i.e., how close the excited state is to the ionization continuum level. The excited state reached by λ_{12} ($^2D_{3/2}$) lies ~1.7 eV below the ionization continuum and therefore the k_{2i} value is not expected to be sufficiently large. Energy values of ~ 3kT are a reasonable estimate for the energy that can be provided by collisional ionization schemes.

Figure 8. Saturation curve for one-step excitation of In - Linear plot.

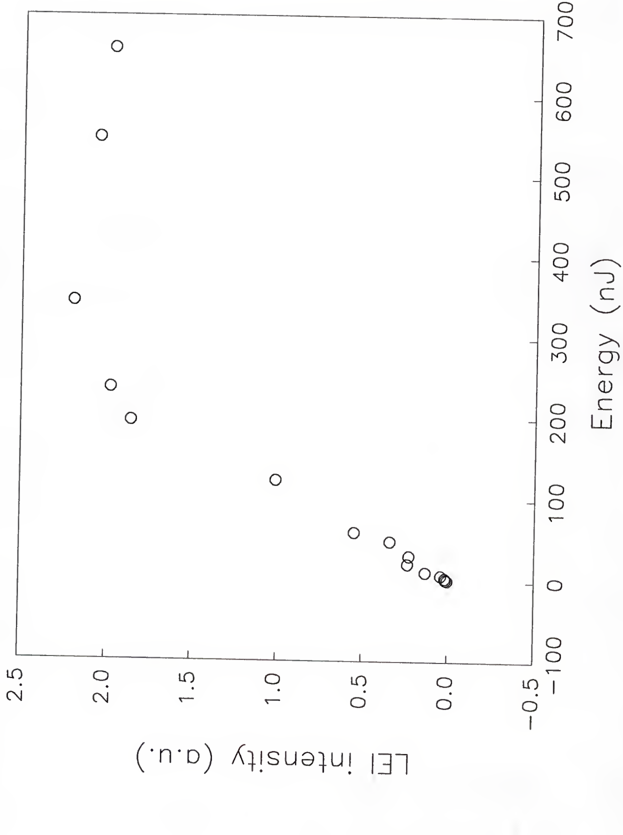
LEI intensity (a.u.)
2.5
2.0
1.5
1.0
0.5
0.0
−0.5
−100
0
100
200
300
400
500
600
700
Energy (nJ)

Figure 9. Saturation curve for one-step excitation of In - Log-log plot.

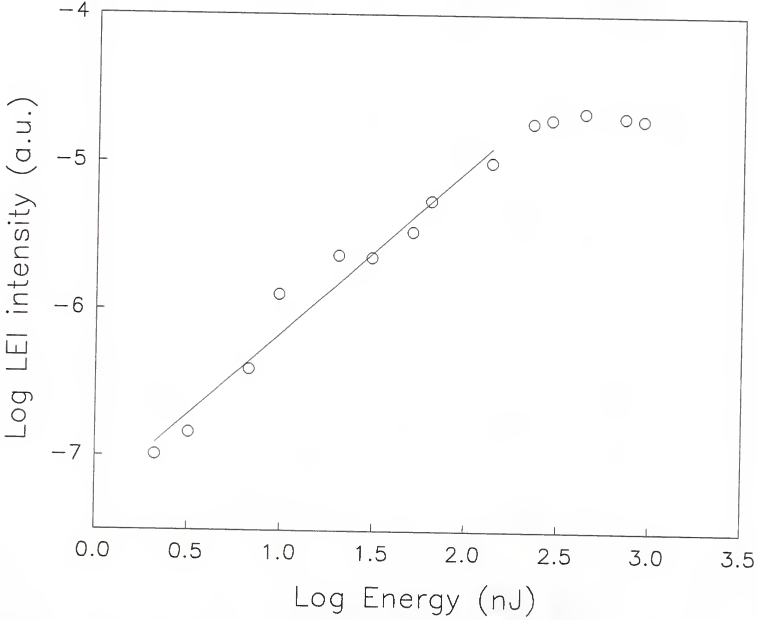
−4
−5
−6
−7
Log LEI intensity (a.u.)
0.0
0.5
1.0
1.5
2.0
2.5
3.0
3.5
Log Energy (nJ)

Step-wise Excitation

The excitation steps evaluated were λ_{12}=303.9 nm and λ_{23}=786.4 nm. The increase in LEI intensity signal was about 10 times when the second step excitation scheme was added. Saturation curves were performed for both excitation transitions.

Saturation curve for λ_{12}

The dependence of the signal on $B_{12}\rho_\lambda(\lambda_{12})$ was evaluated while having 233 μJ of energy in the second step. As can be seen in Figure 10, the transition could be saturated with a laser energy of ≈ 7 nJ, which corresponds to a spectral energy density of ≈ 1.14 x 10^{-20} J cm^{-3} Hz^{-1} if the beam diameter is assumed to be 2 mm.

The log-log plot is shown in Figure 11. For the linear portion of the curve, the slope is 1.032, showing the linear dependence of the LEI signal on $B_{12}\rho_\lambda(\lambda_{12})$. As predicted by the rate equations theory, the signal intensity becomes independent of the laser energy at higher energy levels.

Saturation curve for λ_{23}

The dependence of the LEI signal on $B_{23}\rho_\lambda(\lambda_{23})$ was evaluated while having 83 pJ of energy in the first excitation step. Figure 12 shows that saturation of the transition can be achieved with ≈ 80 μJ of energy, which corresponds to a spectral energy density of ≈ 3.89 x 10^{-16} J cm^{-3} Hz^{-1}. The conditions assumed for this calculation are that the laser

Figure 10. Saturation curve for the first excitation step in the stepwise excitation of In - Linear plot.

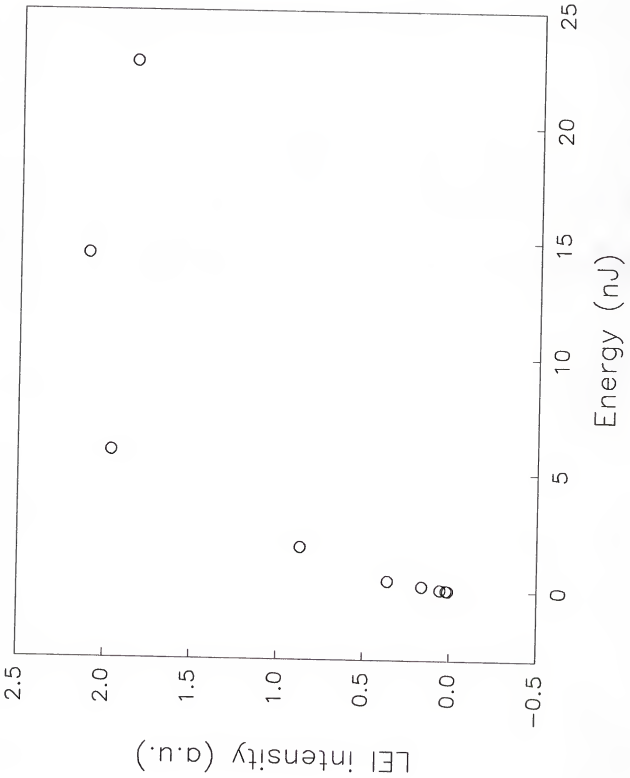
LEI intensity (a.u.)
2.5
2.0
1.5
1.0
0.5
0.0
−0.5
0
5
10
15
20
25
Energy (nJ)

Figure 11. Saturation curve for the first excitation step in the stepwise excitation of In - Log-log plot.

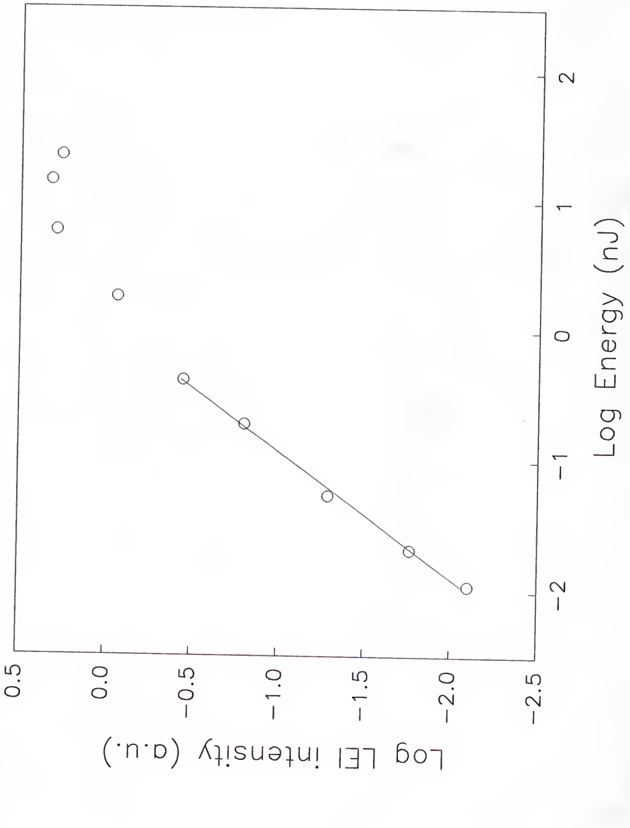
Log LEI intensity (a.u.)
0.5
0.0
−0.5
−1.0
−1.5
−2.0
−2.5
Log Energy (nJ)
−2
−1
0
1
2

Figure 12. Saturation curve for the second excitation step in the stepwise excitation of In - Linear plot.

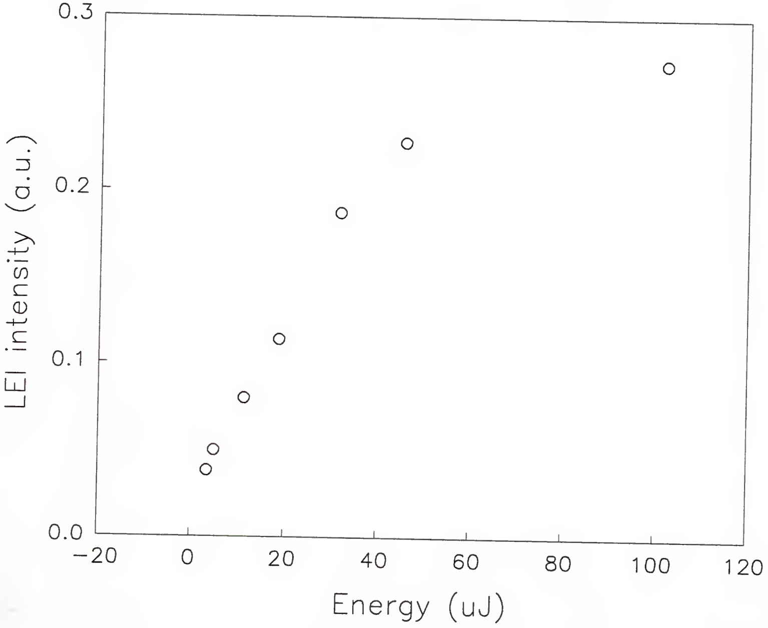
0.3
0.2
0.1
0.0
LEI intensity (a.u.)
−20
0
20
40
60
80
100
120
Energy (uJ)

Figure 13. Saturation curve for the second excitation step in the stepwise excitation of In - Log-log plot.

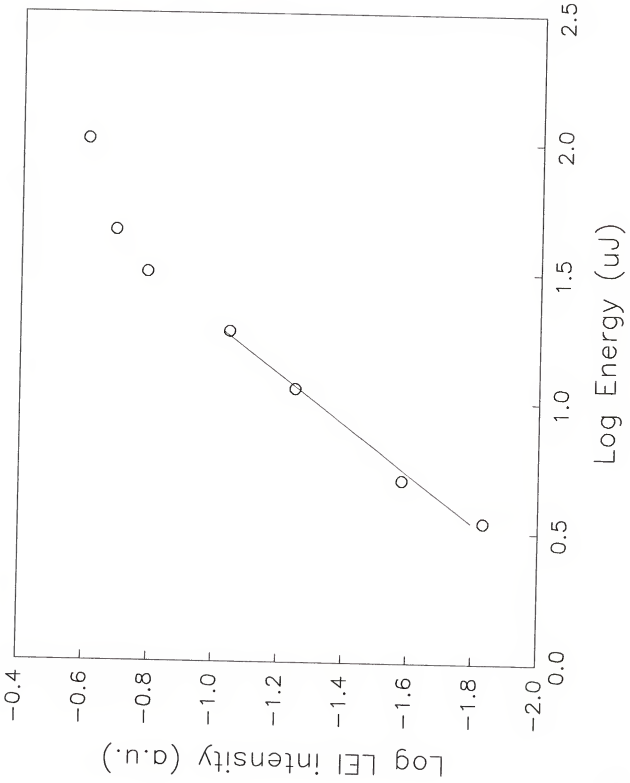
Log LEI intensity (a.u.)
-0.4
-0.6
-0.8
-1.0
-1.2
-1.4
-1.6
-1.8
-2.0
0.0
0.5
1.0
1.5
2.0
2.5
Log Energy (uJ)

bandwidth is 9.71×10^9 Hz (20 pm), beam diameter of 3 mm and laser pulse width of 10 ns.

A slope of 1.05 was obtained for the linear dependence portion of the log-log plot, shown in Figure 13. A plateau is again observed for high laser energies, when the LEI signal becomes independent of $B_{23}\rho_\lambda(\lambda_{23})$.

The condition of a photon detector is best simulated for low energy levels in transition λ_{12} and for saturation of the transition λ_{23}, i.e, energy values smaller than 7 nJ and greater than 80 μJ for each transition, respectively.

Calculation of the Quantum Efficiency

The ratio between the number of ion-pairs created in the detector and the number of incident photons is called quantum efficiency (QE). However, not all of the incident photons are absorbed by the detector. If the frequency of the signal photons is distributed over a larger frequency range than the one that can be absorbed by the detector, an effective quantum efficiency (η_i^*) can be defined:

$$\eta_i{*} = \frac{\text{number of ion-pairs created}}{\text{number of absorbed photons}} \qquad (23)$$

Therefore, the quantum efficiency is the product of the effective quantum efficiency by the fraction of absorbed photons ($[1 - \exp(-\sigma_{12}n_1l_{abs})]$, or simply α).

Experiments permitting the calculation of α were performed as described in the experimental section. Figure 14 shows a typical example of the simultaneous recording of absorption of λ_{12} and LEI signal. The value obtained for α is 0.64, i.e, 64% of the incident photons are within the absorption bandwidth of the detector.

The quantum efficiency can be calculated by dividing the number of electrons produced by the RID by the number of incident photons. Experimentally, the following formula can be used:

$$QE = m \cdot h\nu \cdot bw \cdot \frac{1}{e} \cdot \frac{1}{\alpha} \tag{24}$$

where m is the slope of the linear plot of the saturation curve for the first step in the stepwise excitation process (A J^{-1}), hν is the energy of each photon (J $photon^{-1}$), bw is the gate width of the boxcar (s), e is the electron charge (C $electron^{-1}$) and α is the absorption fraction (dimensionless). For Figure 10, m = 8,54 x 10^3 A J^{-1}, hν at 303.9 nm is 6.54 x10^{-19} J $photon^{-1}$, the width of the boxcar is 400 ns, e is 1.6 x 10^{-19} C $electron^{-1}$ and α is 0.64. The calculated QE is therefore 0.022 or 2.2%.

The value obtained for the quantum efficiency is not the ideal for a photon detector and is not comparable to the one reported in reference 39. QE values are characteristic for

Figure 14. Determination of α - Simultaneous recording of absorption of λ_{12} and LEI intensity.

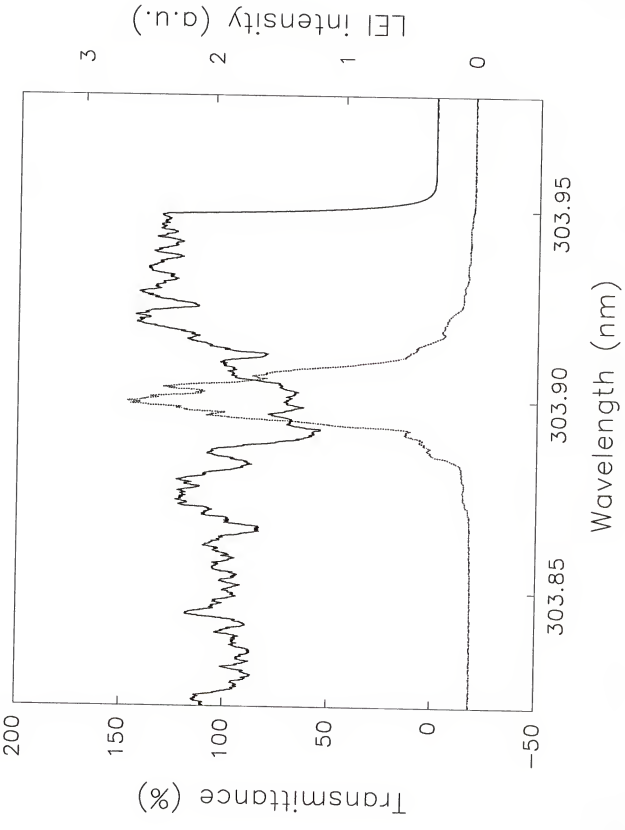
Transmittance (%)
200
150
100
50
0
−50
LEI intensity (a.u.)
3
2
1
0
303.85
303.90
303.95
Wavelength (nm)

each working system and details about the experimental conditions of reference 39 are not known. The attempts made to optimize the operating conditions in order to increase the QE were not successful. One possible source that could be contributing to the QE value is the performance of the dye laser that delivers the second excitation step. Throughout this work, the relative standard deviation of the output energy of that dye laser was ~ 30% and the beam quality was variable and not reliable. It is the author's opinion that these problems could have contributed to the result obtained for the detector's QE.

CHAPTER 4
DETECTION OF OH IN THE In-RID

Introduction

Rotational transitions of the OH radical can be assigned to the peaks shown in Figures 1 and 2. Peak assignments were made according to Dieke and Crosswhite [40] and a partial excitation spectrum of OH showing the assignments in the region ≈ 280.9 nm to 284.0 nm is depicted in Figure 15. The difference between the experimental values and those reported in reference 40 were ≤ 17 pm and therefore the accuracy was limited by the excitation laser bandwidth. The strong ionization signal observed at 283.6 nm is due to an indium transition. The same holds for the signal observed at 285.7 nm in Figure 2.

Potential mechanisms that could lead to the observation of the OH rotational transitions via LEI of indium include the capture by ground state indium atoms of fluorescence photons emitted at 303.9 nm by laser excited OH radicals and the collisional energy transfer from the laser excited OH radicals to ground state indium atoms. This chapter will focus on the work performed to characterize the OH/In-RID and to investigate its origin.

Figure 15. Partial excitation spectrum of OH showing peak assignments.

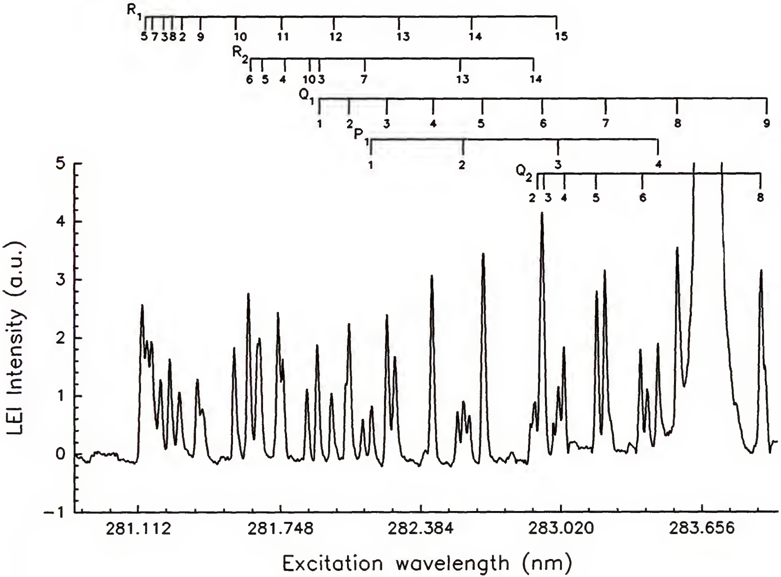
R1
5 7 3 8 2 9 10 11 12 13 14 15
R2
6 5 4 10 3 7 13 14
Q1
1 2 3 4 5 6 7 8 9
P1
1 2 3 4
Q2
2 3 4 5 6 8
LEI Intensity (a.u.)
5
4
3
2
1
0
−1
281.112
281.748
282.384
283.020
283.656
Excitation wavelength (nm)

OH Radical - General Considerations

The concentration of OH radicals in the atmosphere is estimated to be around 10^6 molecules cm^{-3} and even at these low concentrations this very active radical plays an important role in atmospheric chemistry [41]. The existence of the molecule is central to many important phenomena in galactic space and in combustion media. The study of OH is also of interest due to its role in providing fundamental information to molecular physics [42].

The existence of OH in flames is proven through the ultraviolet emission bands with a widely open structure, the strongest band head lying at 306.4 nm (0→0 vibrational band; the number on the left of the arrow corresponds to the vibrational number of the first excitated state, v′, and the number to the right of the arrow corresponds to the vibrational number of the ground state, v"). Other strong band heads lie at 281.1 nm (1→0), 287.5 nm (2→1), and 312.2 nm (1→1). Figure 16 shows a simplified energy diagram of OH major bands; the $Q_1 1$ transition of each band is depicted. The importance of OH in the kinetics of flames and related problems is recognized and the ultraviolet bands have been extensively studied [43].

The lower state of the ultraviolet emission bands is the ground state of OH, denoted $X^2\Pi$. This is an inverted doublet Π state and the component $^2\Pi_{1/2}$ lies above $^2\Pi_{3/2}$. The higher

Figure 16. Energy diagram for OH major bands; transition $Q_1 1$ from each band is represented.

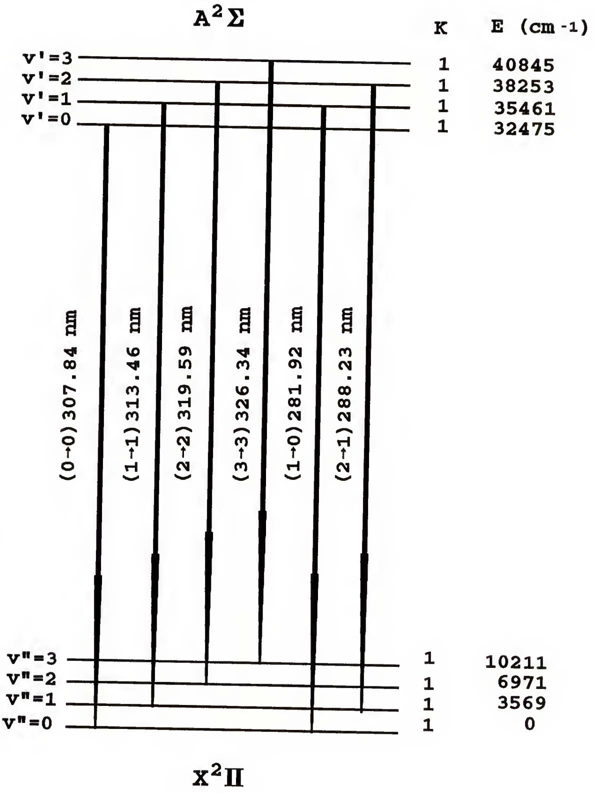
$A^2\Sigma$
K
E (cm -1)
v'=3
v'=2
v'=1
v'=0
1 40845
1 38253
1 35461
1 32475
(0→0) 307.84 nm
(1→1) 313.46 nm
(2→2) 319.59 nm
(3→3) 326.34 nm
(1→0) 281.92 nm
(2→1) 288.23 nm
v"=3
v"=2
v"=1
v"=0
1 10211
1 6971
1 3569
1 0
$X^2\Pi$

state of the ultraviolet bands is a normal doublet Σ denoted $A^2\Sigma^+$.

The rotational states of a diatomic molecule can be described by the total angular momentum or by the angular momentum K if the electronic spin is disregarded, K being always an integer. K can be used with the understanding that it represents the angular momentum without interaction of spin and with the orbital motion removed. In the OH radical, the electronic spin has the value 1/2 and thus doublets are produced. The two components of the doublets are characterized by subscripts 1 and 2 [40]:

$$F_1(K);\ f_1(K)\ :\ J = K + 1/2 \tag{25}$$

$$F_2(K);\ f_2(K)\ :\ J = K - 1/2 \tag{26}$$

F_1 and F_2 are used for the rotational levels of the $^2\Sigma$ state; f_1 and f_2 are used for the rotational levels of the $^2\Pi$ state.

For the $^2\Sigma$ state there is no resulting orbital momentum Λ along the internuclear axis and the electron spin is always coupled to the rotation axis. The two doublet components $F_1(K)$ and $F_2(K)$ nearly coincide for $K = 0$, but there is a so called ρ-type doubling for $K \neq 0$.

For the $^2\Pi$ state, Λ=1. In this circumstance, i.e., when $\Lambda \neq 0$, two extreme cases can be considered according to Hund. In case (a), the spin is coupled through the orbital angular momentum to the internuclear axis and the rotation is so slow that it does not disturb this condition. In case (b), the rotation is so strong that the spin is coupled to the rotational axis rather than the internuclear axis. There are two states, f_1 and f_2. Due to the Λ-doubling, both f_1 and f_2 are doubled; the pair of components are called f_1 and f'_1 and f_2 and f'_2. Most actual $^2\Pi$ states are close to case (a) for slow rotation and close to case (b) for fast rotation.

The selection rules for the $^2\Sigma \rightarrow {}^2\Pi$ transitions are the following: $J \rightarrow J$ and $J\pm1 \rightarrow J$; $K \rightarrow K$ and $K+1 \rightarrow K$. The J selection rule must be strictly satisfied for the free molecule for dipole transitions. The symmetry rule even ⇄ odd is also strict for the free molecule. With these rules, twelve possible branches are obtained. Transitions that satisfy both selection rules form strong branches, those that violate the K rule are weak, except for small values of K. The branches are named for case (b):

O-branch for $K-2 \rightarrow K$
P-branch for $K-1 \rightarrow K$
Q-branch for $K \rightarrow K$
R-branch for $K+1 \rightarrow K$
S-branch for $K+2 \rightarrow K$

The branches are labeled by the indices of the initial and the final levels. If both these indices are the same, it is given only once. The branches with only one index satisfy both the J and the K rule and are called the main branches. The branches with two indices are called the satellite branches.

According to Dieke and Crosswhite [40], the twelve possible branches are:

$$O_{12}(K) = F_1(K-2) - f'_2(K) \qquad J-1 \rightarrow J \tag{27}$$

$$P_1(K) = F_1(K-1) - f_1(K) \qquad J-1 \rightarrow J \tag{28}$$

$$P_2(K) = F_2(K-1) - f_2(K) \qquad J-1 \rightarrow J \tag{29}$$

$$P_{12}(K) = F_1(K-1) - f_2(K) \qquad J \rightarrow J \tag{30}$$

$$Q_1(K) = F_1(K) - f'_1(K) \qquad J \rightarrow J \tag{31}$$

$$Q_{21}(K) = F_2(K) - f'_1(K) \qquad J-1 \rightarrow J \tag{32}$$

$$Q_2(K) = F_2(K) - f'_2(K) \qquad J \rightarrow J \tag{33}$$

$$Q_{12}(K) = F_1(K) - f'_2(K) \qquad J+1 \rightarrow J \tag{34}$$

$$R_1(K) = F_1(K+1) - f_1(K) \qquad J+1 \rightarrow J \tag{35}$$

$$R_{21}(K) = F_2(K+1) - f_1(K) \qquad J \rightarrow J \tag{36}$$

$$R_2(K) = F_2(K+1) - f_2(K) \qquad J+1 \rightarrow J \tag{37}$$

$$S_{21}(K) = F_2(K+2) - f'_1(K) \qquad J+1 \rightarrow J \tag{38}$$

Experimental

The system described previously in Chapter 3 was used. All the conditions and parameters used were the same unless specified otherwise.

The studies were carried out mostly in the small burner mentioned in Chapter 3. A circular 1 cm o.d. burner consisting of a bundle of 75 stainless steel capillaries (0.06 mm i.d.) mounted in a conventional atomic absorption premixed spray chamber was also used for some tests. In this case, the indium solution was aspirated and nebulized with a pneumatic nebulizer.

The fluorescence experiments were performed using a 0.22 m focal length double monochromator (Model 1680B, Spex Industries, Edison, NJ).

In order to obtain more energy for the OH excitation step, the beam expander was removed from the system for detection of OH using the In-RID. However, this first excitation laser was still reduced to 2 mm diameter before reaching the flame.

Lenses of appropriate focal lengths (a pair with f=1 m and f=0.5 m for each dye laser) were used to improve the beam quality of the laser beams that reached the flame. This was done by imaging in the flame the laser beam observed immediately after the end window of the amplifier cell of the dye laser cavity. This physical arrangement tremendously improved the quality of the beams at the flame and made alignment of the two laser beams easier.

Results and Discussion

The experiments performed may be grouped into two main categories: optimization studies and investigation of possible mechanisms for the phenomenon observed.

Optimization Studies

Saturation curves were obtained to investigate the dependence of the observed signal on the laser spectral energy density. The applied high voltage to the collection electrode was - 1700 V and the concentration of the nebulized indium solution was 1%.

Saturation curve for λ_{exc} in the absence of λ_{23}

Using a single step excitation of $\lambda_{exc}=Q_15=282.6674$ nm the dependence of the LEI signal on the laser energy was evaluated. As shown in Figure 17, the laser energy was varied from ≈ 3 to 260 μJ, which was the maximum power attainable at the flame. Figure 18 shows the log-log plot of this saturation curve; it can be seen that throughout the whole range of the laser energies employed, a linear dependence is observed, the slope of the curve being equal to 0.99. The excitation photons used could not produce a sufficient number of signal photons at $\lambda_{12}=303.9$ nm to saturate the first excitation step of the In-RID.

Saturation curve for $\lambda_{23}=786.44$ nm in the absence of λ_{exc}

Figure 19 shows the dependence of the LEI signal on $B_{23}\rho_\lambda(\lambda_{23})$ in the absence of the first excitation laser. The laser energy was varied from ≈ 245 μJ to ≈ 5 mJ; the transition could be saturated with a laser energy of ≈ 3 mJ. This energy value corresponded to a spectral energy density of 1.46×10^{-14} J cm^{-3} Hz^{-1}, assuming that the laser bandwidth was 9.71×10^9 Hz (20 pm), the beam diameter was 3 mm and the laser pulse width was 10 ns.

A slope of 0.97 was obtained for the linear dependence portion of the log-log plot, shown in Figure 20. The initial

Figure 17. Saturation curve for λ_{exc}=$Q_1$5=282.6674 nm in absence of λ_{23} - Linear plot.

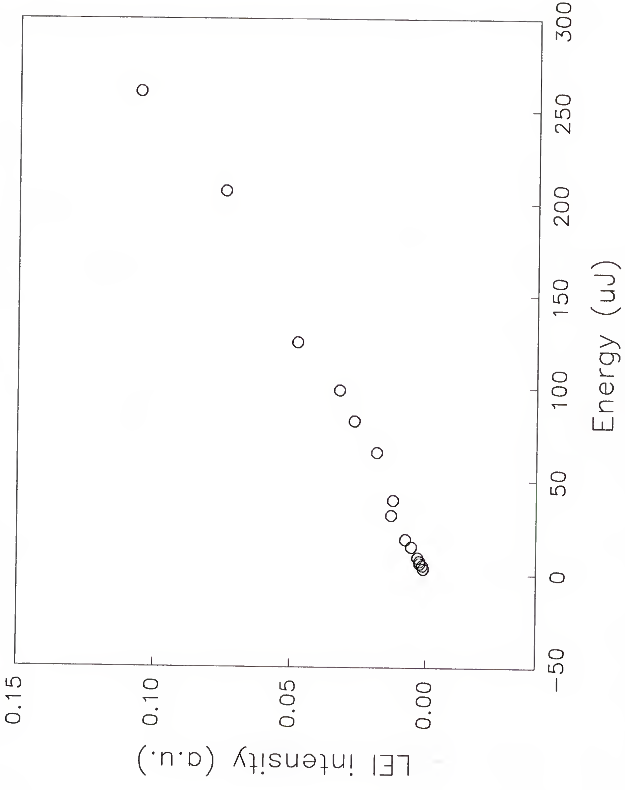
LEI intensity (a.u.)
0.15
0.10
0.05
0.00
Energy (uJ)
−50
0
50
100
150
200
250
300

Figure 18. Saturation curve for $\lambda_{exc}=Q_15=282.6674$ nm in absence of λ_{23} - Log-log plot.

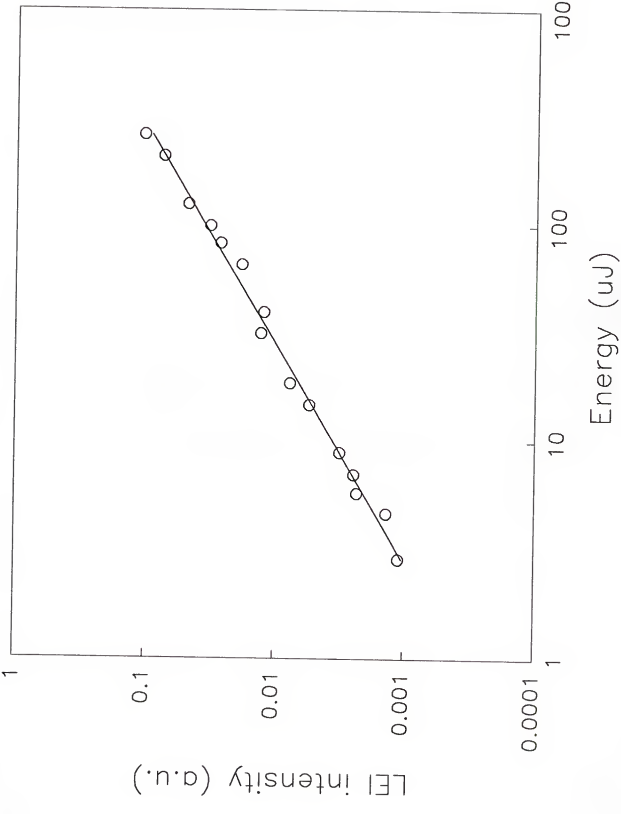
LEI intensity (a.u.)
1
0.1
0.01
0.001
0.0001
Energy (uJ)
1
10
100
1000

Figure 19. Saturation curve for λ_{23}=786.44 nm in absence of λ_{exc} - Linear plot.

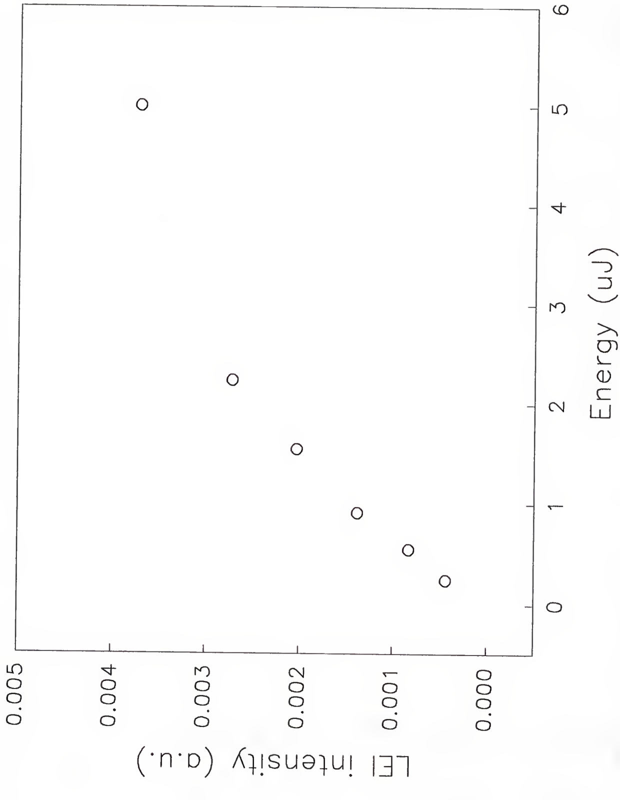
LEI intensity (a.u.)
0.000
0.001
0.002
0.003
0.004
0.005
Energy (uJ)
0
1
2
3
4
5
6

Figure 20. Saturation curve for λ_{23}=786.44 nm in absence of λ_{exc} - Log-log plot.

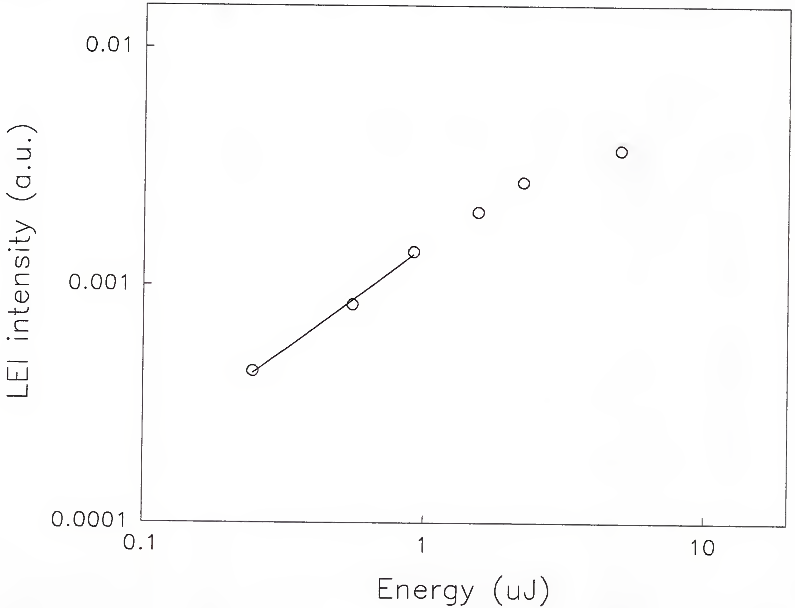
0.01
0.001
0.0001
LEI intensity (a.u.)
0.1
1
10
Energy (uJ)

portion of a plateau can be observed for high laser energies, when the signal becomes independent of $B_{23}\rho_\lambda(\lambda_{23})$.

Saturation curve for λ_{exc} in the presence of λ_{23}

The dependence of the signal on the laser energy of λ_{exc}=$Q_1$5=282.6674 nm was studied while keeping the second excitation laser at λ_{23}=786.44 nm. The energy of the first excitation laser energy was varied from ≈ 1 μJ to ≈ 300 μJ, as can be seen Figure 21, and the second excitation laser energy was ≈ 5 mJ. There was no evidence of optical saturation of the transition with the maximum energy of ≈ 300 μJ attainable at the flame.

The log~log plot is shown in Figure 22. The slope of the curve is 0.90 and the signal is linearly dependent on the first excitation laser energy within the energy range studied.

Saturation curve for λ_{23} in the presence of λ_{exc}

While keeping the first excitation laser at ≈ 300 μJ for λ_{exc}=$Q_1$5=282.6674 nm, the dependence of the signal on the second excitation energy was evaluated. The second laser was kept at λ_{23}=786.44 nm, and the energy values were varied from 3.5 μJ to 5.3 mJ. Figure 23 shows that the transition could be saturated with ≈ 2.5 mJ of energy, which corresponds to a spectral energy density of 1.22×10^{-14} J cm^{-3} Hz^{-1}, assuming a laser bandwidth of 9.71×10^9 Hz (20 pm), a beam diameter of 3 mm and a laser pulse width of 10 ns.

Figure 24 shows the log~log plot and the linear interaction that exists at small energy values. The slope for

Figure 21. Saturation curve for $\lambda_{exc}=Q_15=282.6674$ nm in presence of $\lambda_{23}=786.44$ nm - Linear plot.

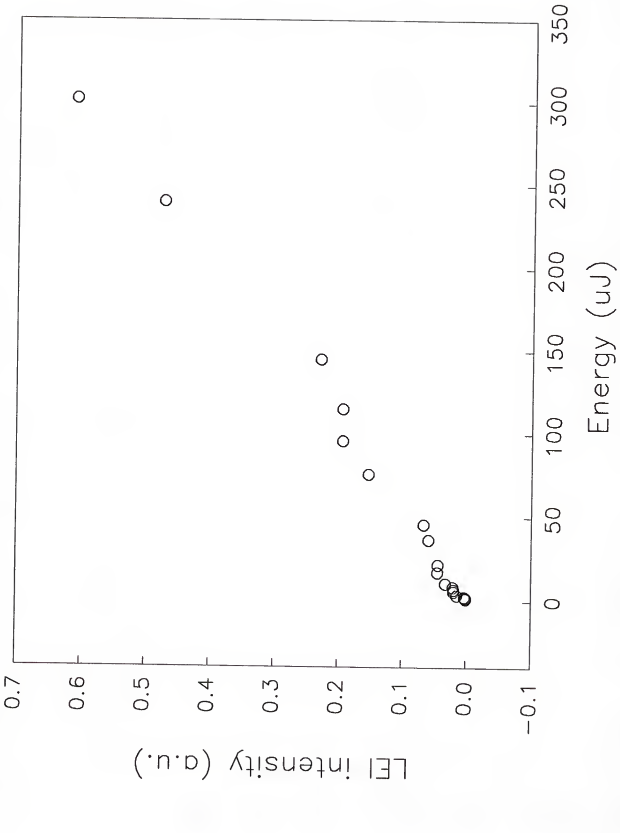

LEI intensity (a.u.)
-0.1
0.0
0.1
0.2
0.3
0.4
0.5
0.6
0.7
Energy (uJ)
0
50
100
150
200
250
300
350

Figure 22. Saturation curve for $\lambda_{exc}=Q_15=282.6674$ nm in presence of $\lambda_{23}=786.44$ nm - Log-log plot.

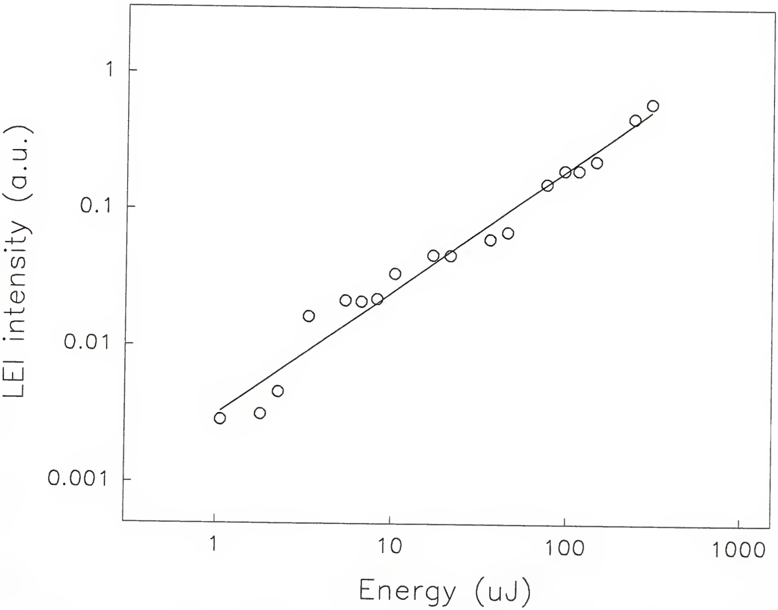
LEI intensity (a.u.)
1
0.1
0.01
0.001
1
10
100
1000
Energy (uJ)

Figure 23. Saturation curve for λ_{23}=786.44 nm in presence of λ_{exc}=$Q_1 5$=282.6674 nm - Linear plot.

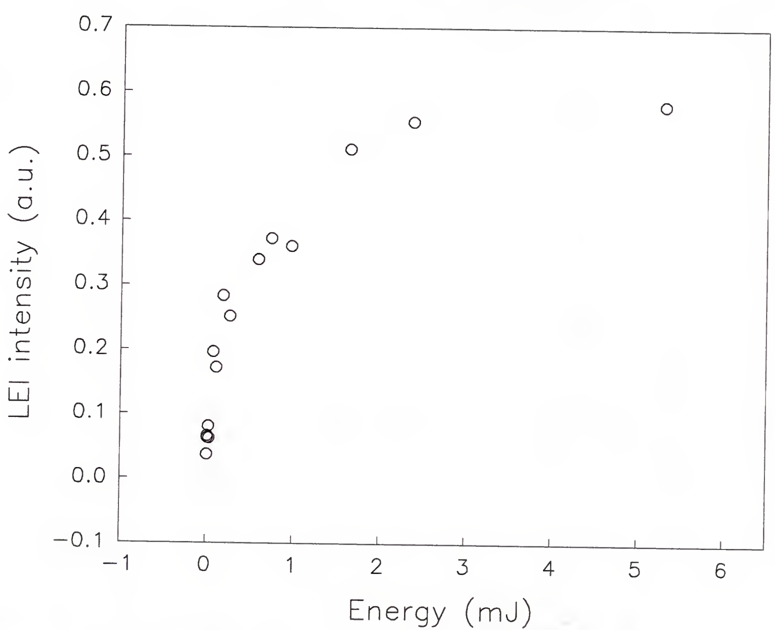
0.7
0.6
0.5
0.4
0.3
0.2
0.1
0.0
−0.1
LEI intensity (a.u.)
−1
0
1
2
3
4
5
6
Energy (mJ)

Figure 24. Saturation curve for λ_{23}=786.44 nm in presence of λ_{exc}=$Q_1$5=282.6674 nm - Log-log plot.

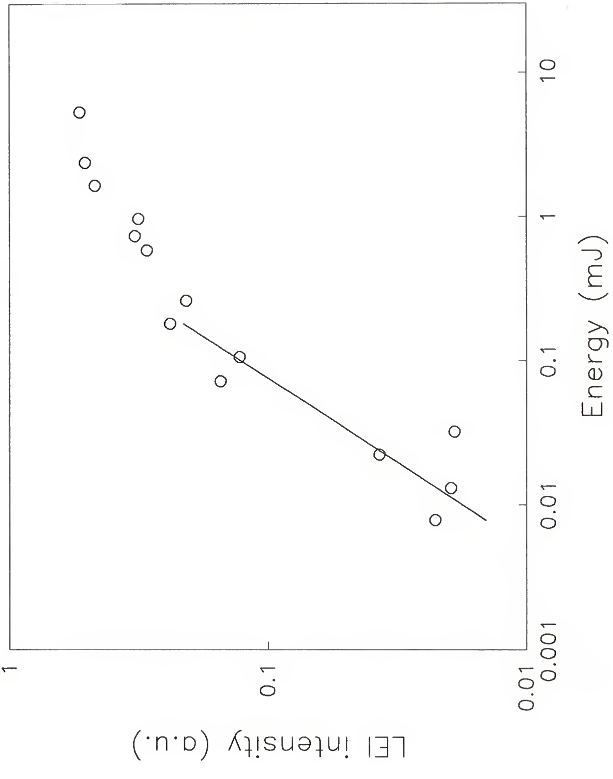
LEI intensity (a.u.)
1
0.1
0.01
0.001
0.01
0.1
1
10
Energy (mJ)

that part of the curve is 0.86. The plateau obtained for higher laser energies shows that the signal becomes independent of $B_{23}\rho_{\lambda}(\lambda_{23})$ at high spectral energy density values.

As a result of the experiments discussed above, the first excitation laser (λ_{exc}) was used with no attenuation for the following optimization studies, since saturation of that process was never achieved at the maximum power outputs that were attainable at the flame. The second excitation step (λ_{23}) could be saturated with ≈ 2.5 mJ of energy. However, besides exhibiting a bad beam quality, the dye laser output energy precision was extremely poor throughout this whole work; the relative standard deviation was of the order of 30 - 40%. For comparison purposes, the output energy precision obtained with the other dye laser was around 10% for the fundamental of the dye and 19% for the ultraviolet beam when tracking; these values can be considered typical for our system. Therefore, even at the expense of probably adding noise to the signal, the full beam with no attenuation was used for the second excitation step in the following experiments.

Effect of high voltage

The dependence of the LEI signal on the high voltage (HV) applied to the electrode was studied by varying the applied HV from -200 to - 1700 V. The first excitation step was $\lambda_{exc}=Q_1 5=282.6674$ nm with ≈ 300 μJ; the second excitation step was $\lambda_{23}=786.44$ nm with ≈ 5.3 mJ. Figure 25 shows that the

Figure 25. Effect of the high-voltage applied to the collection electrode on the LEI signal.

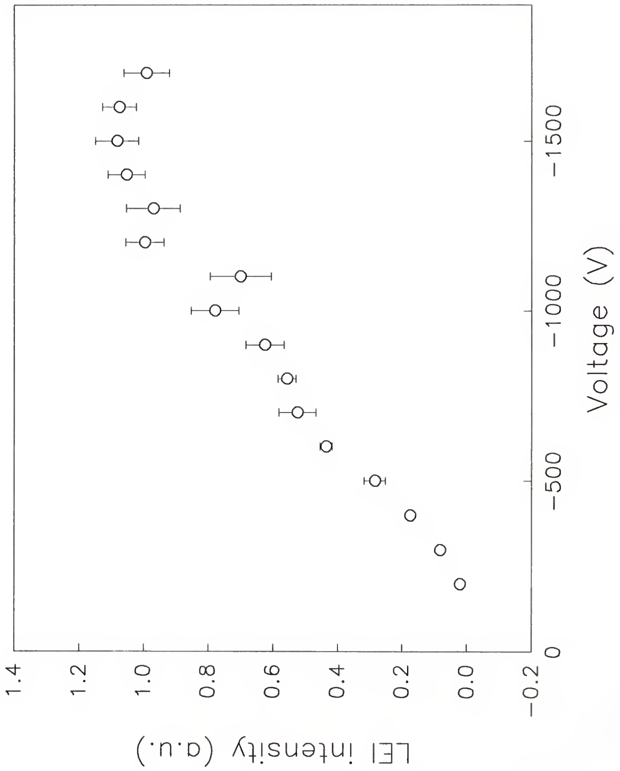
LEI intensity (a.u.)
1.4
1.2
1.0
0.8
0.6
0.4
0.2
0.0
−0.2
0
−500
−1000
−1500
Voltage (V)

signal intensity increased when the HV increased from -200 V to -1300 V. A steady signal intensity was obtained from -1300 to -1600 V and a small decrease was observed when HV = -1700 V. This decrease in signal was probably due to a perturbation of the electrical field existing between the cathode and the anode by the utilization of an excess potential that modifies the collection efficiency of the system. The plateau region, between -1300 and -1600 V shows the region of choice for further experiments, since the signal is not affected by small changes in the applied voltage. On the other hand, if the applied voltage is reasonably constant, other regions of the curve at higher applied HV may also be used without decreasing the signal intensity significantly.

Effect of the concentration of the indium solution

The effect of the concentration of the indium solution on the signal intensity can be observed in Figure 26. The conditions for the excitation steps were similar to the ones described for the HV studies. There was an approximate linear increase of the signal with the increase of indium concentration up to [In] ≈ 2%. Higher indium concentrations led to a decrease of the signal intensity. This problem could have been caused by fouling of the cathode by increasing the amount of indium deposited on the electrode, which could have decreased the collection capability of the system. The solution with an indium concentration of 2% gave the highest signal intensity. However, the signal to noise ratio for the

Figure 26. Effect of the concentration of the nebulized indium solution on the LEI signal.

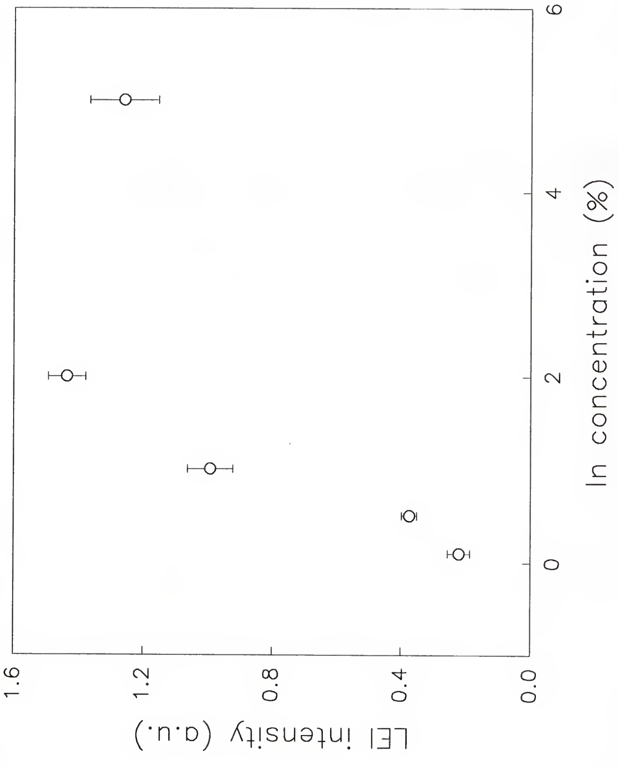
LEI intensity (a.u.)
0.0
0.4
0.8
1.2
1.6
In concentration (%)
0
2
4
6

whole range of concentrations studied was approximately constant (S/N ≈ 7), which made the choice of the concentrations used less critical. The concentrations normally used in our studies were 1% and 2%.

Effect of the power applied to the ultrasonic nebulizer

The incident power applied to the ultrasonic nebulizer was varied from 5 to 35 W. The effect of this variation on the signal intensity is shown in Figure 27. The conditions for the laser excitation steps were described in the HV studies. The signal intensity increased with increase of incident power, becoming approximately constant and maximal when the power reached 30 W. Therefore, 30 W was chosen for the following experiments, because at power values of 35 W and more, the top of the flame was perturbed by excessive nebulization. At an incident power of 30 W, the minimum achievable reflected power was ≈ 6 W and could not be decreased.

Effect of gas flow rates in the flame

The effect of different flow rates of air on the LEI signal were tested for two different flow rates of acetylene, 108 and 131 $cm^3 min^{-1}$, as shown in Figure 28. Higher signals were obtained for the lower flow rate of acetylene studied, 108 $cm^3 min^{-1}$; as the air flow rate increased from 480 to 720 $cm^3 min^{-1}$, an increase in the signal intensity was observed. The signal was steady from 720 to 860 $cm^3 min^{-1}$, and therefore the rates of 108 $cm^3 min^{-1}$ for the acetylene and 800 $cm^3 min^{-1}$ for the air were chosen for all subsequent experiments. This

Figure 27. Effect of the incident power applied to the ultrasonic nebulizer to the LEI signal.

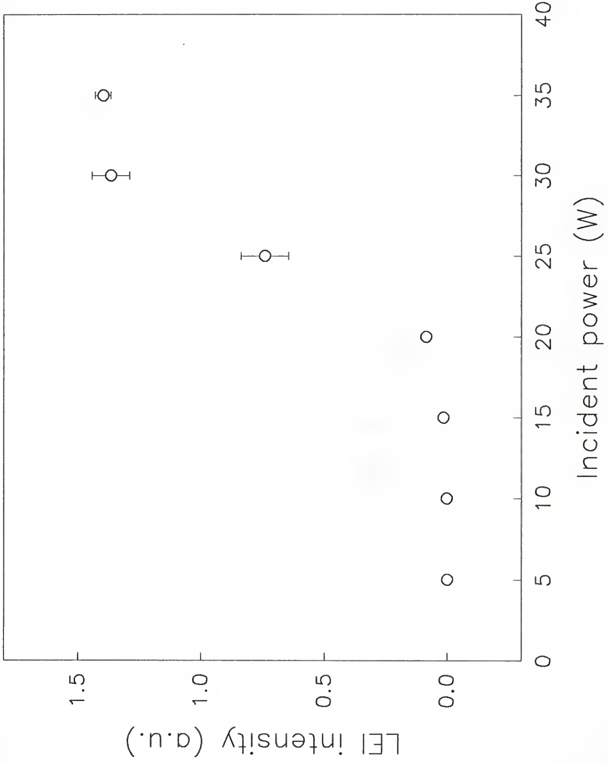
LEI intensity (a.u.)
1.5
1.0
0.5
0.0
Incident power (W)
0
5
10
15
20
25
30
35
40

Figure 28. Effect of the gas flow rates on the LEI signal:
- square: acetylene = 108 cm^3 min^{-1}
- circle: acetylene = 131 cm^3 min^{-1}.

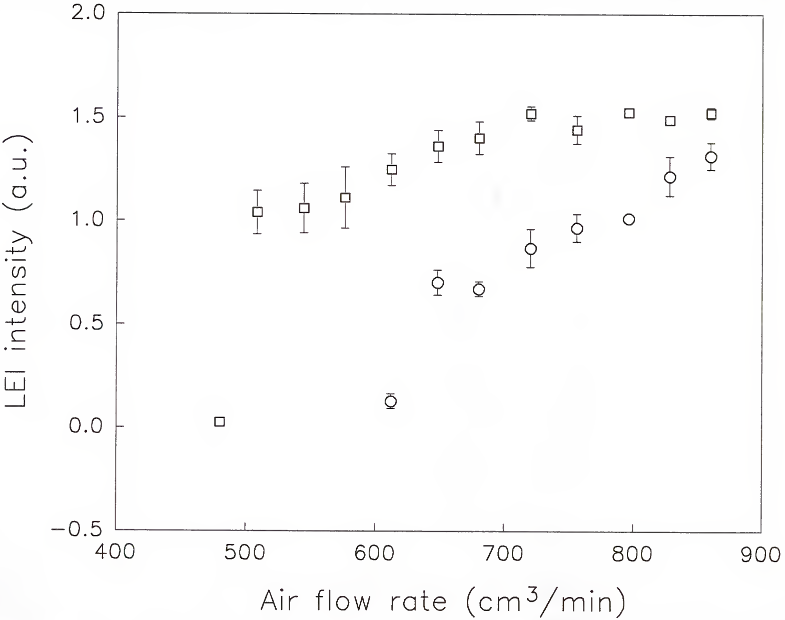
2.0
1.5
1.0
0.5
0.0
−0.5
400
500
600
700
800
900
LEI intensity (a.u.)
Air flow rate (cm³/min)

corresponds to a ratio of oxygen/acetylene of 1.6; therefore the flame used in our experiments was fuel lean, since the ratio for the stoichiometric flame is 1.0.

Expansion of the region scanned

The OH band that was excited with the first λ_{exc} is at 281 nm (1→0). An attempt was made to obtain an expanded LEI spectrum by changing the laser dye and exciting the strongest OH band at 306 nm (0→0); however, only broad features with no structure were observed. The laser dye was again changed and an intermediate region, between 289.3 and 298.2 nm was scanned. This scanned region enabled us to evaluate whether the system was working well; some of the peaks at the far end of the first scan (Figure 2), $P_1$11 (1→0) at 287.5513 nm for example, could be observed. On the other hand, no OH structures could be seen from 289.3 to 297.2 nm, as shown in Figure 29. The peaks observed at ≈ 293.3 and 295.7 corresponded to In(I) lines. If the spectrum is enlarged as in Figure 30, some features can be observed. Those features could be either real OH structures masked by the huge In lines in the region or only featureless structures related to random noise in the system.

Studies in a 1 cm pathlength flame

Several attempts were made to obtain a OH excitation spectrum using the In-RID in a conventional 1 cm pathlength flame with argon shield. It was expected that the presence of the argon shield would stabilize the flame and minimize

Figure 29. Expanded excitation spectrum in the flame In-RID.

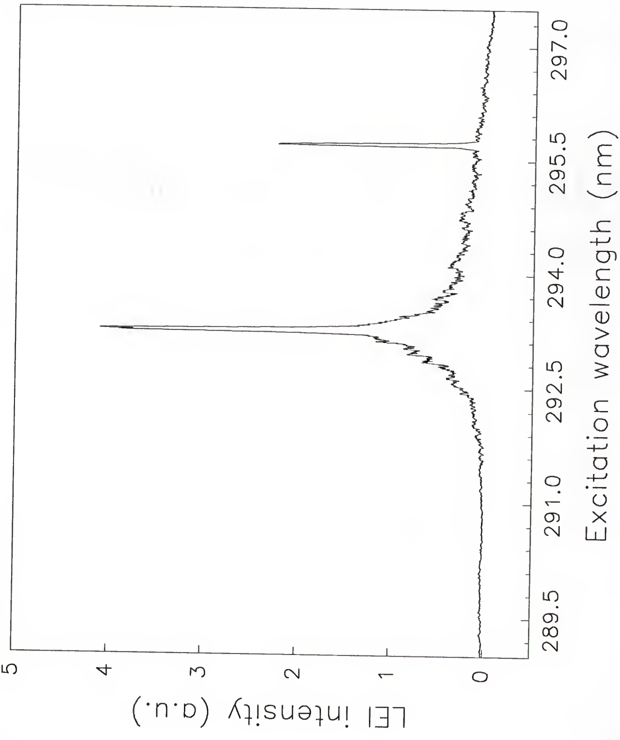
LEI intensity (a.u.)
0
1
2
3
4
5
Excitation wavelength (nm)
289.5
291.0
292.5
294.0
295.5
297.0

Figure 30. Expanded excitation spectrum in the flame In-RID - Enlargement.

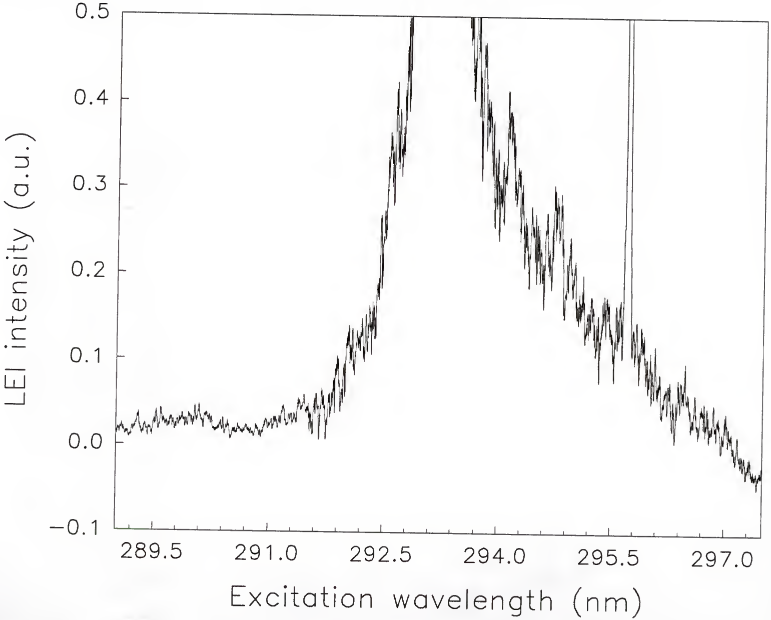
0.5
0.4
0.3
0.2
0.1
0.0
−0.1
LEI intensity (a.u.)
289.5
291.0
292.5
294.0
295.5
297.0
Excitation wavelength (nm)

variations in peak heights due to perturbations of the flame by molecules of OH present in the surrounding environment. This flame would also be more practical, because the use and replacement of In solutions would be greatly facilitated by the utilization of a conventional pneumatic nebulizer. The signal to noise ratio in this flame was very small and the resolution of the spectra obtained was not satisfactory. The majority of the OH lines could not be resolved. The limiting noise in this system was radio-frequency (RF) pick-up noise, with a magnitude of ≈ 1 V peak to peak. Therefore, it was decided to change the system back to the small burner used previously, since one of its main advantages was the low RF noise pick-up. In order to facilitate the changing of solutions, a small peristaltic pump was added to the nebulization system. This pump delivered small droplets of In solution from an external reservoir to the surface of the transducer of the ultrasonic nebulizer. The external reservoir could be filled and replaced easily.

Optimization of the second excitation laser in the OH/In-RID

The second excitation laser used for the regular In-RID described in Chapter 3 was adjusted to λ_{23}=786.44 nm. This transition was chosen because it gave the best signal when the first excitation step was $\lambda_{exc}=\lambda_{12}$=303.9 nm. In the OH/In-RID system, the second excitation laser was scanned from 740.01 nm to 792.92 nm while keeping $\lambda_{exc}=Q_1 5$=282.6674 nm. The spectrum observed is shown in Figure 31. The transition at 786.44 nm has one of the highest intensities. It also has the advantage of being fairly well resolved from the other lines and so is indeed a good choice as the second step excitation for the OH/In-RID. It is worthwhile mentioning that the spectrum shown in Figure 31 is very similar to the one obtained when the second excitation step was scanned in the regular In-RID.

Investigation of Mechanisms

After the unexpected peaks shown in Figures 1 and 2 were assigned to the OH radical, several experiments were performed to investigate the origin of the observed transitions.

The role of indium in the detection of OH was evaluated by nebulizing water instead of indium solution into the flame. No LEI signal was observed. Furthermore, when λ_{23} was detuned towards the blue by approximately 0.1 nm, a decrease in signal intensity of $\approx$ 1 order of magnitude was observed. In the absence of λ_{23} and with λ_{exc} attenuated 10 times, no LEI signal could be observed. The LEI signal was indeed a result of a stepwise excitation process of indium atoms.

Determination of the indium absorption linewidths

The indium absorption linewidths were determined by nebulizing indium solution into the flame and slowly scannning λ_{exc} over the In(I) 303.9 nm line while recording the LEI signal. The resulting peak was fitted with a Gaussian function

Figure 31. Second step (λ_{23}) excitation spectrum in the OH/In-RID with $\lambda_{exc}=Q_15=282.6674$ nm:

a) 740.01 - 767.40 nm
b) 767.40 - 792.92 nm

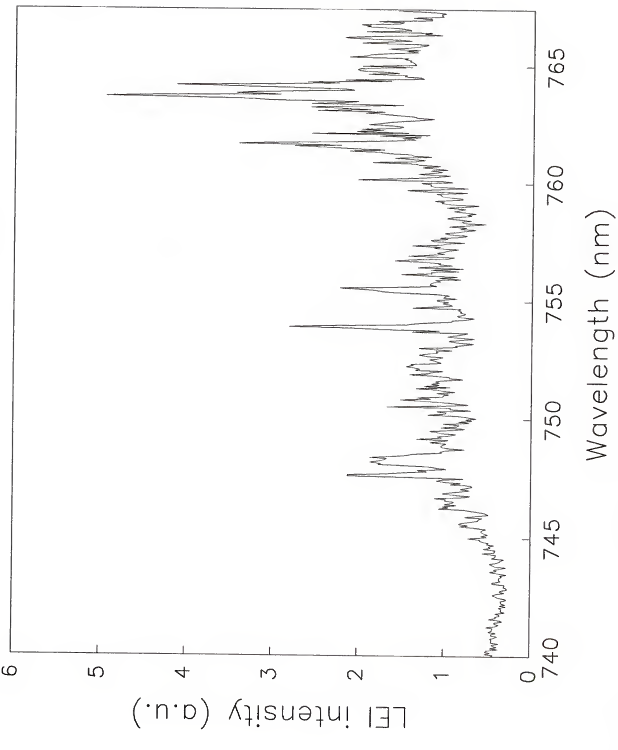
LEI intensity (a.u.)
0
1
2
3
4
5
6
740
745
750
755
760
765
Wavelength (nm)

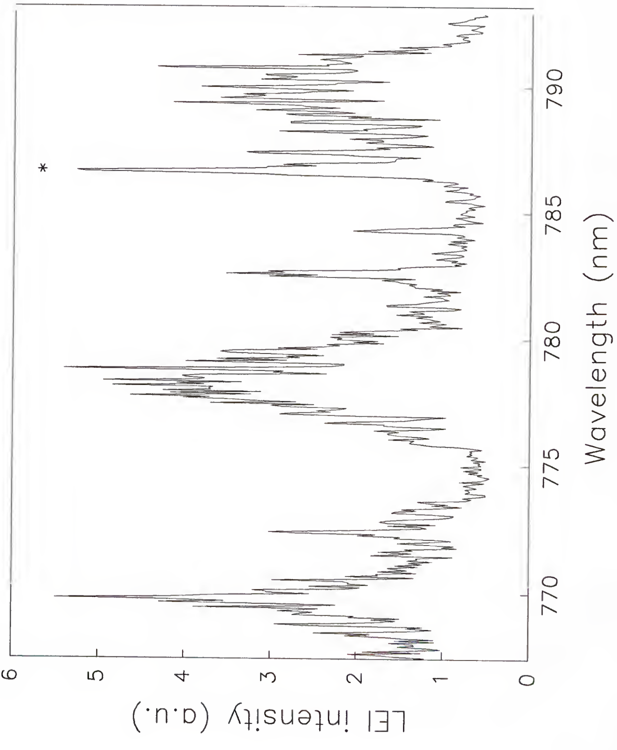
LEI intensity (a.u.)
0
1
2
3
4
5
6
Wavelength (nm)
770
775
780
785
790
*

and the peak width at half of the intensity (FWHM) was measured. This measured value is a convolution of our "real" laser linewidth and the indium linewidth at 303.9 nm in an air-acetylene flame, as can be seen in Equation 39:

$$\Delta\lambda_{tot} = [(\Delta\lambda_L)^2 + (\Delta\lambda_{In})^2]^{1/2} \qquad (39)$$

where $\Delta\lambda_{tot}$ is the total linewidth experimentally measured, $\Delta\lambda_L$ is the actual laser linewidth and $\Delta\lambda_{In}$ is the indium linewidth at 303.9 nm in an atmospheric pressure air-acetylene flame. The value used for $\Delta\lambda_{In}$ was 2 pm [44].

The linewidths could be calculated for three different experimental conditions. For conditions of low laser intensity (Q_λ = 2.4 nJ) and for low concentration of In (100 ppm), the measured $\Delta\lambda_{tot}$ was 11.44 ± 0.53 pm; therefore the actual laser linewidth $\Delta\lambda_L$ was 11.26 ± 0.53 pm.

For conditions of high concentration of indium ([In]=1% or 10000 ppm) and low laser intensities (Q_λ = 2.4 nJ), the indium absorption linewidth is concentration broadened and equation 40 applies:

$$\Delta\lambda_{tot} = [(\Delta\lambda_L)^2 + (\Delta\lambda_c)^2]^{1/2} \qquad (40)$$

where $\Delta\lambda_c$ is the indium absorption linewidth broadened by the high concentration of indium. The experimental $\Delta\lambda_{tot}$ measured was 15.53 ± 1.42 pm. Since $\Delta\lambda_L$ = 11.26 ± 0.53 pm, the calculated value of $\Delta\lambda_c$ was 10.70 ± 1.52 pm.

For conditions of high concentration of indium ([In]=1% or 10000 ppm) and high laser intensities (Q_λ = 130 μJ), the indium linewidth is concentration broadened and laser intensity broadened:

$$\Delta\lambda_{tot} = [(\Delta\lambda_L)^2 + (\Delta\lambda_c^i)^2]^{1/2} \tag{41}$$

where $\Delta\lambda_c^i$ is the indium absorption linewidth broadened both by absorption due to the high concentration of indium and due to the high laser intensity. The experimental $\Delta\lambda_{tot}$ measured was 32.66 ± 3.90 pm. Since $\Delta\lambda_L$ = 11.26 ± 0.53 pm, the calculated value of $\Delta\lambda_c^i$ was 30.65 ± 3.94 pm. This value describes better the indium absorption linewidth for the experimental conditions used in most of the present work.

Fluorescence mechanism

Based on the above results, a mechanism based on capture of fluorescence photons was proposed; the proposed mechanism is shown schematically in Figure 32. A photon at 282.667 nm was utilized as an example of one of the λ_{exc} values employed in our system. The mechanism can be explained as follows. The OH is excited from one of the rotational levels of the zero vibrational level (v"=0) of the ground state ($X^2\Pi$) to one of the rotational levels of the first vibrational level (v'=1) of the excited state $A^2\Sigma^+$. From the level v'=1, the excited OH molecules are collisionally redistributed to other rotational and vibrational levels. One level that can be possibly populated by this means is the K'=25 rotational level of the

Figure 32. Schematic diagram of the proposed fluorescence capture mechanism.

Fluorescence Capture

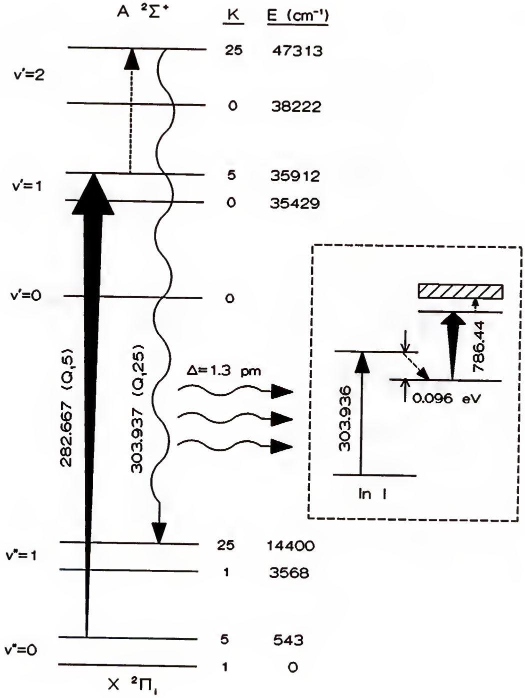

second vibrational level (v′=2) of $A^2\Sigma^+$ state. This excited level is optically coupled with the K"=25 rotational level of the first vibrational level (v"=1) of the ground state by the emission of a fluorescence photon at 303.9373 nm (transition $Q_1$25 of the 2 → 1 band). The emitted radiation is 1.3 pm away from the first excitation step used in the In-RID, which is 303.9360 nm. The absorption bandwidth of the detector in our experimental conditions, determined in an experiment already described, was found to be approximately 30 pm. Therefore, essentially all photons emitted by the $Q_1$25 transition will fall within the detector bandwidth and will be utilized as the first excitation step for the In-RID. The detector exhibits the high spectral selectivity characteristic of resonant monochromators. Other events such as Raman and Rayleigh scattering, which produce photons falling out of the detector bandwidth, are not detected.

The proposed mechanism was corroborated by the excitation spectrum of nebulized water shown in the lower part of Figure 33. The first laser λ_{exc} was scanned from ≈ 280.55 to 282.8 nm and the fluorescence emitted by water was imaged into a double monochromator set at the wavelength of 303.9 nm. Because of the poor S/N, spectrometer slits of 500 μm were used; therefore, the spectral bandpass was 0.9 nm, which greatly degraded the resolution. The upper part of Figure 33 is a portion of the spectrum shown in Figure 2; it is included in Figure 33 only for comparison purposes. The correspondence

Figure 33. Partial excitation spectrum of OH using:

- Lower trace: a double monochromator (bandpass = 0.9 nm) set to 303.9 nm
- Upper trace: the In-RID.

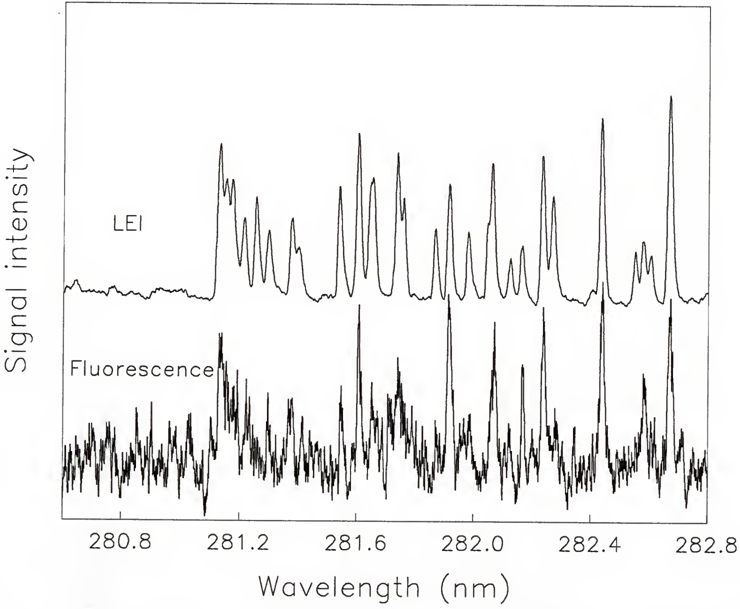
LEI
Fluorescence
Signal intensity
280.8
281.2
281.6
282.0
282.4
282.8
Wavelength (nm)

between the two spectra is evident. The poor S/N ratio obtained with the monochromator is probably related to the low intensity of fluorescence photons for the OH $Q_1$25 transition of the 2 → 1 band. Fluorescence spectra showing an excellent S/N ratio were later obtained for the 0 → 0 band of OH.

While nebulizing only water, the dependence of the fluorescence signal on the energy intensity of λ_{exc}=282.6674 nm ($Q_1$5 line of 1→0 band) was evaluated. The monochromator was set at 303.9 nm to detect photons produced at $Q_1$25 (2→1 band). Figure 34 shows that with the laser energies employed (≈ 26 to 220 μJ) no saturation conditions for production of fluorescence photons were achieved. This linear dependence of the fluorescence signal with the laser energy gave a slope of 0.98 for the log-log plot, which is shown in Figure 35. Therefore, assuming the verity of the fluorescence mechanism, it can be inferred that higher intensities in the LEI signal could be achieved if a higher energy output was available.

An emission spectrum was obtained while nebulizing water into the flame. The signal was collected at an angle of 90°. The excitation wavelength was 282.6674 nm ($Q_1$5 of the 1→0 band) and the monochromator was scanned from 279.8 nm to 309.8 nm, as depicted in Figure 36. The huge peak at ≈ 282.7 nm is due to laser scattering. The spectrum obtained is almost featureless, but higher signal intensities are obtained for the region around 306.4 and 308.7 nm, which can be associated with the strong 0 → 0 band of OH. The intensity of the signal

Figure 34. Saturation curve for fluorescence signal at 303.9 nm while nebulizing water, λ_{exc}= $Q_1 5$=282.6674 nm - Linear plot.

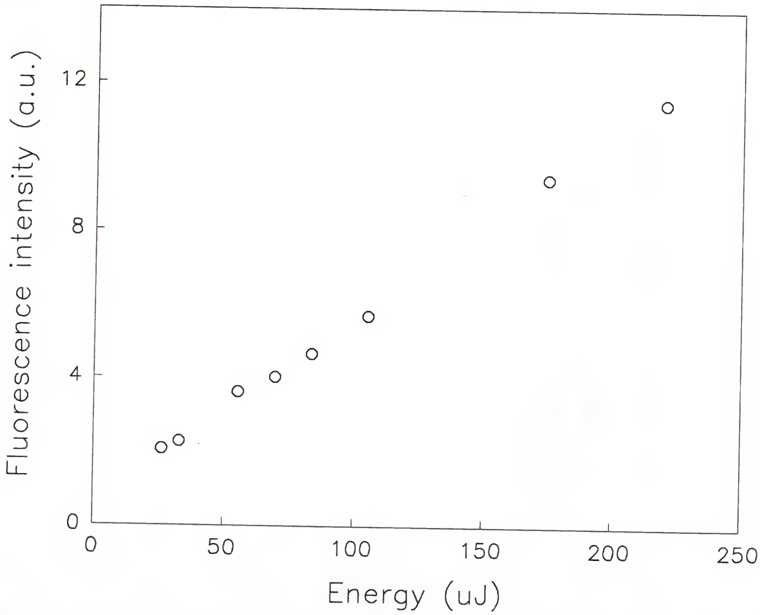
Fluorescence intensity (a.u.)
0
4
8
12
Energy (uJ)
0
50
100
150
200
250

Figure 35. Saturation curve for fluorescence signal at 303.9 nm while nebulizing water, λ_{exc}= $Q_1$5=282.6674 nm - Log-log plot.

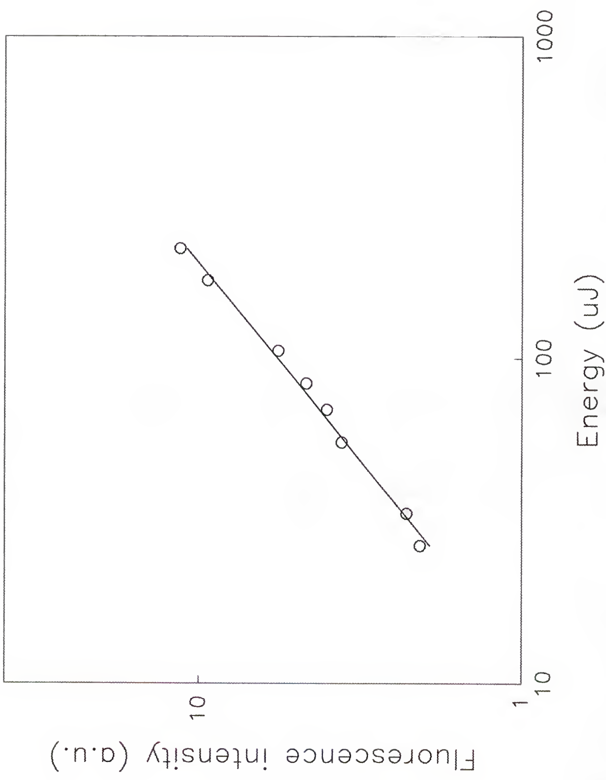
Fluorescence intensity (a.u.)
1
10
10
100
1000
Energy (uJ)

Figure 36. Emission spectrum of nebulized water, λ_{exc}= $Q_1 5$=282.6674 nm.

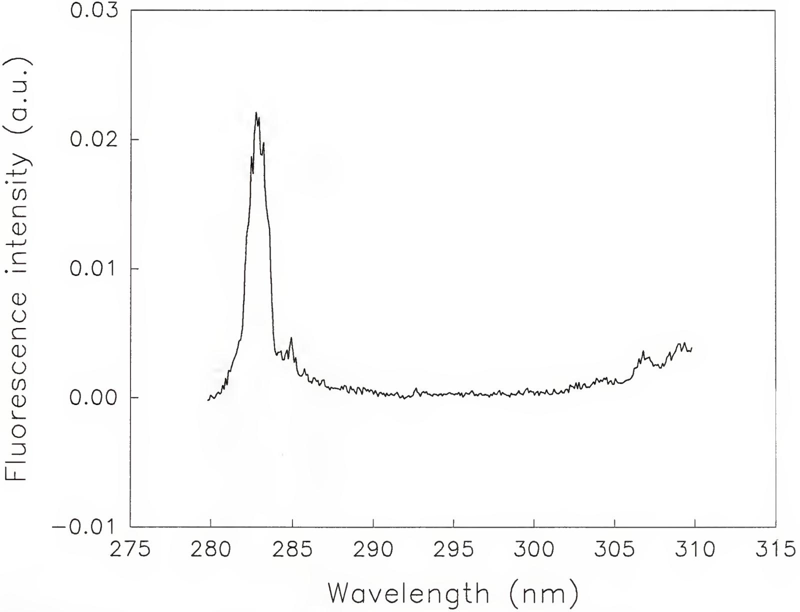
0.03
0.02
0.01
0.00
−0.01
275
280
285
290
295
300
305
310
315
Fluorescence intensity (a.u.)
Wavelength (nm)

at ≈ 303.9 nm is weak. For the proposed fluorescence mechanism, this could be considered an indication of the high efficiency of detection of the In-RID employed, since this weak fluorescence emission results in well resolved LEI peaks.

Assuming that OH fluorescence at 303.9 nm is the process responsible for the LEI signal, the procedure of evaluating the timing between λ_{exc} and λ_{23} at the flame using a photodiode is intrinsically inaccurate for this experiment. The timing coincidence that should be assured for this experiment is between the fluorescence photons (λ_{fl}) emitted at $Q_1 25$ (2→1 band) and the λ_{23}.

Since time coincidence between λ_{exc} and λ_{23} at the flame was already set from the previous experiments, an attempt was made to check the timing between the λ_{exc} and the production of fluorescence photons. The exciting laser pulse at 286.2035 nm ($P_1 9$ transition of the 1 → 0 band) and the fluorescence measured using the monochromator set at 303.9 nm (to detect the $Q_1 25$ line of the 2 → 1 band) were timed simultaneously using an oscilloscope. No time delay was observed between the onset of the laser pulse and the production of fluorescence photons; the time resolution available for the oscilloscope was ≈ 20 ns.

Unfortunately, this time resolution was not sufficient to observe the build up of fluorescence signal with respect to the laser pulse. The required time resolution can be inferred from the following studies. According to Lengel and Crosley

[45,46], the rate coefficient for a v′=2 to v′=1 energy transfer in $A^2\Sigma^+$ OH is 1.18 x 10^{-10} cm^3 s^{-1}. Using N_2 as a collision partner at P = 1 atm and T = 2200 K, the molecular nitrogen number density is 3.34 x 10^{18} cm^{-3} . Therefore, the rate for the process 2 → 1 is approximately 4 x 10^8 s^{-1}. At thermal equilibrium, the backward rate can be approximated by the following equation:

$$k_{1\rightarrow 2} \approx k_{2\rightarrow 1} \exp[-\Delta E/kT] \qquad (42)$$

where $k_{1\rightarrow 2}$ is the rate v′=1 to v′=2, $k_{2\rightarrow 1}$ is the rate v′=2 to v′=1, k is the Boltzmann constant (8.62 x 10^{-5} eV K^{-1}) and T is the temperature (K). ΔE is the difference in energy; for a transition between the rotational level K′=0 of the vibrational level v′=1 to the rotational level K′=0 of the vibrational level v′=2 in the $A^2\Sigma^+$ state of OH, ΔE ≈ 0.37 eV. Substituting these values into equation 42, an approximate rate can be obtained for the studied OH transition v′=1 to v′=2, $k_{1\rightarrow 2} \approx 5.7 \times 10^7$ s^{-1} or approximately 17.5 ns. Therefore, 17.5 ns is an approximation of the time necessary for build up of the fluorescence signal with respect to the laser pulse and a detector system with better time resolution is necessary for this experiment.

An energy diagram for indium is shown in Figure 37. It can be observed that several states, in addition to the state $^2D_{3/2}$ that is populated by λ_{12} = 303.9 nm, can be efficiently coupled with the RID second excitation step at λ_{23} = 786.4 nm.

Figure 37. Partial energy diagram for In:

- arrows indicate transitions wavelengths (nm);
- double arrows indicate energy difference between levels (eV).

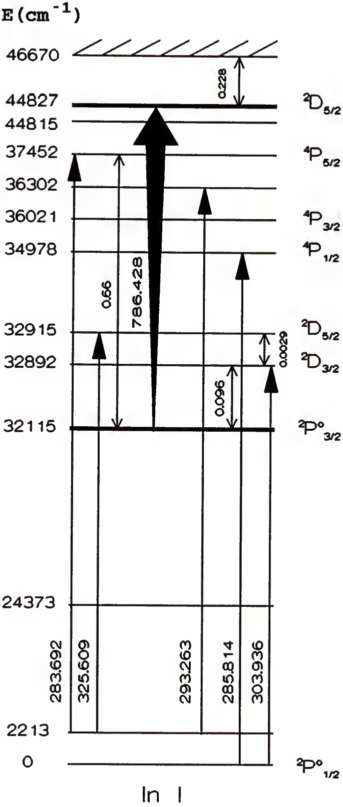
E(cm-1)
46670
44827
44815
37452
36302
36021
34978
32915
32892
32115
24373
2213
0
0.228
0.66
786.428
0.096
0.0029
283.692
325.609
293.263
285.814
303.936
²D5/2
⁴P5/2
⁴P3/2
⁴P1/2
²D5/2
²D3/2
²P°3/2
²P°1/2
In I

Table I shows the additional indium lines that could be efficiently coupled with λ_{23} in the flame and the OH transitions that could be detected by the In-RID. Only transitions in the 2 → 2, 2 → 1, 1 → 0 and 0 → 0 bands were considered. Transitions showing a wavelength difference between the OH and In lines ($\Delta\lambda$ OH/In) of less than 30 pm could still be detected due to the broadened indium absorption linewidth of ≈ 30 pm. All these possible events might contribute to the LEI signal obtained in the OH/In-RID.

Energy transfer mechanism

An energy transfer mechanism can also be proposed as a feasible mechanism to explain the OH peaks obtained while using the In-RID. Processes involving rotational [44,47] and vibrational [45] energy transfer in the $A^2\Sigma^+$ OH excited state and in the $X^2\Pi$ OH ground state [48] have been previously studied.

The proposed energy transfer mechanism can be explained by the use of the following equations:

$$\mathrm{OH}\ (v''=0,\ K''=\ldots) + h\nu_{exc} \rightarrow \mathrm{OH}\ (v'=1,\ K'=\ldots) \qquad (43)$$

$$\mathrm{OH}\ (v'=1, K'=\ldots) \rightarrow \mathrm{OH}\ (v'=0,\ K'=0) \qquad (44)$$

$$\mathrm{OH}(v'=0,\ K'=0) + \mathrm{In}(^2P^\circ_{1/2}) \rightarrow \mathrm{OH}(v''=0,\ K''=0) + \mathrm{In}(^2P^\circ_{3/2}) \qquad (45)$$

Figure 38 shows a schematic diagram of the proposed energy transfer mechanism. It should be noted that the energy difference (ΔE) for this process, i.e., between levels $v'=0$, $K'=0$ of the $A^2\Sigma^+$ state of OH and the $^2P^\circ_{3/2}$ state of In

Table 1: In transitions that could be coupled with λ_{23} and closest OH transitions.

Indium			OH			
λ (nm)	Transition (cm $^{-1}$) (ΔE(eV) from λ_{23})	f_{abs}	λ (nm)	Transition	Δλ OH/In (pm)	Relative Intensity
283.692	2213→37452 (0.66)	0.016	283.674	1→0 $R_2$16, $O_2$2	18.4	14+3
			283.709	1→0 3'	17.4	14
285.814	0→34978 (0.35)	0.28	285.797	1→0 $Q_1$13	16.6	60
293.263	2213→36302 (0.52)	0.08	293.256	2→1 $R_2$20	7	2
295.701	2213→36021 (0.48)	0.0011	295.673	1→0 $P_1$20	27.3	10+1
			295.731	2→1 $P_1$13	30.4	13+1
303.936	0→32892 (0.096)	0.495	303.937	2→1 $Q_1$25	1.3	1
325.609	2213→32916 (0.099)	0.5	325.601	2→2 $O_2$7	8	1+1
			325.592	2→2 $P_2$10	17.2	12+1
325.856	2213→32892 (0.096)	0.12	325.881	2→2 $P_1$11	25.4	13

Figure 38. Schematic diagram of the proposed energy transfer mechanism.

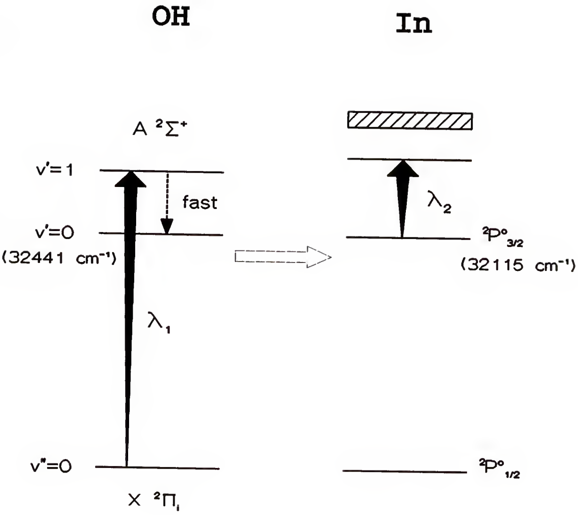
OH
In
A ²Σ⁺
v'=1
fast
v'=0
(32441 cm⁻¹)
λ₁
v"=0
X ²Πᵢ
λ₂
²P°₃/₂
(32115 cm⁻¹)
²P°₁/₂

(which is the initial state for the In-RID second excitation step at λ_{23}=786.4 nm), is only 326 cm^{-1} (0.04 eV).

Additional transfers of energy might also occur from other rotational and vibrational levels of the excited state of OH to one of the excited states of In, as is depicted in Figure 39. Many of these energy transfer processes exhibit a ΔE from the OH excited state in relation to the In $^2P^o_{3/2}$ state sufficiently small to be still optically connected to the second excitation step at λ_{23} = 786.4 nm.

Additional considerations

In order to examine the validity of the two proposed mechanisms additional experiments were performed. To evaluate whether fluorescence photons were indeed responsible for the LEI signal, the experiment shown in Figure 40 was executed. Water was nebulized into a 1 cm path lengthflame which was irradiated with the first excitation laser, λ_{exc}. The photons emitted by this arrangement were conveyed by an optical system into the small flame which had a high concentration of indium vapor and was irradiated simultaneously with the second excitation laser, λ_{23}. The LEI collection electrodes were connected to the small flame. It was expected that if the proposed fluorescence mechanism was responsible for the OH/In-RID signal, a LEI signal would be observed as a result of this experiment; however, no LEI signal could be detected. Nevertheless, this negative result is not seen as a conclusive proof against the fluorescence mechanism because the absence

Figure 39. Schematic diagram of additional possible processes of energy transfer.

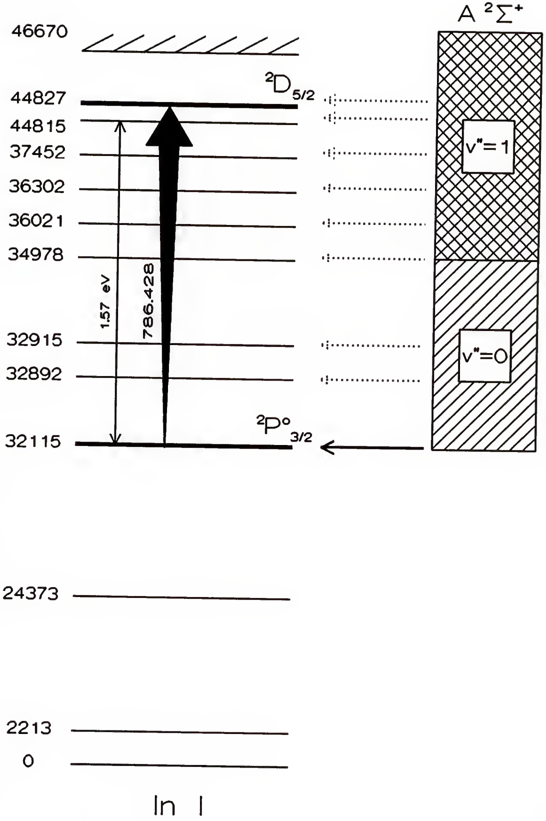
46670
44827
44815
37452
36302
36021
34978
32915
32892
32115
24373
2213
0
$^2D_{5/2}$
$^2P^o_{3/2}$
1.57 eV
786.428
$A\ ^2\Sigma^+$
v"=1
v"=0
In I

Figure 40. Schematic diagram of fluorescence collection experiment.

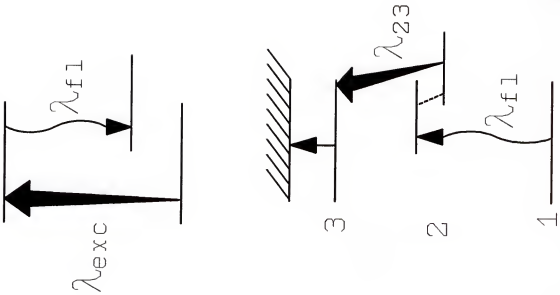
λexc
λfl
λ23
λfl
3
2
1

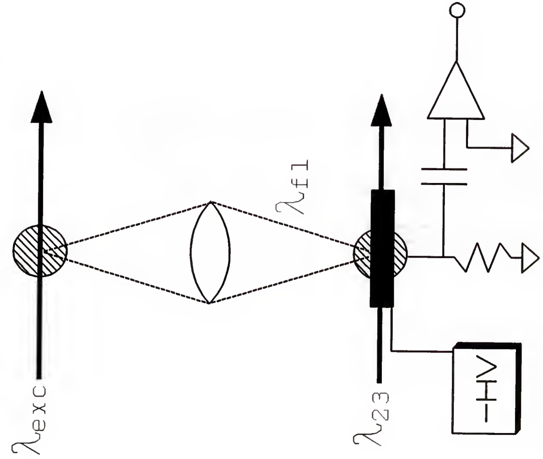
λexc
λfl
λ23
-HV

of LEI signal could be a consequence of the poor optical collection of the fluorescence photons generated in the 1 cm path length flame. Clearly, the optical collection efficiency in this experiment is much poorer than would be the case in the single flame measurements.

An attempt to excite OH in the 0 → 0 band by scanning λ_{exc} from 306.0 to 308.0 nm, while keeping λ_{23} fixed at 786.4 nm was also carried out. The experiment was performed both for water and indium solutions being nebulized into the flame. LEI and fluorescence signals were detected simultaneously by the use of two boxcar integrators. Fluorescence in the 0 → 0 OH band was observed for both the water and indium solutions ([In]=1%). No LEI signal was observed for water. The LEI spectrum of indium was mainly a broad band with some small features on top of it. Because of the high concentration of indium utilized, this broad band could be the wing of the In(I) 303.9 nm line, a transition with a high oscillator strength. As a consequence, it is not known if the LEI spectrum did not show resolved OH peaks due to a high background or if the fluorescence mechanism is the process responsible for the LEI signal. If an unequivocal In LEI signal was observed as a result of this experiment, the proposed mechanism involving the 303.9 nm line would be very unlikely because of the following reason. In this experiment, OH was excited in the 0 → 0 band; for the detection of the fluorescence photon emitted at the $Q_1 25$ transition from the 2

→ 1 band, a collisional redistribution from the $v'=0$ to $v'=2$ vibrational level of the excited $A^2\Sigma^+$ OH state would have to occur. This event is not probable, since the difference in energy between the two vibrational levels is ≈ 1.84 eV.

In another experiment, the emission of 0 → 0 band of OH was monitored while having the monochromator positioned at 306.4 nm. The λ_{exc} was set at 303.9 nm ($=\lambda_{12}$). The emission signal was sent to an oscilloscope. Initially a background emission signal was obtained by exciting nebulized water with λ_{exc}. If the energy transfer mechanism is the process responsible for the OH/In-RID signal, the nebulization of indium solution into the flame should increase the OH emission background signal. This would occur because the 303.9 nm photons absorbed by the ground state indium (In) could be transferred by the excited state indium (In*) to the ground state OH molecules (OH*). After collisional redistribution an increase in the emission of the 0 → 0 band would be detected. The inverse experiment, i.e., the transfer of energy from OH excited state to indium ground state could also be monitored in a similar experiment and it is shown schematically in the lower part of Figure 41. Equations 46 to 48 describe the events:

$$In + h\nu_{exc} \rightarrow In^* \qquad (46)$$

$$In^* + OH \rightleftarrows In + OH^* \qquad (47)$$

$$OH^* \rightarrow OH + h\nu_{0\rightarrow0} \quad . \qquad (48)$$

Figure 41. Schematic diagram of energy transfer experiment:
a) upper trace: energy transfer from In* to OH;
b) lower trace: energy transfer from OH* to In.

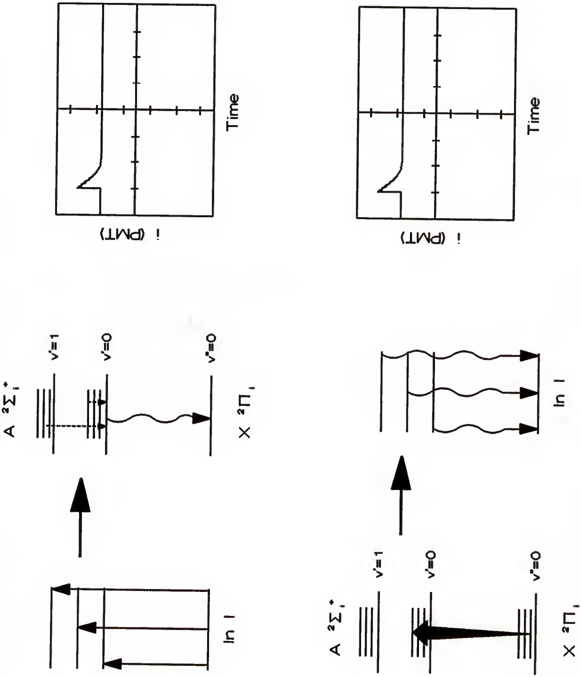
i (PMT)
Time
i (PMT)
Time
A $^2\Sigma_i^+$
v'=1
v'=0
v"=0
X $^2\Pi_i$
ln I
A $^2\Sigma_i^+$
v'=1
v'=0
v"=0
X $^2\Pi_i$
ln I

Figure 41 (upper part) shows a simplified schematic of the experiment and the output on the screen of the oscilloscope. It can be seen that an increase in the emission was observed, which was expected for the charge transfer mechanism. On the other hand, if the monochromator was scanned to wavelengths closer to the indium lines of 303.9 nm and 325.6 nm an increase in the intensity of the observed peak was observed. This means that part or all of the peak we observed when the monochromator was at ≈ 306.4 nm could be due to fluorescence of indium; therefore, energy transfer OH/In could or could not be associated with the experimental observations.

Unfortunately none of the above described experiments produced unequivocal proof of the actual mechanism involved in the detection of OH using the In-RID. Some experimental evidence favors the energy exchange process, such as the fact that a signal was not seen when the two flame experiment was performed and the fact that it takes ≈ 20 ns for the collisional build up of the population in OH vibrational level $v'=2$. On the other hand, tuning λ_{exc} in the region from ≈ 306 to 308 nm did not give a spectrum and boosting the indium population into the $^2D_{3/2}$ state (collisionally coupled with the $^2P^o_{3/2}$ state) produced no clear change in OH emission; these evidences could point to the fluorescence mechanism. At this point, the choice of one of the mechanisms as the most probable one is not possible and a feasible alternative is the participation of both mechanisms in the detection process.

CHAPTER 5
FLAME TEMPERATURE MEASUREMENTS USING THE OH/In-RID

Introduction

Combustion chemical kinetics and studies in turbulent reacting flow systems require the development of very sensitive techniques for evaluating the temperature with high spatial and temporal resolution [49]. Knowledge of the temperature may also be helpful in understanding the formation and disappearance of stable and unstable species in a flame. This can help in the formulation of comprehensive mathematical models for both basic combustion phenomena and practical devices, thus helping to find solutions for technical problems in combustion [50,51].

The OH molecule in both the ground and excited electronic states is produced by the oxidation of any hydrogen containing fuel. OH is also considered a key intermediate species in most combustion processes [45].

The temperature of OH in various flames has been used for many years as a rotational temperature indicator for flame combustion diagnostics [52]. Therefore, the decision to evaluate the applicability of the OH/In-RID to flame temperature measurements for combustion diagnostics came as a natural consequence of the experimental results described in the previous chapters.

Theory

The temperature of a flame is a reflection of its thermal energy [43]. This thermal energy is distributed between the activated particles to the various translational, rotational, vibrational, electronic and ionization states. Each one of these states can be defined separately by its own temperature; when this temperature is the same for all these states the flame is considered to be in thermal equilibrium.

The Boltzmann equation relates the population distribution of the excited states to the temperature of the exciting source; it can only be applied for thermal equilibrium conditions:

$$n_i/n_j = g_i/g_j \{\exp [-(E_i-E_j)/kT]\} \qquad (49)$$

where n_i and n_j are the number densities of particles (cm^{-3}), E_i and E_j are the energies (eV) with respect to the ground state, g_i and g_j are the statistical weights (dimensionless) of the ith and jth level, respectively, k is the Boltzmann constant (8.62×10^{-5} eV K^{-1}) and T is the absolute excitation temperature (K).

Thermodynamic equilibrium is achieved by collisions with other species, chemical reactions and the emission and reabsorption of radiation, when the system relaxes to an equilibrium state. Usually, the gas species do not spend sufficient time in the flame combustion zone to suffer a sufficient number of collisions to promote the distribution of the combustion energy among all of the various modes. Therefore, a single temperature cannot generally exist in a flame.

A local thermodynamic equilibrium (LTE) is characterized by a local temperature which describes the velocity particle distribution and the distributions of internal energy states at specific points in a flame. This means that thermal equilibrium is established at each point of the flame. In LTE, the temperatures (translational, vibrational, rotational, electronic and ionization) are statistically equivalent.

Measurements of flame temperatures in the outer cone of stoichiometric premixed flames using several procedures and states of excitation (vibrational, rotational and electronic) have shown that, within experimental errors, local thermodynamic equilibrium can be considered to exist in that region. On the other hand, thermal equilibrium is not reached in the inner cone; the temperatures obtained differ widely according to the measuring procedure.

The intensities of OH rotational bands can be used to determine the rotational temperature of a flame, assuming the existence of LTE. For rotationally resolved excitation fluorescence scans of OH in a flame [53,54] and for the LEI signal obtained in the OH/In-RID in the flame, the signal intensity normalized to the laser power (I, J^{-1} Hz cm^3) is given by:

$$I \propto B_{ij}\ n_{K",J"} \tag{50}$$

where B_{ij} is the Einstein coefficient of stimulated absorption (J^{-1} Hz cm^3) for a transition from level i to level j, $n_{K"J"}$ is the number density in the ground rotational state (cm^3), K" is the orbital angular momentum number with electronic spin disregarded and J" is the total angular momentum number, both in the ground state.

Assuming the existence of thermal equilibrium in the ground state, the Boltzmann relationship applies:

$$n_{K",J"} \propto (2J"+1)\ \exp\ [(-E_{K",J"}/kT)] \tag{51}$$

where $E_{K",J"}$ is the energy of the ground state rotational level (cm^{-1}), k is the Boltzmann constant (0.695 cm^{-1} K^{-1}) and T is the rotational temperature (K).

Combining equations (50) and (51) yields:

$$I \propto B_{ij}\ (2J"+1)\ \exp\ [(-E_{K",J"}/kT)] \tag{52}$$

By taking natural logarithms, the expression above can be written:

$$\ln\ [I/B_{ij}(2J"+1)] = C - E_{K",J"}/kT \tag{53}$$

where C is a constant. The left side of equation 53 is known, as I is measured and B_{ij} and J" are found in tables. The energy values are also known; therefore, a plot of ln $[I/B_{ij}(2J''+1)]$ vs $E_{K'',J''}$ is a straight line with the slope being equal to $-1/kT$. By measuring the slope, the rotational temperature can then be calculated.

The use of many transition lines for plotting the curve described by equation 53 can increase the accuracy of the determination of the temperature, since the influence of an occasional poor line can be minimized. It can also be affirmed that a rotational temperature exists if a straight line is obtained from the plot. A poor fitting may be due to several causes, among them the lack of thermal equilibrium in the source, the existence of a continuous background and the influence of self-absorption.

Experimental

The system described previously in Chapter 3 was used. All the conditions and parameters were the same, unless specified otherwise. The second excitation step was kept at λ_{23}=786.44 nm, while the first excitation step (λ_{exc}) was scanned through transitions of the 1 → 0 band of OH.

The dimensions of the flame used were the following: 30 mm in height (corresponding to 5 mm for the inner cone and 25 mm for the outer cone) and 6 mm in diameter in the central portion. The burner was mounted on a micrometer translational stage so that the flame could be moved in order to change the probing position of the first excitation laser in the flame.

Laser induced fluorescence (LIF) was employed to obtain flame temperature measurements for comparison purposes. While nebulizing water into the flame, transitions in the 1 → 0 band of OH were excited using the first excitation laser (λ_{exc}). The fluorescence excitation spectrum was recorded by collecting the fluorescence photons into a 0.22 m double monochromator (Model 1680B, Spex Industries, Edison, NJ) set at 306.4 nm.

Most of the OH excitation scans for flame temperature measurements were performed while having the two excitation laser beams (λ_{exc} and λ_{23}) crossing at 90° in the flame. Figure 42 shows a diagram with the modified experimental setup. The two laser beams were also focused into the flame. This configuration enabled the attainment of a greater spatial resolution for the temperature measurements. The diameters of the laser beams in the flame was measured by scanning a 25 μm slit mounted on a micrometer translational stage through each beam while monitoring the transmitted radiation with a photodiode. The beams were attenuated with neutral density filters to ensure a non-saturating regime for the photodiode. The beam diameter for the first excitation laser, λ_{exc}, was ≈ 100 μm. The second excitation laser, λ_{23}, had a beam diameter of ≈ 300 μm. These values were measured using 10% of the maximum signal as the cutoff limits for the diameter of the beam.

The profile of the temperatures in the flame at different regions of the flame was determined in the following way. The

Figure 42. Modified experimental configuration showing the two excitation laser beams crossing at 90° in the flame.

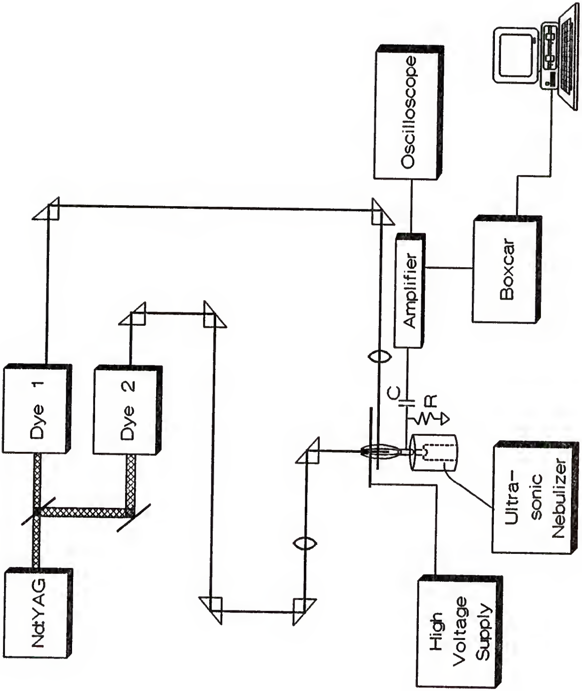
Nd:YAG
Dye 1
Dye 2
Oscilloscope
Amplifier
Boxcar
C
R
Ultra-
sonic
Nebulizer
High
Voltage
Supply

two excitation lasers were always kept crossed at a 90° angle at a fixed vertical distance from the burner head. The position of the second excitation beam in the flame was always kept unchanged. The flame was mounted on a micrometer translational stage; therefore, different horizontal positions of the first excitation laser in the flame could be obtained by changing the position of the flame.

The temporal coincidence of the two laser beams in the flame for this modified experimental configuration was checked according to the procedure described in Chapter 3. The FWHM for the first excitation laser was measured using the fundamental wavelength of the dye laser and it was found to be approximately 7 ns; the full width at the base of the laser pulse was ≈ 16 ns. The FWHM of the second excitation laser was 8 ns; the full width at the base of the laser pulse was ≈ 14 ns.

Results and Discussion

The first excitation region used for temperature measurements was from ≈ 286.0 to ≈ 287.8 nm. The transitions from the 1 → 0 band used were $Q_2 13$, $P_1 9$, $Q_1 14$, $P_2 9$, $Q_2 14$, $P_1 10$, $Q_1 15$, $P_2 10$, $Q_2 15$, $P_1 11$ and $Q_1 16$. Table 2 gives the wavelength (λ, nm) [40], the energy value of the lower state (E, cm^{-1}) [40], the total angular momentum number (J", dimensionless), the value of 2J"+1 (dimensionless) and the Einstein coefficient for stimulated absorption normalized to the

Table 2. Transitions of OH (1→0) used for calculation of temperature values in the flame.

Transition	λ(nm)	E(cm $^{-1}$)	J"	2J"+1	B_{ij} *
$R_1$10	281.5368	2014.98	10.5	22	201
$R_2$6	281.6024	824.49	5.5	12	190
$R_2$5	281.6549	608.15	4.5	10	183
$R_2$10	281.8677	2054.26	9.5	20	206
$Q_1$1	281.9145	0.03	1.5	4	240
$R_1$12	281.9822	2846.01	12.5	26	207
$R_2$2	282.1302	187.71	1.5	4	153
$P_1$1	282.1706	0.0	1.5	4	251
$Q_1$4	282.4393	355.87	4.5	10	361
$Q_1$5	282.6674	544.82	5.5	12	377
$Q_2$13	286.0615	3348.75	12.5	26	414
$P_1$9	286.2035	1650.74	9.5	20	211
$Q_1$14	286.3720	3819.01	14.5	30	418
$P_2$9	286.5668	1693.15	8.5	18	198
$Q_2$14	286.6237	3846.64	13.5	28	416
$P_1$10	286.8581	2014.98	10.5	22	210
$Q_1$15	286.9913	4251.19	15.5	32	418
$P_2$10	287.1987	2054.26	9.5	20	200
$Q_2$15	287.2324	4377.25	14.5	30	416
$P_1$11	287.5513	2413.51	11.5	24	209
$Q_1$16	287.6564	4915.04	16.5	34	418

* Values normalized to $P_1$1 of 0→0 band

coefficient value for the $P_1$1 transition of the 0 → 0 band (B_{ij} normalized, dimensionless) [55] for the above transitions and for other transitions that were also used for temperature measurements. Figure 43 shows a typical spectrum obtained for the region ≈ 286.0 - 286.3 nm. The flame region analysed was the center of the flame, 4 mm above the inner cone. The drift and the poor signal-to-noise observed in the spectrum were characteristic of this region which corresponded to the end of the lasing range of the dye used (rhodamine 590).

For each temperature measurement an excitation spectrum was acquired. The signal intensities used for the calculation of the temperature were measured using two approaches, peak heights measured directly from the spectrum and peak heights measured after a Gaussian function was fitted to each peak. The temperature values were obtained by plotting the data using Equation 53; the plot is shown in Figure 44. After fitting the curves with a least squares program both temperatures were very similar, 2516 ± 175 K for the first approach and 2493 ± 195 K for the Gaussian approach. Attempts to reduce the standard deviation by normalizing the peak heights for variations in laser power output detected by photodiodes, both for λ_{exc} and λ_{23}, were not sucessful. The estimated volume of the probed region is ≈ 2 x 10^{-6} cm^3.

Instead of obtaining an excitation spectrum for each flame temperature measurement, the peak heights were also determined by a "sitting" procedure, where a slow scan of the

Figure 43. Typical excitation spectrum of OH rotational transitions used for flame temperature measurements in the OH/In-RID.

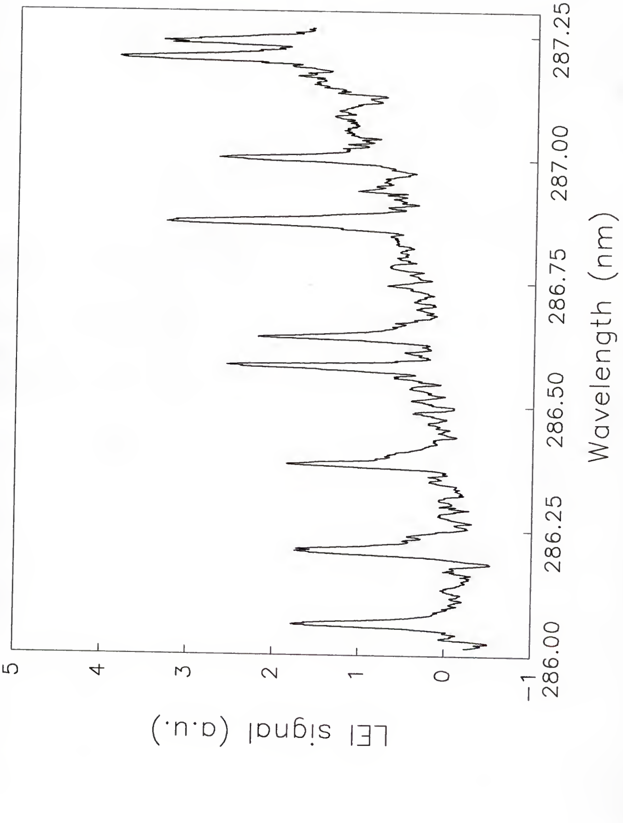
LEI signal (a.u.)
5
4
3
2
1
0
−1
286.00
286.25
286.50
286.75
287.00
287.25
Wavelength (nm)

Figure 44. Boltzmann plots used for calculation of temperature; transitions used were from the 1 → 0 band of OH in the region 286.0 - 287.8 nm:

a) solid line, circle symbols: linear regression line using peak heights
b) dashed line, square symbols: linear regression line using Gaussian fitting.

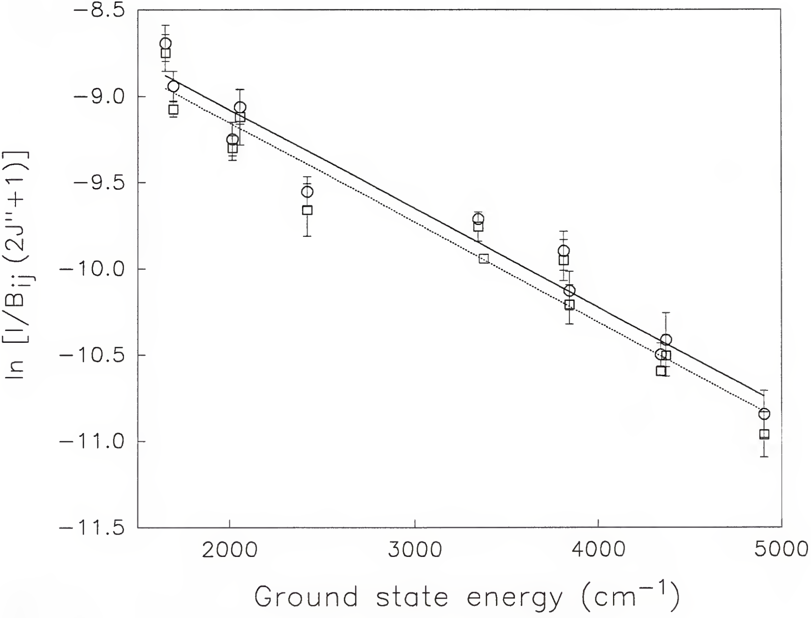

-8.5
-9.0
-9.5
-10.0
-10.5
-11.0
-11.5
$\ln\,[I/B_{ij}\,(2J''+1)]$
2000
3000
4000
5000
Ground state energy (cm^{-1})

first excitation laser to the peak of each transition was made. The peak heights were then measured while sitting on the transition peak. Both procedures were almost equally time consuming. The acquisition of one spectrum took about 5 min and usually 5 spectra were taken for each flame temperature measurement when the scanning procedure was used. A complete acquisition of the data for one set of transitions using the "sitting" procedure also took around 40 - 45 min.

Figure 45 shows a plot of data acquired while using the "sitting" procedure. The temperature value obtained with this method was 2641 ± 301 K. The larger standard deviation obtained for this procedure was probably associated with the difficulty of stopping the scan of the first excitation laser at the actual peak of the transition.

In order to evaluate if the large standard deviations obtained for the temperature values were a characteristic of the OH/In-RID as a method or were due to the poor signal to noise ratio of the region scanned, another set of transitions in a region that had a better signal to noise ratio was analysed. The transitions from 1 → 0 band of OH used were $R_1 10$, $R_2 6$, $R_2 5$, $R_2 10$, $R_1 12$, $R_2 2$, $P_1 1$, $Q_1 4$ and $Q_1 5$. Figure 46 shows a representative excitation spectrum of the transitions used; the typical signal to noise ratio was ≈ 100. The wavelengths and the constants used for the calculation of the temperature are given in Table 2.

Figure 45. Boltzmann plots obtained for the "sitting" procedure; transitions used were from the 1 → 0 band of OH in the region 286.0 - 287.8 nm.

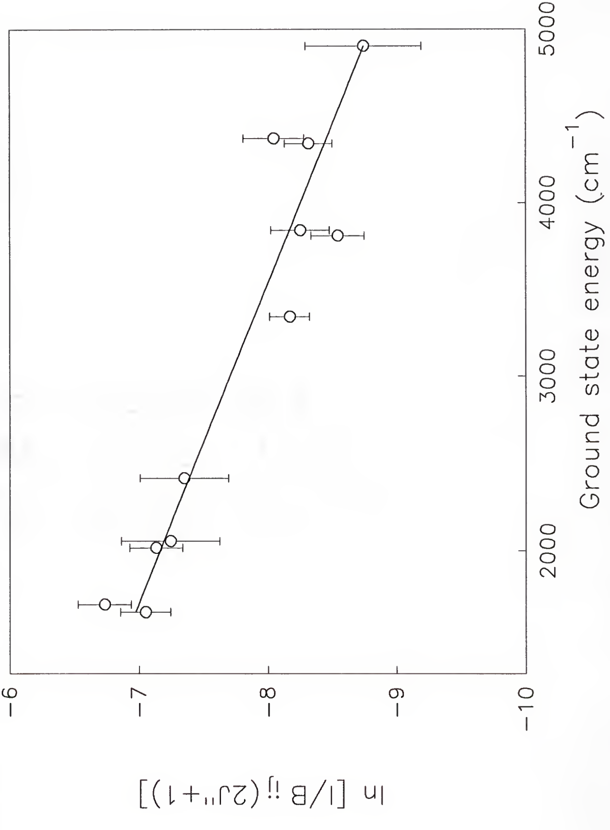
-6
-7
-8
-9
-10
ln [I/B ij (2J''+1)]
2000
3000
4000
5000
Ground state energy (cm^{-1})

Figure 46. Typical excitation spectrum of OH rotational transitions used for flame temperature measurements in the OH/In-RID.

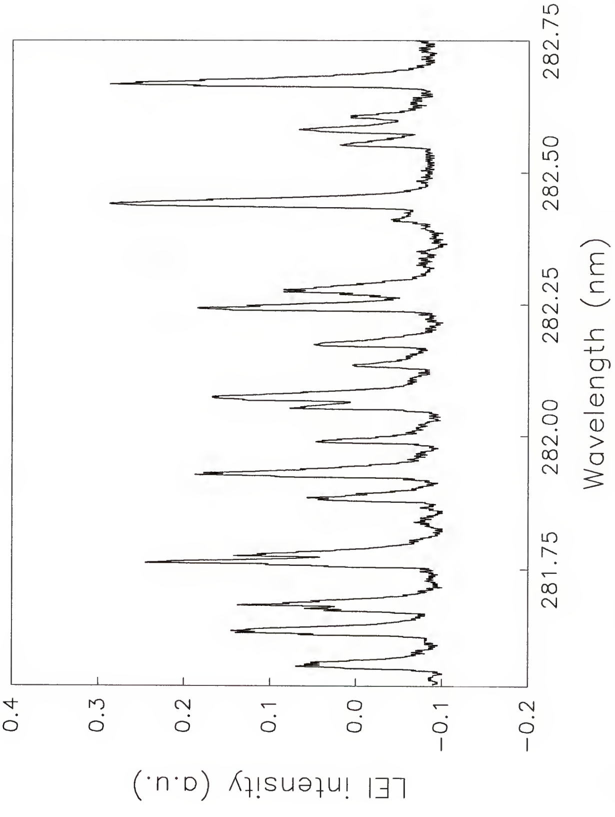
LEI intensity (a.u.)
0.4
0.3
0.2
0.1
0.0
−0.1
−0.2
281.75
282.00
282.25
282.50
282.75
Wavelength (nm)

A profile of the temperatures in the flame was performed by using the procedure of scanning the first excitation laser. The lasers were positioned at ≈ 7 mm above the burner head, which corresponded to ≈ 2 mm above the inner cone. Five spectra were acquired for each calculated flame temperatures. Figure 47 shows a representative plot with the linear regression line for each one of the 5 scans; the graph shows the data for the position placed at 3.4 mm from the center of the flame. This position was the furthest position from the center that generated a spectrum with a reasonable signal to noise ratio so that peak heights could be measured.

Table 3 summarizes the temperature values obtained for the different positions in the flame that were analysed. The flame temperature profile is shown in Figure 48. The relative standard deviations were generally in the range 4% - 11%. It was observed that the signal to noise ratio for each flame position was dependent on the concentration of the nebulized indium solution; higher indium concentrations (≈ 2%) for the flame edge and lower indium concentrations (≈ 0.5 %) for the center of the flame produced the best results. The temperature value for the position at the center of the flame obtained for this second scanned region was 2722 ± 325 K and was comparable to the temperature obtained for the first scanned region, 2516 ± 175 K; however, the standard deviation was larger. On the other hand, it should be noted that the larger temperature

Figure 47. Representative Boltzmann plot used for calculation of temperature; results of OH/In-RID 5 different scans from the 1 → 0 band of OH in the region ≈ 281.3 - 282.8 are shown.

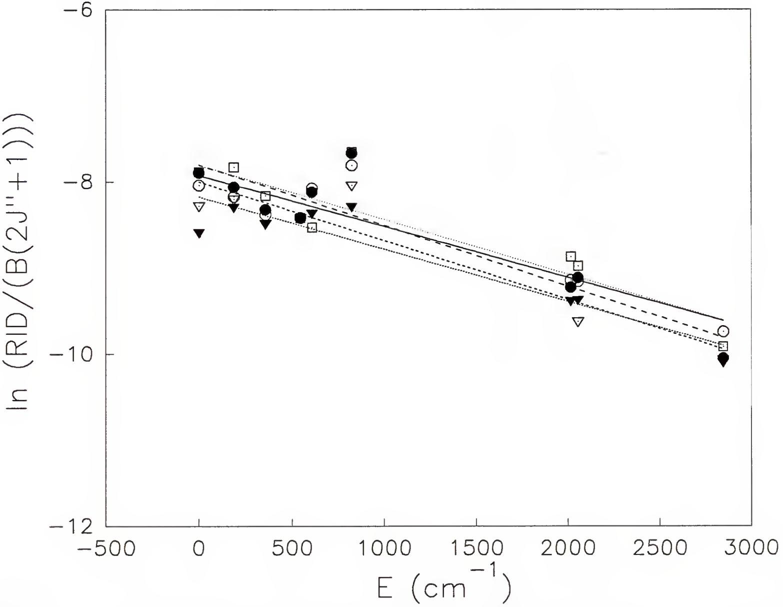
−6
−8
−10
−12
ln (RID/(B(2J''+1)))
−500
0
500
1000
1500
2000
2500
3000
E (cm^{-1})

Table 3. Temperatures obtained for the OH/In-RID technique.*

Distance from center (mm)	Temperature (K)
0	2722±325
0.2	2423±112
0.4	2532±182
0.6	2719±228
0.8	2451±149
1.1	2744±149
1.5	2571±333
1.9	2596±252
2.3	2518±242
2.7	2417±130
3.1	2067±126
3.4	2234±169

* The procedure of scanning the excitation laser was used

Figure 48. Flame temperature profile at ≈ 2 mm above the inner cone using the procedure of scanning the excitation laser in the OH/In-RID technique ; symmetry was assumed.

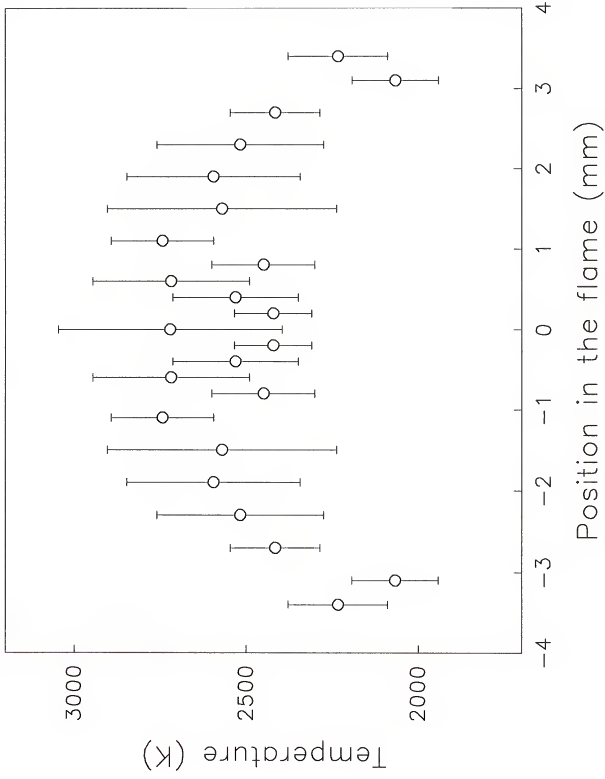
Temperature (K)
3000
2500
2000
Position in the flame (mm)
−4
−3
−2
−1
0
1
2
3
4

value was obtained for a distance of 2 mm above the inner cone of the flame, while the smaller value refered to a distance of 4 mm above the inner cone of the flame. The flame temperature did not exhibit much variation in the region between the center and 2.5 cm away from the center; towards the edge of the flame a significant decrease in the temperature could be observed. Generally the relative standard deviation values for the temperatures obtained for the two different excitation regions scanned were quite similar and seemed to be characteristic of the OH/In-RID method for our system.

A profile of the temperatures in the flame was performed also by using the procedure of "sitting" on the peak of each transition. Table 4 gives the temperature values obtained, while Figure 49 shows the profile exhibited by the flame using this procedure. Comparing the two profiles, it can be observed that the flame temperature values obtained for the procedure of "sitting" on the peak of each transition are significantly lower than the values obtained for the procedure of scanning the excitation laser; this was probably a result of the difficulty of stopping the scan of the excitation laser on the peak of the transition. The relative standard deviations are also higher for the "sitting" procedure; generally between 13% and 15%.

Two possibilities of alternative techniques for comparison of the temperature values obtained with the OH/In-RID were examined but could not be used. The line reversal

Table 4. Temperatures obtained for the OH/In-RID technique.*

Distance from center (mm)	Temperature (K)
0	1914±257
0.2	1912±264
0.4	1816±279
0.6	1767±246
1.1	1890±268
1.6	1902±285
2.1	1817±273

* The procedure of "sitting" on the peak of each transition was used

Figure 49. Flame temperature profile at ≈ 2 mm above the inner cone using the procedure of "sitting" on the peak of each transition in the OH/In-RID technique; symmetry was assumed.

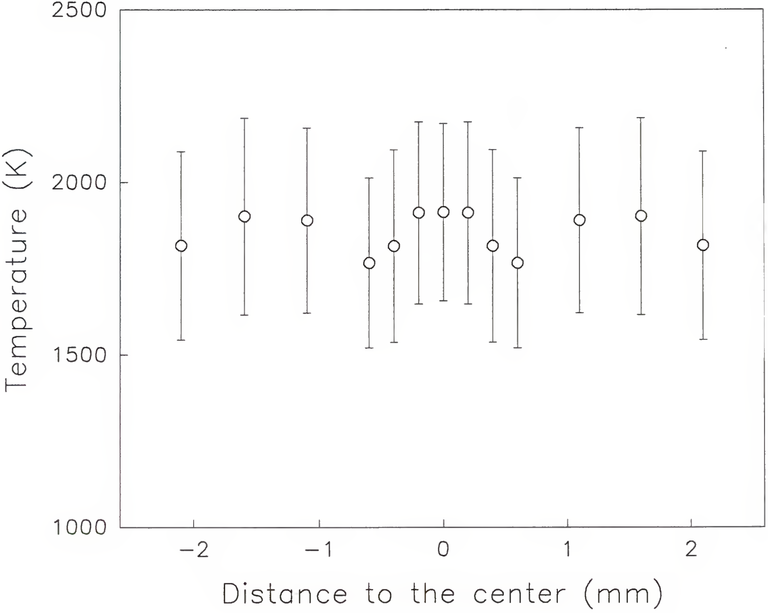

2500
2000
1500
1000
Temperature (K)
−2
−1
0
1
2
Distance to the center (mm)

method [43,52] could not be employed since a calibrated blackbody radiator was not available in our laboratory at the time of this work. The technique of determination of the electronic temperature of the flame through detection of iron emission [52,56,57] in the region 369.0 - 378 nm was experimentally tried. Unfortunately, the spectral resolution achieved in our system was not sufficient to resolve the iron emission peaks while using the monochromator in the first order. Second order was also tried, but the peak intensities were too low and the S/N ratio was poor. The "two-line" method of flame temperature measurement for iron emission [58] was investigated, but the resolution and/or the intensities of the peaks were not sufficient for any of the line-pairs to be used.

Laser induced fluorescence (LIF) was employed as a comparison technique for the temperatures in the flame. The transitions of the OH 1 → 0 band that were excited were in the region ≈ 281.5 nm - 287.8 nm and they correspond to the same transitions used for the second scanned region employed for the OH/In-RID experiments: $R_1 10$, $R_2 6$, $R_2 5$, $R_2 10$, $R_1 12$, $R_2 2$, $P_1 1$, $Q_1 4$ and $Q_1 5$. Figure 50 shows a typical fluorescence excitation spectrum obtained in our experiments. The flame volume probed was ≈ 50×10^{-6} cm^3. This volume was 25 times greater than the volume probed by the OH/In-RID, because of the excellent spatial resolution of the OH/In-RID technique.

Figure 50. Excitation spectrum of OH obtained by the use of the LIF technique.

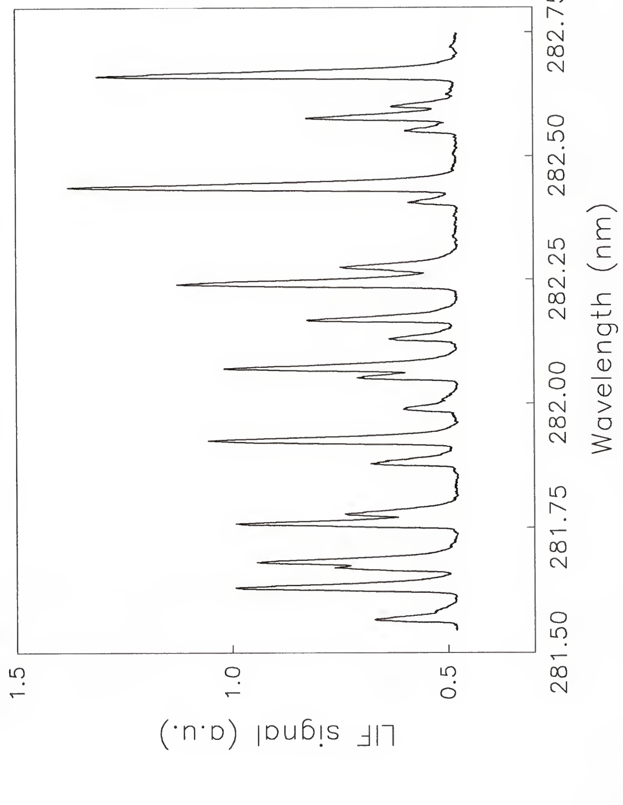
LIF signal (a.u.)
1.5
1.0
0.5
281.50
281.75
282.00
282.25
282.50
282.75
Wavelength (nm)

Figure 51 shows a representative plot with the linear regression line for each one of the 5 scans that were usually recorded for calculation of each temperature. In this experiment, the center of the flame was imaged into the monochromator and the laser path was positioned at about 2 mm above the inner cone. The temperature obtained was 1897 ± 87 K. Even though an attempt was made to image only the central region of the flame into the monochromator, the lower temperature values were probably observed because the LIF temperature corresponded to a line-of-sight measurement. Therefore, this temperature is an average of the flame temperature at ≈ 2 mm above the inner cone, which was the region excited by the laser beam, while the OH/In-RID temperature values were spatially resolved and representative of the flame area probed by the intersection of the two beams. The standard deviation is of the same order of magnitude as the smaller values obtained by the OH/In-RID technique.

The LIF technique used here did not have the high spatial resolution of the OH/In-RID. A profile of the flame temperatures was attempted by imaging into the monochromator different parts of the flame. The excitation laser beam and the monochromator entrance slits were parallel to each other. The imaging of different regions of the flame was achieved by moving the flame across the monochromator slit. The flame temperature profile obtained is shown in Figure 52. The temperature results are summarized in Table 5. The

Figure 51. Representative Boltzmann plot used for calculation of temperatures; results of LIF 5 different scans from the OH 1 → 0 band in the region ≈ 281.5 - 282.8 nm are shown.

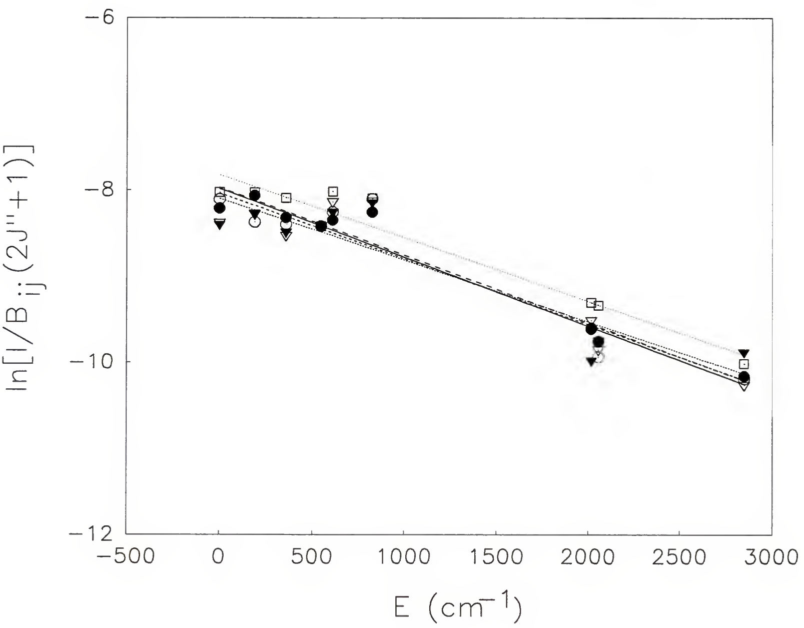

−6
−8
−10
−12
−500
0
500
1000
1500
2000
2500
3000
$\ln[I/B_{ij}(2J''+1)]$
E (cm^{-1})

Figure 52. Flame temperature profile at ≈ 2 mm above the inner cone using the procedure of scanning the excitation laser in the LIF technique; symmetry was assumed.

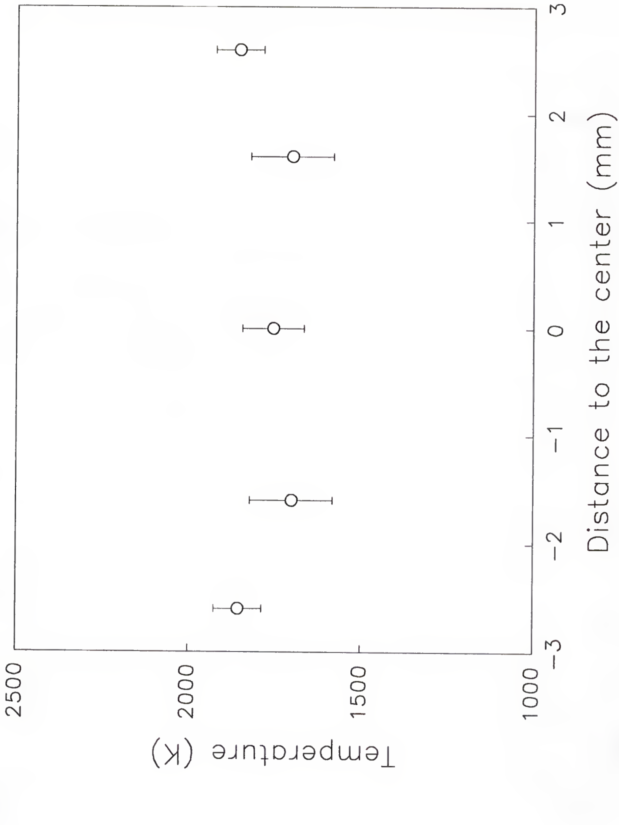
Temperature (K)
2500
2000
1500
1000
−3
−2
−1
0
1
2
3
Distance to the center (mm)

Table 5. Temperatures obtained for the LIF technique.*

Distance from center (mm)	Temperature (K)
0	1755±89
1.6	1702±120
2.6	1855±69

* The procedure of scanning the excitation laser was used

temperature values obtained were very similar for the whole region probed and a difference in flame temperature at different regions could not be detected. The relative standard deviations were of the same order of magnitude as the smaller values obtained by the OH/In-RID technique.

The precision of the OH/In-RID method using our experimental setup was not comparable with the values commonly reported for measurement of flame temperatures, which can exhibit precision values as low as 5 K for the line-reversal method and are between 50 - 200 K for spectral emission methods [52]. Experimental conditions such as poor precision in the energy output of the second excitation laser, on the order of 30 -40%, and problems in the delivery of solution to the flame due to the nebulizer performance could have contributed to the errors in the temperature measurements.

This problem could also be associated with the fact that the excitation laser pulses used were of the order of 8 ns, while pulses of the order of μs are generally used for flame temperature measurements. The achievement of steady-state conditions in the rotational levels can be questioned when flame radicals such as OH are subjected to such short pulse excitation [59] since the laser pulse is probably not long enough to allow all the rotational level populations to equilibrate. In the case of the fluorescence mechanism for the OH/In-RID, each rotational level might also exhibit different temporal collisional behavior in populating the fluorescing level ($Q_1$25) in the v′=2 manifold. Steady state is established throughout the upper and lower sets of rotational levels only after a succession of collisional transfers occurs, which for OH has been estimated to require more than 30 ns in an atmospheric flame.

The use of fluorescence data obtained by laser excitation pulse lengths of the order of nanoseconds can be simplified by the use of the balanced cross-rate model. The basic principle of this model is that the single directly excited upper rotational level is coupled very strongly to the single directly excited lower rotational level via fast absorption and stimulated emission processes. As a consequence, at saturation intensities, a steady-state population balance is established between these two levels in much less than a nanosecond. The achievement of steady-state throughout the rest of the rotational levels is established much more slowly by collisional transfer processes [48,59]. The application of the balanced cross-rate model to the prevailing conditions in our system is somewhat difficult because saturation conditions were not reached for the first excitation step (λ_{exc}). Furthermore, the mechanism responsible for the OH/In-RID has not yet been determined with certainty and further studies are needed to validate the use of this model for the OH/In-RID results obtained in this work.

CHAPTER 6
CONCLUSIONS AND FUTURE WORK

The resonance ionization detection technique using indium as the detector element was evaluated in an air-acetylene flame. Both one step excitation at λ_{12}=303.9 nm and step-wise excitation using λ_{12}=303.9 nm and λ_{23}=786.4 nm were studied. Collisions in the flame were responsible for the ionization step. Saturation curves were performed for both excitation schemes. The conditions of a photon detector are best simulated for low energy values in the first excitation step and saturation of the second excitation step. For our experimental configuration, these energy values corresponded to less than 7 nJ for the first transition and more than 80 μJ for the second transition. The quantum efficiency of the detector was estimated to be ≈ 2.2 %; this low value could be associated with the poor output energy performance of the dye laser that delivered the second excitation step.

An LEI rotational spectrum of OH 1 → 0 band was recorded in the In-RID while scanning the first excitation laser (λ_{exc}) in the region ≈ 281.0 nm to 288.0 nm and having the second excitation laser (λ_{23}) at 786.4 nm. The LEI signal showed a linear dependence on the energy of λ_{exc} up to the maximum energy attainable at the flame (≈ 300 μJ) and no optical saturation could be observed. The second excitation step could be saturated with ≈ 2.5 mJ of energy. Studies pointed to the following values for optimized conditions: voltage applied to the collection electrode between -1300 and -1600 V; concentration of In ≈ 2%; incident power applied to the ultrasonic nebulizer of ≈ 30 W and flow rates of 108 $cm^3 min^{-1}$ for acetylene and 800 $cm^3 min^{-1}$ for air.

Two mechanisms were proposed to explain the observed rotational OH spectrum recorded in the RID, the fluorescence capture mechanism and the energy transfer mechanism. Several experiments were performed to evaluate the possibility of one or both mechanisms being involved in the OH/In-RID. Some experimental evidence favored the energy transfer process while others favored the fluorescence mechanism. Definite proof of the actual mechanism involved in the detection of OH using the In-RID was not accomplished and both mechanisms could be contributing to the phenomenon.

The application of the OH/In-RID to the determination of flame temperatures was evaluated. Flame temperatures were profiled using the procedure of obtaining an excitation spectrum for each flame temperature measurement and the procedure of doing a slow scan of the first excitation laser to the peak of each transition and measuring the peak while sitting on the transition peak. The former produced smaller standard deviations and higher temperature values than the latter, probably due to the difficulty of stopping the scan of the excitation laser right on the peak of the transition in the "sitting" procedure. The temperature values obtained for ≈ 2 mm above the inner cone with the "scanning" procedure were ≈ 2500 - 2700 K for the region between 0 and 2.3 mm away from the center; the temperature values were lower towards the edge of the flame, reaching ≈ 2200 K at 3.4 mm away from the center of the flame. Relative standard deviations were of the order of 4 - 11 %.

The results of the flame temperature measurements using the OH/In-RID were compared with results obtained with LIF. The temperature values for the LIF technique were lower than those obtained with the OH/In-RID; values around ≈ 1700 - 1860 were obtained for the region at ≈ 2 mm above the inner cone and between 0 and 2.6 mm away from the flame that was probed. These lower values probably resulted from the line-of-sight observations in the LIF measurements, while the OH/In-RID values were spatially resolved. The relative standard deviations for the LIF technique were of the same order of magnitude of the smaller values obtained by the OH/In-RID, i.e., 4%.

The poor precision of the OH/In-RID in our experimental conditions could be associated with the use of short pulse excitation lasers of the order of 8 ns; for these short pulse lengths, the achievement of steady state conditions in the rotational states can be questioned.

Application of the OH/In-RID to combustion diagnostics can be proposed as a direct extension of this work. The spatial mapping of OH number density distributions in flames of different types and compositions and the determination of other fundamental constants related to the quenching and collisional processes in flames could contribute to the understanding of the overall combustion process.

Longer dye laser pulses, on the order of μs, should be investigated as excitation sources for the OH/In-RID. Those lasers could provide energy to the system for a period of time sufficient for achievement of a steady-state regime through successive collisional transfers. If this steady-state condition was not achieved with our nanosecond excitation laser, better precision and accuracy could probably be achieved by this approach.

Other experiments are necessary in order to investigate the proposed mechanisms for the OH/In-RID. One such experiment is the time resolved measurement of the build up of the fluorescence signal at 303.9 nm from OH transition $Q_1 25$ ($2 \rightarrow 1$ band) with respect to the excitation laser pulse λ_{exc}. This signal should be compared with the fluorescence build up from OH at 306.4 nm ($0 \rightarrow 0$ bandhead). It is expected that the former would show a slower build up, since the transfer from the excited $v'=1$ level to the $v'=2$ would have to rely on upward collisional transfer processes. In this case, a delaying of the second excitation laser (λ_{23}) in relation to the first excitation laser (λ_{exc}) would result in an increase of the LEI signal, since the temporal overlapping of the fluorescence photons and λ_{23} would be optimized if the fluorescence capture mechanism is valid.

Detection of OH using resonance ionization with other detection elements can be attempted. The use of bismuth as a detector element for OH in a flame seems feasible. For the Bi-RID, the following excitation scheme could be used: λ_{12}=306.772 nm and λ_{23}=382.0. The OH transition $R_2$9 (0 → 0 band), λ_{trans}=306.7775 nm, has an intensity ≈ 400 times greater than the $Q_1$25 (2 → 1 band) that has been hypothesized as being the first excitation step for the present OH/In-RID in the fluorescence capture mechanism. Assuming that the fluorescence photons emitted by OH at 306.7775 nm would be collected by the detector as the first excitation step for the bismuth atoms, the OH/Bi-RID would theoretically exhibit signals ≈ 400 times more intense than the OH/In-RID. Furthermore, the technique would rely on downward vibrational energy transfer from the v′=1 to the v′=0 instead of the upward vibrational transfer from v′=1 to v′=2 in OH/In-RID.

The energy coincidence of rotational and vibrational transitions of other flame species, such as NO and CO, with transitions from the ground states for other atomic elements should be examined in order to evaluate the possibility of detection of these flame species by resonance ionization detection.

REFERENCE LIST

1. A. C. Eckbreth, P. A. Bonczyk and J. F. Verdieck, "Review of Laser Raman and Fluorescence Techniques for Pratical Combustion Diagnostics", U.S.E.P.A., Washington, DC (1977).

2. J. D. Ingle, Jr. and S. R. Crouch, "Spectrochemical Analysis", Prentice-Hall, Inc., New Jersey (1988).

3. V. S. Letokhov, "Laser Photoionization Spectroscopy", Academic Press, Inc., London (1987).

4. J. C. Travis, G. C. Turk and R. B. Green, *Anal. Chem.* **54**, 1006A, (1982).

5. J. C. Travis, G. C. Turk, J. R. DeVoe, P. K. Shenck and C. A. van Dijk, *Prog. Analyt. Atom. Spectrosc.* **7**, 199 (1984).

6. N. Omenetto, B. W. Smith and L. P. Hart, *Fresenius Z. Anal. Chem.* **324**, 683 (1986).

7. O. Axner and H. Rubinsztein-Dunlop, *Spectrochim. Acta* **44B**, 835 (1989).

8. N. Omenetto and J. D. Winefordner, *Prog. Analyt. Atom. Spectrosc.* **2**, 1 (1979).

9. G. A. Petrucci, Ph. D. Dissertation, University of Florida (1990).

10. J. C. Travis, G. C. Turk and J. R. DeVoe, *Clin. Chem.* **29**, 1683 (1983).

11. J. C. Travis, G. C. Turk and R. B. Green, "New Applications of Lasers to Chemistry", American Chemical Society Symposium Series No. 85, A.C.S. (1978).

12. G. C. Turk, J. C. Travis and J. R. DeVoe, *Journal de Physique* **44**, C7-301 (1983).

13. J. C. Travis, *J. Chem. Educ.* **59**, 909 (1982).

14. G. C. Turk, *J. Analytic. Atom. Spect.* **2**, 573 (1987).

15. R. W. Wood, *Phil. Mag.* **10**, 513 (1905).

16. R. W. Wood, *Phil. Mag.* **23**, 689 (1912).

17. J. V. Sullivan and A. Walsh, *Appl. Opt.* **7**, 1271 (1968).

18. J. V. Sullivan and A. Walsh, *Spectrochim. Acta* **21**, 727 (1965).

19. J. V. Sullivan and A. Walsh, *Spectrochim. Acta* **22**, 1843 (1966).

20. M. A. Nippoldt and R. B. Green, *Appl. Opt.* **20**, 3206 (1981).

21. E. F. Zalewski, R. A. Keller and C. T. Apel, *Appl. Opt.* **20**, 1584 (1981).

22. N. Omenetto, B. W. Smith and P. B. Farnsworth, in *Proceedings of RIS-90, Inst. Phys. Conf. Ser. No. 114: Section 9*, eds. J. E. Parks and N. Omeneatto, IOP Publishing Ltd., Bristol, p.369 (1991).

23. J. B. Dawson, E. Grassam and D. J. Ellis, *Analyst* **101**, 587 (1976).

24. H. G. C. Human, J. A. Strauss and L. R. P. Butler, *Spectrochim. Acta* **35B**, 207 (1980).

25. R. Stephens, *Can. J. Chem.* **58**, 1621 (1980).

26. G. A. Petrucci and J. D. Winefordner, *Spectrochim. Acta* **47B**, 437 (1992).

27. E. F. Palermo and S. R. Crouch, *Anal. Chem.* **45**, 1594 (1973).

28. O. I. Matveev, N. B. Zorov and Y. Y. Kuzyakov, *J. Anal. Chem. U.S.S.R.* **34**, 654 (1979).

29. O. I. Matveev, *J. Anal. Chem. U.S.S.R.* **38**, 561 (1983).

30. N. Omenetto, B. W. Smith and J. D. Winefordner, *Spectrochim. Acta, Part B*, Special Supplement on the Proceedings of the Symposium held at Pontifical Academy of Sciences, 91 (1989).

31. O. I. Matveev and V. A. Pribytkov, *J. Appl. Spectrosc. U.S.S.R.* **46**, 16 (1987).

32. O. I. Matveev, *J. Anal. Chem. U.S.S.R.* **38**, 561 (1983).

33. S. H. Bloom, E. Korevaar, M. Rivers and C. S. Liu, *Opt. Lett.* **15**, 294 (1990).

34. T. Okada, H. Andou, Y. Moriyama and M. Maeda, *Opt. Lett.* **14**, 987 (1989).

35. B. W. Smith, N. Omenetto and J. D. Winefordner, *Spectrochim. Acta, Part B*, Special Supplement on the Proceedings of the Symposium held at Pontifical Academy of Sciences, 101 (1989).

36. B. W. Smith, P. B. Farnsworth, J. D. Winefordner and N. Omenetto, *Opt. Lett.* **15**, 823 (1990).

37. G. A. Petrucci, R. G. Badini and J. D. Winefordner, *J. Anal. At. Spectrom.* **7**, 481 (1992).

38. N. Omenetto, B. W. Smith, P. B. Farnsworth and J. D. Winefordner, *J. Anal. At. Spectrom.* **7**, 89 (1992).

39. R. G. Badini, G. A. Petrucci and J. D. Winefordner, *J. Quant. Spectrosc. Radiat. Transfer* **50**, 47 (1993).

40. G. H. Dieke and H. M. Crosswhite, *J. Quant. Spectrosc. Radiat. Transfer* **2**, 97 (1962).

41. E. L. Baardsen and R. W. Terhune, *Appl. Phys. Lett.* **21**, 209 (1972).

42. D. K. Killinger and C. C. Wang, *J. Chem. Phys.* **71**, 1582 (1979).

43. R. Mavrodineanu and H. Boiteux, "Flame Spectroscopy", John Wiley and Sons, Inc., New York (1965).

44. M. L. Parsons, B. W. Smith and G. E. Bentley, "Handbook of Flame Spectroscopy", Plenum Press, New York (1975).

45. R. K. Lengel and D. R. Crosley, *J. Chem. Phys.* **67**, 2085 (1977).

46. R. K. Lengel and D. R. Crosley, *J. Chem. Phys.* **68**, 5309 (1978).

47. G. Zizak, J. A. Lanauze and J. D. Winefordner, *Combust. Flame* **65**, 203 (1986).

48. G. Zizak, G. A. Petrucci, C. L. Stevenson and J. D. Winefodner, *Appl. Opt.* **30**, 5270 (1991).

49. G. Zizak, N. Omenetto and J. D. Winefordner, *Opt. Eng.* **23**, 749 (1984).

50. K. C. Lück and W. Thielen, *J. Quant. Spectrosc. Radiat. Transfer* **20**, 71 (1978).

51. J. H. Bechtel, *Appl. Opt.* **18**, 2100 (1979).

52. M. L. Elder and J. D. Winefordner, *Prog. Analyt. Atom. Spectrosc.* **6**, 293 (1983).

53. W. R. Anderson, L. J. Decker and A. J. Kotlar, "Temperature Profile of a Stoichiometric CH_4/N_2O Flame from Laser Excited Fluorescence Measurements On OH", Technical Report ARBRL-TR-02412, U. S. Army Ballistic Research Laboratory, Aberdeen (1982).

54. W. R. Anderson, L. J. Decker and A. J. Kotlar, "NH and OH Concentration Profiles in a Stoichiometric CH_4/N_2O Flame by Laser Excited Fluorescence and Absorption Techniques", Technical Report ARBRL-TR-02426, U. S. Army Ballistic Research Laboratory, Aberdeen (1982).

55. I. L. Chidsey and D. R. Crosley, *J. Quant. Spectrosc. Radiat. Transfer* **23**, 187 (1980).

56. W. R. L. Masamba, Ph. D. Dissertation, University of Florida (1992).

57. B. M. Spencer, II, Ph. D. Dissertation, University of Florida (1993).

58. G. F. Kirkbright, M. Sargent and S. Vetter, *Spectrochim. Acta* **25B**, 465 (1970).

59. R. P. Lucht, D. W. Sweeney and N. M. Laurendeau, *Appl. Opt.* **19**, 3295 (1980).

BIOGRAPHICAL SKETCH

Denise Imbroisi was born on September 25, 1961, in São João del-Rei (Minas Gerais), Brazil. She received her bachelor's degree in chemistry from Universidade de Brasília, Brasília (Distrito Federal), Brazil, in 1982. A master's degree from the same University was completed in 1986 in the area of electrochemistry.

She has taught at the University of Brasília as a Teaching Assistant while in her master's program and as a Assistant Professor after completion of her degree. In August 1987 she joined the Environmental Department of Centrais Elétricas do Norte do Brasil S. A. (Eletronorte).

In 1989 she was awarded a scholarship from the Brazilian agency Conselho Nacional de Desenvolvimento Científico e Tecnológico (CNPq) for pursuing doctorate studies. She took an educational leave of absence from Eletronorte in May 1990 and joined the Ph.D. program of University of Florida, Gainesville, Florida, in the summer of 1990.

I certify that I have read this study and that in my opinion it conforms to acceptable standards of scholarly presentation and is fully adequate, in scope and quality, as a dissertation for the degree of Doctor of Philosophy.

James D Winefordner

James D. Winefordner, Chair
Graduate Research Professor of Chemistry

I certify that I have read this study and that in my opinion it conforms to acceptable standards of scholarly presentation and is fully adequate, in scope and quality, as a dissertation for the degree of Doctor of Philosophy.

Gerhard M Schmid

Gerhard M. Schmid
Associate Professor Emeritus of Chemistry

I certify that I have read this study and that in my opinion it conforms to acceptable standards of scholarly presentation and is fully adequate, in scope and quality, as a dissertation for the degree of Doctor of Philosophy.

Anna Brajter-Toth
Associate Professor of Chemistry

I certify that I have read this study and that in my opinion it conforms to acceptable standards of scholarly presentation and is fully adequate, in scope and quality, as a dissertation for the degree of Doctor of Philosophy.

John R. Eyler

John R. Eyler
Professor of Chemistry

I certify that I have read this study and that in my opinion it conforms to acceptable standards of scholarly presentation and is fully adequate, in scope and quality, as a dissertation for the degree of Doctor of Philosophy.

Eric R. Allen
Professor of Environmental Engineering Sciences

This dissertation was submitted to the Graduate Faculty of the Department of Chemistry in the College of Liberal Arts and Sciences and to the Graduate School and was accepted as partial fulfillment of the requirements for the degree of Doctor of Philosophy.

April 1994

Dean, Graduate School